Multiparametric MRI of Neurodegeneration in the Peripheral Nervous System

By

Michael David Pridmore

Dissertation

Submitted to the Faculty of the

Graduate School of Vanderbilt University

in partial fulfillment of the requirements

for the degree of

DOCTOR OF PHILOSOPHY

in

Chemical and Physical Biology

June 30th, 2020

Nashville, Tennessee

Approved:

Bruce M. Damon, Ph.D.

John C. Gore, Ph.D.

Seth A. Smith, Ph.D.

Wesley P. Thayer, M.D., Ph.D.

Richard D. Dortch, Ph.D.

This body of work is dedicated to my friends, family, and the others who have challenged me:

I would not be the person I am today without you.

ACKNOWLEDGEMENTS

First, I would like to express my great appreciation to Dr. Richard Dortch for showing unfailing support, encouragement, and a great sense of humor over my time as his graduate student. He has given me a great opportunity to develop into a critically-thinking scientist, and showed me that I am more capable than I thought. I would also like to thank Dr. Seth Smith for his friendship and being a constant supporting mentor, leading me to apply to the Chemical and Physical Biology program back in 2015. I thank my other committee members, Drs. John Gore, Wesley Thayer, and the chair, Bruce Damon, who have greatly impacted my scholarship and inspired me to excel past my own expectations. I would like to express huge gratitude to the MRI technologists at the Vanderbilt University Institute of Imaging Science, as well as Marcia Spear, Ellie Dahms, and Alesia Pruitt, and Teresa Turner for outreach, recruitment, and coordination of research participants. I would also like to thank Dr. Filip Szczepankiewicz, Dr. Junzhong Xu, Dr. Mark Does, Dr. Jun Li, Dr. Bennett Landman, Dr. Isaac V. Manzanera Esteve, and Alonda Pollins for each of their contributions toward my academic development. Thank you to Dr. Beth Bowman for advising me on applying directly to the Chemical and Physical Biology program. I would be remiss not to mention the fellow students and staff that went through the trenches with me. Steve Damon, Ben Conrad, Dr. Sam By, Dr. Kurt Schilling, Dr. Alex Smith, Dr. Andrew Plaasard, Dylan Lawless, and Willy Reickert have all had a substantial impact on my academic performance, for better or worse, and I cannot thank you enough for being at my side. Lastly, I would like to thank Bruce Damon and Patty Mueller for organizing such a diverse and inclusive graduate program. She and Bruce have crafted a great graduate program that shows real devotion and care to students.

TABLE OF CONTENTS

Page

Chapter

LIST OF TABLES

LIST OF FIGURES

LIST OF ABBREVIATIONS

CMAP	Compound Muscle Action Potential
CMT	Charcot-Marie-Tooth disease
CMTNS	Charcot-Marie-Tooth Neuropathy Score
CNS	Central Nervous System
CTS	Carpal Tunnel Syndrome
DML	Distal Motor Latency
DTI	Diffusion Tensor Imaging
EMG	Electromyography
F_{per}	Fat Percentage
HNPP	Hereditary Neuropathy with liabilities to Pressure Palsies
LTE	Linear Tensor Encoding
MCV	Motor Conduction Velocity
MHQ	Michigan Hand Outcomes Questionnaire
MRI	Magnetic Resonance Imaging
MTR	Magnetization Transfer Ratio
NCS	Nerve Conduction Studies
NHPT	Nine-Hole Peg Test
PEG	Polyethylene Glycol
PMP22	Peripheral-Myelin-Protein 22
PNS	Peripheral Nervous System
ROI	Region of Interest
SE	Spin Echo
SNAP	Sensory Nerve Action Potential
SPL	Sensory Peak Latency
STE	Spherical Tensor Encoding
T	Tesla
TE	Echo Time
TR	Repetition Time
TPNI	Traumatic Peripheral Nerve Injury

CHAPTER I

INTRODUCTION

1.1 Purpose

The overall goal of this dissertation is to develop and evaluate magnetic resonance imaging (MRI) methods to characterize peripheral nerve microstructure and pathologies in vivo in humans. More specifically, we assessed the ability of quantitative MRI methods developed for the central nervous system (CNS) to assay myelin and axonal pathologies in peripheral nerves in patients with inherited neuropathies and nerve trauma. Furthermore, we translated a recently developed advanced diffusion MRI method to the peripheral nervous system for the first time to overcome the lack of specificity inherent in traditional diffusion MRI approaches.

Of the two pathologies studied, both have limitations in standard clinical care that may be augmented by noninvasive measures of nerve pathology that can be assessed with MRI methods. Despite this promise, many of quantitative MRI methods have not been translated to the peripheral nervous system (PNS) because of the technical challenges associated with imaging small nerves. In this work, we developed strategies to overcome these challenges, evaluated these new methods in two patient cohorts, and translated an emerging diffusion method that may improve our ability to differentiate myelin and axon pathologies. If successful, the methods herein could be used to improve clinical care by providing information about the degree of pathology, which can inform clinicians and surgeons of proper treatment strategies (e.g., the need to re-operate) and response to therapy.

1.2 Dissertation Overview

1.2.1 Background

Chapter 2 serves as an overview of the general anatomy, organization of the peripheral nervous system, Chapter 3 will cover MRI principles, and Chapter 4 details how these concepts are combined to peripheral neuropathies. In addition, a brief review of the biology of nerve trauma and inherited neuropathies will be discussed in Chapter 2. Overall, these reviews will include applied imaging methods and current clinical tools for assessment of nerve pathology. Finally, the detailed summary of current MRI methods will shed light on the areas that are relevant to nerve pathology and set the stage for where advanced tools may help improve our ability to gain specific measures of nerve pathology. This foundational knowledge will illustrate why there is a current need for non-invasive imaging to assess nerve health across multiple clinical presentations.

1.2.2 Inherited Neuropathy in the Lower Extremity

In Chapter 5, we will explore a rare neurodegenerative disease, known as Hereditary Neuropathy with liability to Pressure Palsies (HNPP), which is a primary dysmyelinating neuropathy with secondary axonal loss. Individuals with HNPP experience a gradual progression of symptoms over time, such as numbness, tingling, and recurring weakness under mechanical pressure. Many of these symptoms are length-dependent, with distal areas of the limb having symptoms before moving proximally towards the spinal cord. Current clinical assessments and their limitations will be discussed. These will be compared to the quantitative MRI protocols developed herein, such as nerve magnetization transfer ratio (MTR) imaging and muscle Dixon fat-water imaging, which were performed in the distal and proximal leg to measure the length-dependent nature of the disease. The results of this study demonstrated that quantitative MRI measures of nerve and muscle pathology are feasible and may serve as a non-invasive biomarker in patents with HNPP. These results have been published in *Annals of Clinical and Translational Neurology,* (Pridmore, et al. (2020). doi:10.1002/acn3.50953).

1.2.3 Trauma in the Upper Extremity

Chapter 6 will focus on individuals with upper extremity trauma, including full laceration and surgical repair of the median and/or ulnar nerve(s) and compression of the median nerve, as seen in Carpal Tunnel Syndrome (CTS). In this study, we imaged all subjects post-operatively with Diffusion Tensor Imaging (DTI) to evaluate regeneration after surgical intervention. Data from traumatic peripheral nerve injuries (TPNIs) were compared to carpal tunnel subjects and healthy controls to assess the sensitivity of DTI indices to injury severity. In addition, a subset of TPNI patients were scanned longitudinally and DTI findings were compared to clinical outcomes. Together, these findings demonstrate that DTI indices may be predictive of outcomes and show promise as a non-invasive method to identify failed surgeries that may require secondary procedures to restore function.

1.2.4 Multidimensional Diffusion of the Sciatic Nerve

DTI has improved our ability to diagnose and monitor certain diseases. However, the method may lack specificity to the complex underlying microstructural changes that occur in trauma and disease. For instance, partial voluming effects may occur between crossing fibers and/or regions with edema, losing valuable information on microstructure within that area and misleading interpretations of nerve de/regeneration. Multidimensional diffusion, or tensor-valued diffusion encoding, is a promising new diffusion MRI method that offers improved specificity to tissue microstructure over traditional DTI methods. This method has been previously validated in the brain. In Chapter 5, the challenges of translating this method to the sciatic nerve will be detailed. In addition, the scan-rescan repeatability of the method will be evaluated and compared to DTI methods in the sciatic nerve of healthy subjects. Future applications where this technique may provide information on microstructure that DTI cannot capture will be discussed.

1.2.5 Conclusions

The final chapter will present limitations that were present in each study, challenges of applying basic and advanced MRI techniques to the peripheral nervous system, and future directions of the work presented herein. Specifically, small sample size, patient comfort, and subject motivation are discussed, as well as strategies for post-processing of novel MRI data, the need for high resolution to image small structure, and ways to extend the findings presented in this dissertation to future studies that seek to probe specific aspects of nerve microstructure.

Funding support

This research is supported by grants from National Institutes of Health/NINDS, R01 NS066927 (J.L.) and R01 NS097821 (R.D.), the Muscular Dystrophy Association, the National Center for Advancing Translational Sciences (UL1TR000445), and the Department of Defense, MR150075 (WT). All studies herein were approved by our local Institutional Review Board and all

participants provided informed consent prior to all examinations. Deidentified data related to each study will be made available upon reasonable request.

CHAPTER II

THE PERIPHERAL NERVOUS SYSTEM

2.1 Peripheral Nervous System and Pathology

2.1.1 General Nerve Anatomy

The human peripheral nervous system (PNS) is composed of bundles of axons that connect organs, limbs, and sensory receptors to the central nervous system (CNS), containing the brain and spinal cord. The PNS facilitates the communication of the brain and spinal cord to organs and muscles, while also allowing for sensory feedback to the CNS. Control of these commands is divided into two systems: the autonomic nervous system and somatic nervous system[1]. The autonomic nervous system is responsible for governing involuntary body functions, such as heart rate, salivation, and pupil constriction/dilation[2]. For the purpose of this dissertation, we will focus on the somatic nervous system specifically, which governs voluntary control of muscles and feedback of sensory information to the CNS. The nerves of the peripheral nervous system originate from a network of branches that extend from multiple sections of the spinal cord. For the purpose of this dissertation, we will focus on the nerves of the upper (Chapter 6) and lower extremities (Chapter 5 and 7), which originate from the brachial and sacral plexus, respectively.

The brachial plexus arises from spinal nerves C5, C6, C7, C8, and T1, and further divisions result in lateral, medial, and posterior cords that give rise to the musculotaneous, axillary, median, ulnar, and radial nerves in the upper extremity, which extend to the distal ends of the arm[1]. The median nerve innervates the flexor muscles of the forearm (except the flexor carpi ulnaris and the medial part of the flexor digitorum profundus), the intrinsic muscles of the hand for control of palmar and distal-dorsal areas of the thumb, index finger, middle finger, and lateral half of the ring finger, and also provides sensory supply to these areas. The ulnar nerve innervates two muscles in the forearm, the flexor carpi ulnaris and the medial part of flexor digitorum profundus, and the intrinsic muscles of the hand for control of the ring finger and pinky finger. Sensory supply of the ulnar nerve is given to the palmar and dorsal surfaces on the medial half of the ring finger and the entire pinky finger. While the radial nerve contributes to motor and sensory innervation to part of the forearm and the dorsal part of the hand, the median and ulnar nerves will be the specific focus of Chapter 6 when we look at cases of traumatic peripheral nerve injury and compression. Figure 2-1 shows the organization of these nerves in the wrist and hand.

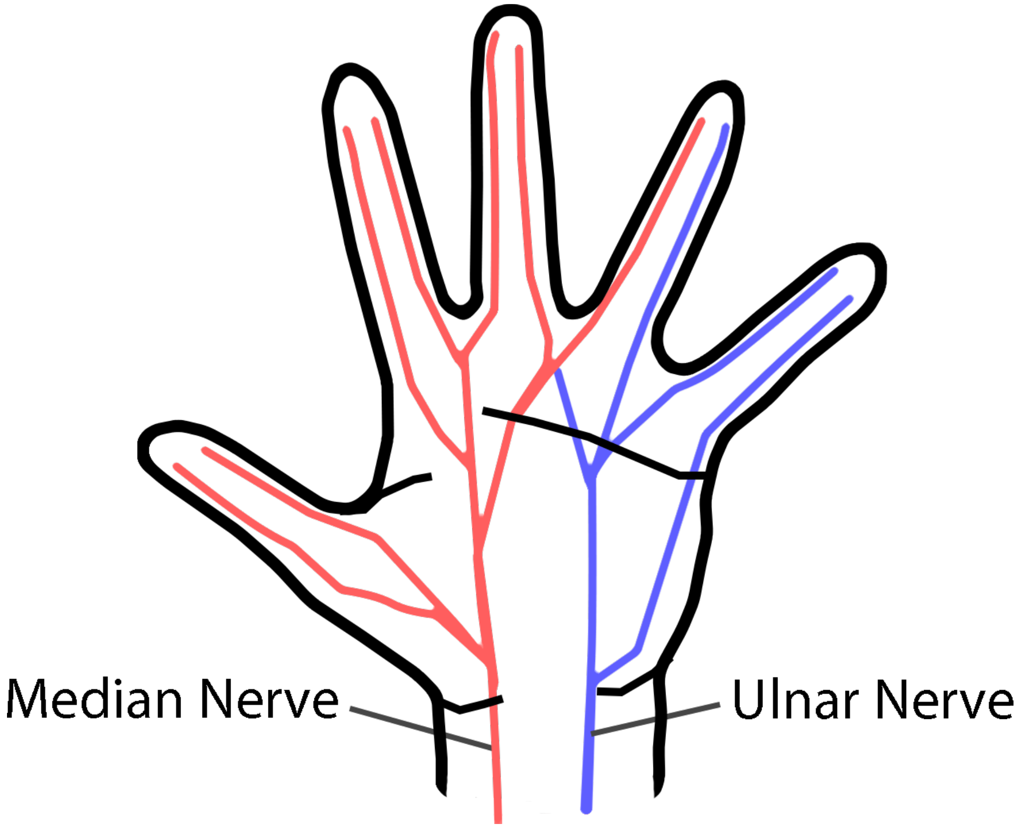

Figure 2-1: Peripheral nerves of the hand. Median Nerve labeled in red. Ulnar nerve labeled in blue. View is facing palmar regions of the hand.

The sacral plexus in the lower extremity, which originates from spinal nerves L4, L5, S1, S2, S3, and S4, results in formation of the sciatic, tibial, and common peroneal nerves which extend from the hip to the distal areas of the leg[1]. The sciatic nerve innervates the muscles of the thigh, specifically the biceps femoris, semimembranosus, and semitendinosus muscles, providing extension of the hip and flexion of the knee. There are no direct sensory functions of the sciatic nerve, however it has indirect innervations through terminal branches in all parts of the lower extremity. Moving distally, past the knee, the sciatic nerve bifurcates into the tibial and common peroneal nerves. Further distal, the common peroneal nerve splits again into deep and superficial peroneal nerves (not shown in Figure 2-2). The tibial nerve innervates the muscles of the leg distal to the knee, specifically the gastrocnemius, soleus, popliteus, flexor digitorum longus, flexor hallicus longus, and tibialis posterior muscles. Tibial nerve innervation of these muscles provide plantar flexion of the ankle as well as adduction, abduction, and flexion of toes[1]. Sensory contributions of the tibial nerve arise from the lateral sides of distal leg sole (plantar surface) of the foot. An illustration of these structures is shown in Figure 2-2. While the common peroneal nerve contributes to motor function of foot and sensory function via the sural nerve branch, the sciatic and tibial nerves of the leg will be the specific focus of (i.) Chapter 5 where we assess an inherited neuropathy disease and (ii.) Chapter 7 where we will evaluate an advanced diffusion method that offers improved specificity over traditional DTI methods.

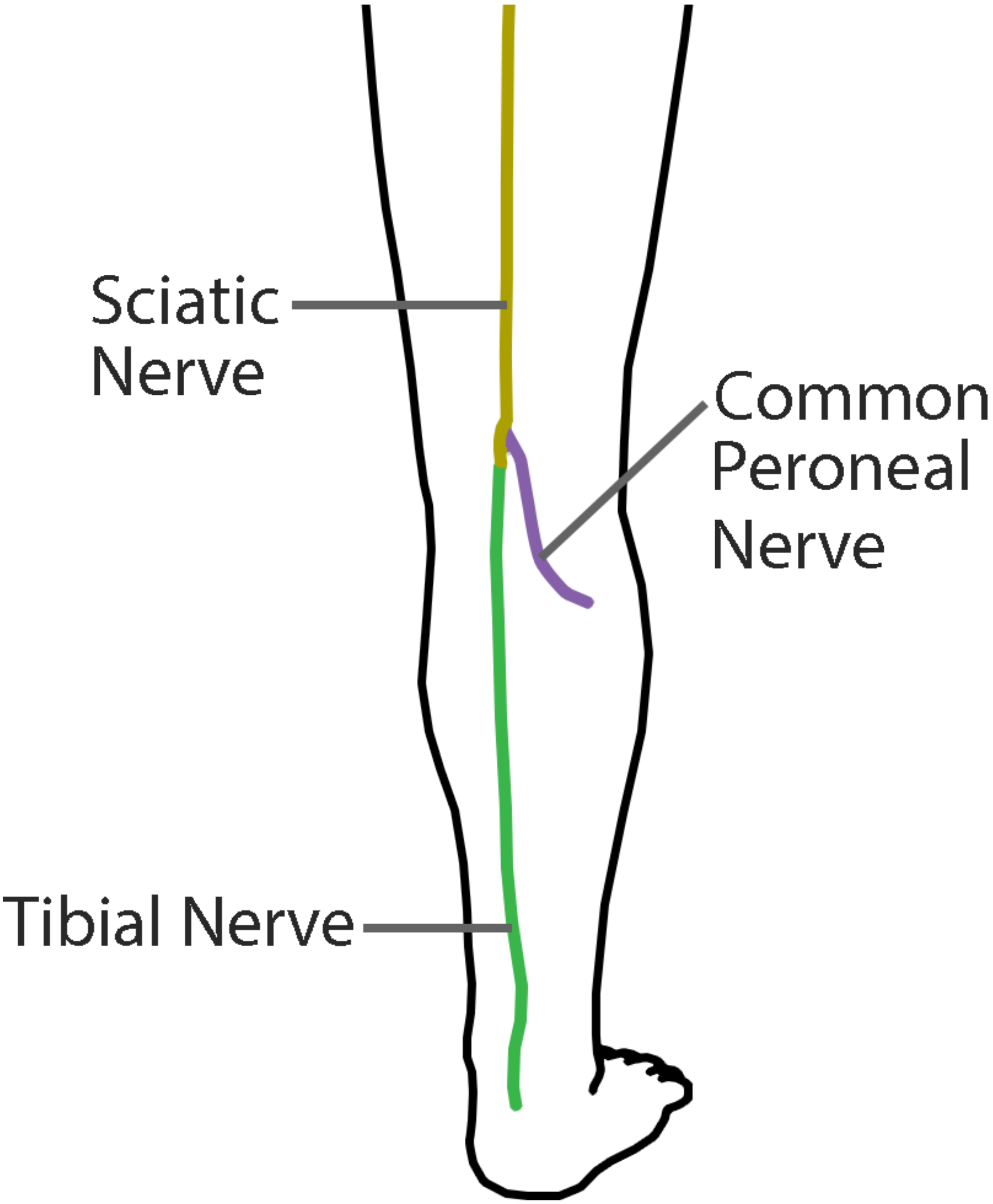

Figure 2-2: Peripheral nerves of the leg. Sciatic nerve labeled in yellow. Common peroneal nerve labeled in purple. Tibial nerve labeled in green. View is from backside of the leg, with the foot facing away from view.

Now that we have established where brachial and sacral plexuses originate and how these systems are connected to the central nervous system, a review of peripheral nerve microstructure will allow for an understanding of the biological mechanisms that give rise to sensory and motor function in the body. Figure 2-3 illustrates the basic structure of a peripheral nerve. The main components of peripheral nerves include axons, which conduct sensory and motor axon potentials; Schwann cells, which myelinate axons and promote the conduction of action potentials; and connective tissue, which provides mechanical integrity. Each of these three main features will be detailed in the following section to illustrate how the PNS functions and the biological contributions that allow for these functions to occur.

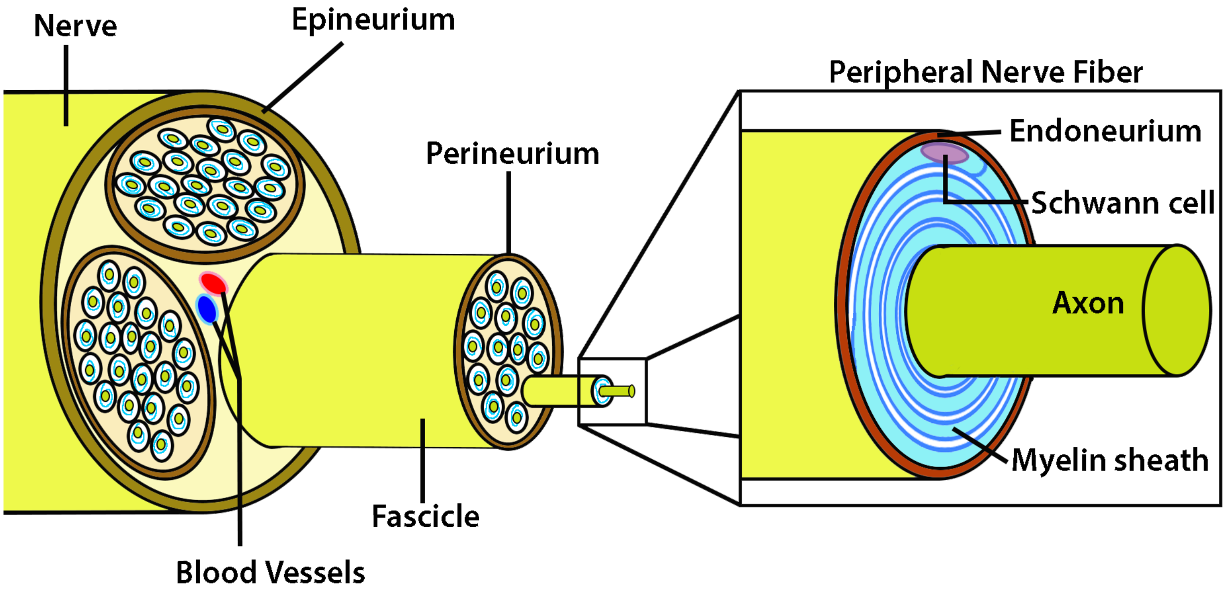

Figure 2-3: Peripheral Nerve Structure. Organization and structure of peripheral nerve from main branch to an axon. Note: (i.) Illustration is not to scale, (ii.) Afferent and efferent neurons are not delineated as their organization and structure are generally similar, and (iii.) Unmyelinated axons are also present in peripheral nerve but excluded from this diagram for sake of simplicity.

There are two types of neurons in the peripheral nervous system. Afferent neurons are sensory neurons that transmit sensory information from organs and limbs to the spinal cord in the central nervous system. As such, afferent neurons are responsible for the sensation of touch and pain as well as proprioception. Efferent neurons are motor neurons and are responsible for movement. These two types of neurons propagate signals in peripheral nerves via action potentials, and these signals could be viewed as the “messages” the CNS and PNS are sending back and forth to each other.

In peripheral nerves, an axon is surrounded by Schwann cells that cover segments of the axon and play a critical protective role. It should be noted that there are both myelinating and non-myelinating Schwann cells in peripheral nerve. The main function of myelinating Schwann cells is to form myelin that insulates the axon and yields faster conduction velocities. Non-myelinating Schwann cells are involved with maintenance of axons and could be seen as the “first responders” when an injury occurs in peripheral nerves[3]. The contribution of Schwann cells in the PNS is the hallmark difference from axons in the CNS, and their organization in peripheral nerves results in faster conductance of propagating signals in the PNS, as described below.

Increased conduction velocities in myelinated nerve fibers in the PNS are accomplished by a process referred to as saltatory conduction. Since myelin acts as an insulator for the axon, depolarization cannot occur in areas covered with myelin, but instead occurs at the Nodes of Ranvier. As such, action potentials form a local circuit that extends between Nodes rather than between adjacent patches of membrane and appear to jump along each node down the axon, which increases the rate of propagation of the action potential along nerve fiber. This process is important in nerve fibers as it increases the velocity of propagation and conserves the energy required for axons to depolarize and repolarize. Faster and more efficient signal transmission is important for peripheral nerves since they are generally long structures, originating at the spinal cord and extending to distal ends of limbs.

Another unique feature of peripheral nerves is the presence of connective tissue and collagen, which resides in the epineurium, perineurium, and endoneurium layers of peripheral nerve[4]. The main function of collagen in these layers serves to establish organization of the nerve fiber and maintain its integrity in situations of mechanical stress and stretching. The elasticity of collagen in healthy peripheral nerve allows for gross mechanical stretching and resistance to physical stress in load-bearing activities[5]. Collagen plays a pivotal role in the extracellular matrix of the basal lamina, which surrounds Schwann cells in peripheral nerve fibers, and serves major contributions to overall nerve formation[6]. For instance, it has been shown that without the formation of the basal lamina, Schwann cells fail to myelinate axons[7]. In addition to this, in cases of peripheral nerve injury, collagen production has been observed to sometimes surpass the ideal response and can obstruct the growth of regenerating axons[4], resulting in failed regeneration of damaged nerves.

Damage incurred to the axon, myelin, or connective tissues in peripheral nerve may lead to a loss of function and/or neuropathy. While many factors can lead to neuropathy, such as environmental (toxins), metabolic (vitamin deficiency), and inflammatory (abnormal immune response), the focus of this dissertation will concentrate on traumatic and genetic causes of peripheral neuropathy as detailed in the following sections.

2.1.2 Nerve Pathology of Trauma

The etiology of peripheral nerve trauma in the general public comes mostly from accidental injuries. These can vary in severity as some injuries may have occurred in the household during a home project, while other injuries may come from a severe automotive accident. Additionally, the Department of Defense has shown interest in treatment of traumatic peripheral nerve injuries (TPNI's) due to increasing reports of non-fatal limb injuries of service members, likely due to improvements of body armor that covers vital areas (i.e., head, neck, and chest) but may leave arm and leg areas more exposed.

When the peripheral nervous system is damaged via nerve degeneration following trauma, the nerve undergoes what is referred to as Wallerian degeneration at the site of injury[8]. In healthy motor axons, a neuron cell body with an axon extends to and connects to skeletal muscle fibers. Innervation of this neuron to its respective skeletal muscle fiber ensures proper motor function. Similar sensory deficits occur when sensory axons are damaged. In damaged nerves, reinnervation to skeletal muscle and sensory targets allows for action potentials to reach the target tissue and normal function is regained.

When the nerve is damaged, the site of injury along the axon undergoes gross microstructural reorganization[9,10]. This process is called Wallerian degeneration, whereby the distal portion of the nerve undergoes retrograde axonopathy from the injury site to the skeletal muscle fiber for motor axons. At this point, the axon is no longer connected to the skeletal muscle fiber and function is impaired. During Wallerian degeneration, Schwann cells signal macrophages by releasing cytokines such as chemokines to attract cells to the injury site. Present and recruited macrophages will infiltrate the site of injury and clean out damaged tissue that is distal from the injury site. This step of degeneration allows for the beginning of axonal regeneration, as the injured nerve begins to proliferate distally with the guidance of Schwann cells, allowing a tube of myelin sheath cells to form around the axon as it reinnervates to its target location. Full regrowth of the disrupted nerve is concluded once the axon has reached and reinnervated its target skeletal muscle fiber and sensorimotor function is regained[11]. An illustration of these steps in degeneration and regeneration are shown in Figure 4-1.

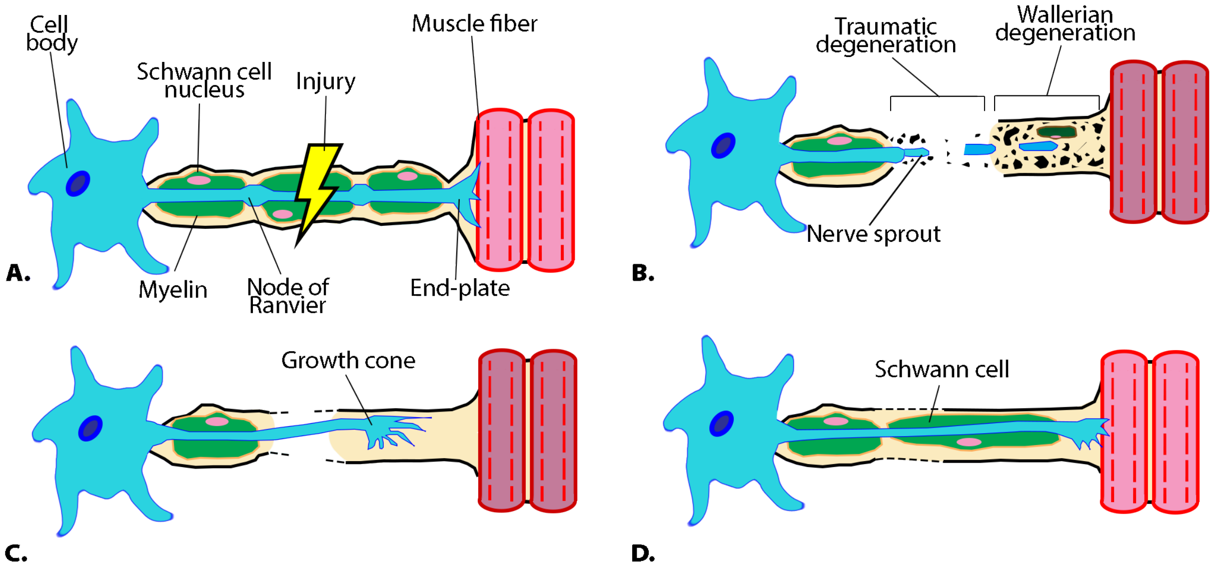

Figure 2-4: Wallerian Degeneration. A.) Healthy Nerve experiencing injury. B.) Wallerian degeneration occurs distal to injury site. C.) Damage tissue is cleaned out and growth cone projects towards target muscle fiber. D.) Schwann cell reforms after connection to muscle.

Secondary effects of Wallerian degeneration also impact muscle health. As injured nerves become severed from skeletal muscle fiber, denervated muscles will atrophy from non-use and fat will replace the areas where muscle-wasting has occurred. The functional result is muscle weakness. This is where clinical assessments (e.g., repetitive planter flexion, grip strength) prove most useful, as functional and behavioral testing of muscle strength can be compared to healthy values to assess degree of dysfunction. What these clinical tests fail to capture, however, is the manner in which nerve recovery is progressing prior to muscle reinnervation. As a result, these assessments only give us a snapshot as to an individual's degree of dysfunction. Knowing the degree of injury and regeneration can not only inform individual patient diagnoses but can inform the clinical management and prognosis of the injury.

In cases of traumatic nerve injury and recovery, it has been shown that regrowth of a nerve to its target muscle fiber occurs at a rate of 1 inch per month. In full nerve transection, we would expect to see the effects of Wallerian degeneration occur over weeks to months as damaged tissue is cleared and the axon grows towards its target location. However, milder compression injuries may not have the same process of recovery.

As a result, the surgical treatment and likelihood of recovery can vary substantially across different injuries. Toward this end, Sir Herbert Seddon identified three major classes of peripheral nerve injuries and pathologies in 1943[12]. Class I, Neurapraxia, is described as a brief loss of myelin surrounding the axon which results in a temporary block of nerve conduction, due to demyelination. Class II, Axonotmesis, involves the loss of the continuity of the axon and surrounding myelin, but with the epineurium and perineurium surrounding the nerve is still intact, maintaining the tract for target nerve recovery over time. Class II can also be described as axonal degeneration. Class III, Neurotmesis, is described as partial or full laceration of the entire nerve fiber with disruption of the epineurium, perineurium, and endoneurium layers, resulting in axonal loss. Damage to the epineurium layer usually results in no regrowth, while damage to the perineurium and endoneurium layers may result in poor to adequate regrowth[13].

In 1951, Sydney Sunderland further divided Seddon's Class III into three distinct categories that relate more closely to the surgical approach that is required for successful recovery[14]. Sunderland's first and second grades are described the same way as Seddon's Class I and Class II injuries, respectively. In Sunderland's third grade of injury, the first category of

Seddon's Neurotmesis, the epineurium and perineurium remain intact while the endoneurium is damaged, and while this may recover on its own, surgical intervention may be necessary in some cases. Sunderland's fourth grade of injury, the second category of Seddon's Neurotmesis, describes cases when the perineurium and endoneurium are damaged and only the epineurium remains intact. In these cases, surgical intervention is absolutely necessary. Finally, Sunderland's fifth grade of injury, the third category of Seddon's Neurotmesis, describes complete transection of the nerve, and recovery is not possible unless surgery is performed to reconnect the distal end of the injured nerve to its respective proximal end[15]. An illustration showing grades of injury is shown in Figure 2-4.

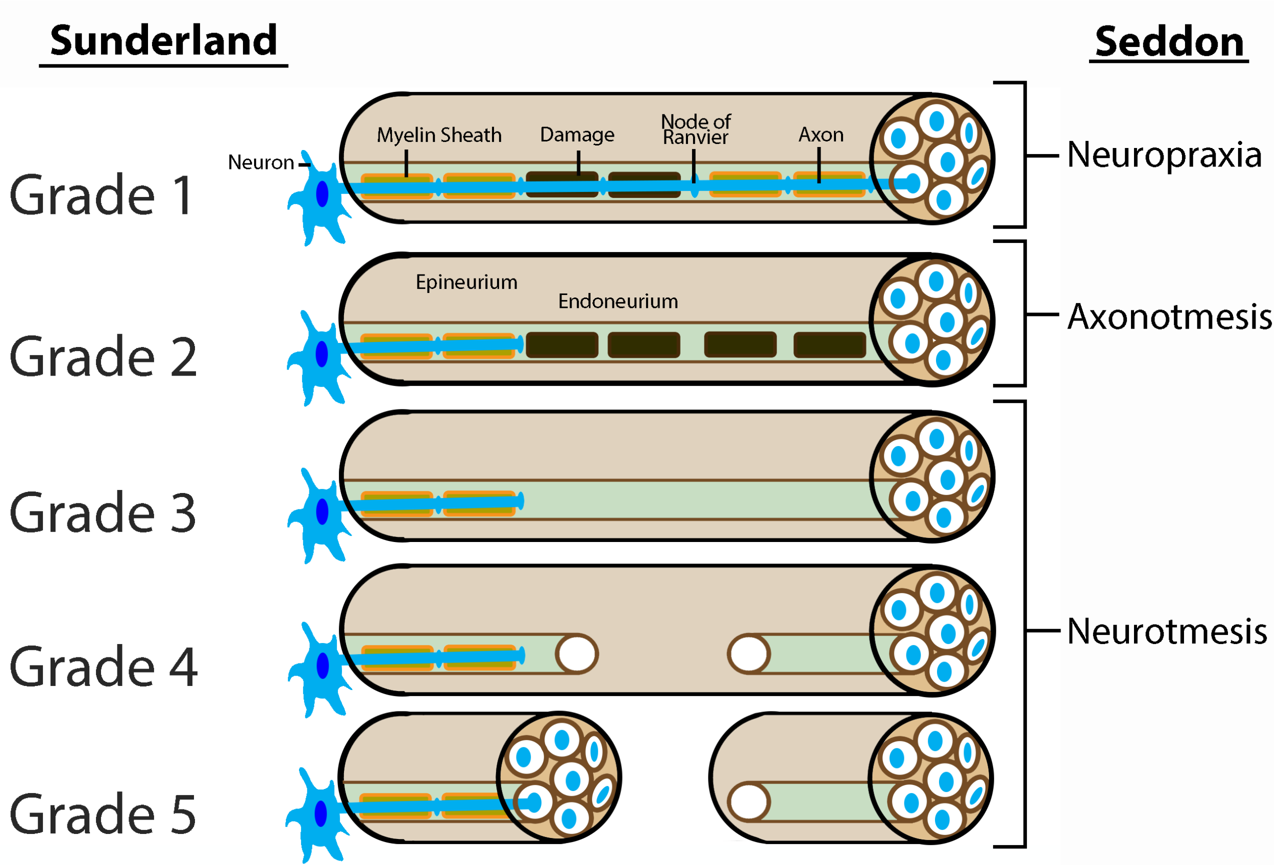

Figure 2-5: Seddon and Sunderland scales classifying nerve injury. Sunderland scales are shown on left and Seddon classifications shown on right. Neurons, Nodes of Ranvier, and Axons are shown in blue. Orange rectangles represent healthy myelin sheaths. Dark rectangles represent damaged/demyelinated sheaths. Illustration is not to scale.

The Seddon and Sunderland scales are to this day used in current clinical practice to assess the degree to which trauma has occurred and what surgical and/or treatment strategies would best benefit the patient with consideration to the anatomy of the damaged nerve. However, these classifications only pertain to cases of peripheral nerve injury and/or trauma. For example, in cases where genetic factors lead to a chronic progressive neuropathy, there are other assessments that provide for specific clinical information on disease progression.

2.1.3 Nerve Pathology of Inherited Disease

Peripheral nerve health can also be affected by the onset of inherited neurological diseases, or inherited neuropathies, which directly impact the microstructural formation of nerves. Charcot-Marie-Tooth (CMT) disease is a general term used for a set of inherited neuropathies that is caused by a genetic mutation that affects neuronal formation and growth in peripheral nerves. This disease was coined by those who first classically described the disease: Jean-Martin Charcot, his student Pierre Marie, and later by Howard Henry Tooth. CMT1- diseases are characterized by de/dysmyelinating, while CMT2- are characterized by primarily affecting axons, and each of these characterizations are further subtyped by their specific genetic mutation.

The most common subtype of CMT, CMT1A, results from duplication of a region on chromosome 17p11.2 that encodes for peripheral-myelin-protein 22 (*PMP22*). The duplication of this part of the chromosome results in abnormal Schwann cell formation and demyelinated axons, which slows nerve conduction velocity from axon to axon and reduces the propagation of action potentials to muscle. The response to demyelinated PNS axons is to remyelinate them, however, in CMT1A, this cycle of demyelination and remyelination occurs more rapidly than normal. This results in layers of Schwann cells surrounding the axon, resulting in nerves that appear thicker and larger in circumference due to the proliferation of Schwann cells layers, coined as the “onion bulb” presentation. This chronic de/remyelination also results in secondary axonal degeneration and impedes the ability of neurons to reinnervate target muscle fibers. This results in denervated muscles that will atrophy over time, reducing the quality of life for individuals with this disease by requiring assistance for walking and aid in performing common household tasks. CMT2A is a more aggressive disease and primarily affects axons, as opposed to a primarily de/remyelinating disease. CMT2A results from mutations in the mitofusin 2 (*MFN2*) gene. While CMT1A and CMT2A are provided as examples, other forms and subtypes of CMT exist and are named by their respective genetic origin.

For example, deletion of this same *PMP22* gene involved in CMT1A results in and a much less common disorder referred to as Hereditary Neuropathy with liabilities to Pressure Palsies (HNPP), which is the specific disease of focus for Chapter 5. This mutation results in numbness, tingling, and general weakness of muscles in the limbs; problems with touch, pain, and temperature sensations; as well as a high sensitivity to mechanical pressure. Pathologically, this results in the abnormal thickening of myelin sheaths, or "tomacula". If we take into consideration the other diagnostic tools (i.e., family history, nerve conduction studies, physical exam), CMT/HNPP disease are generally differentiated clinically from similar neuropathies (i.e., diabetic neuropathy) by genetic testing.

It is worth noting that while life expectancy is not diminished in the majority of HNPP cases, quality of life is greatly affected, as expensive home-care may need to be implemented for an individual. In addition, the risk of falls greatly increases from difficulty walking, which could lead to other life-threatening injuries like broken bones. For an individual with this disease, there are typically expensive costs associated with hiring an at-home care professional, installing handicap rails in the shower and chair lift on stairs, and having driving assistance provided in order to meet orthopedic and clinic visits. This becomes an increasing burden on the individual if there is no family support system already available to mediate these expensive costs.

2.2 Clinical Assessment of Peripheral Nerves

2.2.1 Nerve Conduction Studies & Electromyography

The most common clinical tests of peripheral nerve health and function include nerve conduction studies (NCS) and electromyography (EMG). Although these tests measure different aspects of nerve function, they are often employed at the same time to make a diagnosis. NCS evaluates the quality of electrical conduction in the affected nerve(s) of a patient displaying symptoms. Four components of the NCS describe different ways in which a nerve could be affected: Motor NCS, Sensory NCS, F-wave study, and H-reflex study. Motor NCS is conducted by electric stimulation of a peripheral nerve and recording the time or latency (in milliseconds) it takes for that electrical stimulation to reach its target muscle. The motor response in this task is referred to as compound muscle action potential (CMAP), which will have a lower amplitude in damaged nerve, reflecting neurodegeneration[16]. Sensory NCS are performed similarly with electrical stimulation of a peripheral nerve, but the signal recorded is selected from a sensory nerve, such as the skin, and measured in microvolts (μV). The sensory response in this task is called sensory nerve action potential (SNAP), which also reflects neurodegeneration with lower amplitudes. Latency and distance from the stimulation to the recording site are also calculated to estimate conduction velocities, which relate to myelination. Both F-wave and H-reflex studies derive latency measures of the time it takes for an electrical stimulation to travel from the stimulating electrode to the spinal cord and back, which can give clinicians some indirect information on proximal neuropathies.

While NCS captures nerve fiber connections, and how these connections interact with the spinal cord, needle electromyography (EMG) provides specific details on muscle spontaneous and/or evoked muscle activity by inserting the EMG needle into the muscle directly[17].EMG can distinguish myopathic from neurogenic muscle weakness, focal from plexus pathology, and axonal degeneration from demyelination by metrics of spontaneous activity and motor unit recruitment[18]. Spontaneous activity detects acute denervation through fibrillations, positive sharp waves, and complex repetitive discharges. In nerve trauma, denervated muscle fiber becomes supersensitive and will discharge or fibrillate and can be detected with the EMG needle. Positive sharp waves occur when the needle tip damages muscle fiber and action potentials will propagate up to and terminate on the EMG needle. Complex repetitive discharges are indicative of neurologic disease and would not be used to assess trauma. Motor unit recruitment measures the amplitude, duration, number of phases, and firing rate of motor units. In a minimal muscle contraction, one to a few motor units will be recruited. In a maximal muscle contraction, more units are recruited and action potentials will appear to overlap and interfere with each other. This is also referred to as interference pattern or recruitment pattern.

In cases where NCS/EMG are non-responsive, which is often true in cases of trauma (where nerve is severed) or in length-dependent inherited neuropathies (where distal axons are lost), skin biopsies may be collected from the surface of the skin to evaluate the small sensory nerve fibers of the skin[19]. The main limitation in this method is that information on only sensory nerves are reported and motor information is not included. Biopsy of the nerve itself is not well tolerated as it may create more nerve problems those that were already present. In cases where no clear cause for disfunction is determined by NCS or EMG, a sural nerve biopsy can be performed to assess any global neuropathy that affects the body. The sural nerve is chosen because it is a purely sensory nerve with no motor loss associated with biopsy trauma, it is superficial and easy to locate on the body across patients, and its target sensory area is at the dorsolateral area of the foot,[20] which doesn't leave patients as debilitated as other nerve perturbations. However, the primary limitation mentioned before still exists in sural nerve biopsies, as it only will show myelination fibers for sensory neurons since no motor neurons are present in the sural nerve.

2.2.2 Functional and Behavioral Testing

Clinical examinations of peripheral nerve degeneration are limited to tests that assess overall function and perception of difficulty reported by the patient. While many tests exist, a few will be covered herein for context into the clinical decision-making that occurs and what tools are currently used to inform clinicians and surgeons on proper treatment strategies. Overviewing these tests will provide a proper interpretation of patient measures given in the upcoming chapters.

The Michigan Hand Outcomes Questionnaire (MHQ) is a composite score that includes measures for: overall hand function, daily living activities, work performance, pain, aesthetics, and satisfaction[21]. This test is carried out on the affected arm, or in cases of bilateral injury both arms are tested. Patients answer questions on a 5-point Likert Scale, with higher scores indicating better hand performance. The overall MHQ score is calculated by averaging the scores together for all scales, with lower overall scores indicating poor functioning and higher overall scores representing healthy functioning[22]. The MHQ has been used to assess upper extremity injuries for over the past 20 years and has proven itself to be a reliable, valid, and replicable instrument in clinical practice[23]. Unfortunately, there are limitations with this test when assessing the degree of injury that occurs immediately following a traumatic event, such as in the case of acute compression and full laceration will present identical symptoms at the onset of nerve recovery. In addition, this measure fails to give information as to the regeneration of nerves, and only serves as a representation of what the patient thinks and feels about their injury within a certain context.

The Grip Test is a clinical test of grip strength and upper limb function, which is performed with a handgrip dynamometer. For a traumatic injury, the Grip Test is usually deferred until resistive exercises are approved by the patient's physician so as to not disrupt the patient's healing and give reliable measures. The score for a standard grip test procedure is derived by calculating the mean from three grip strength trials. The Grip Test has proven reliable and valid[24–26], and also has an established table of normative values by age[27]. The main limitation of this assessment is that injuries that have not fully healed cannot be subjected to restrictive tests that may extend the process of healing, which is more common in cases of traumatic injury. This limitation means that this clinical information may be recorded only after a certain amount of time has passed, possibly after nerve recovery has occurred. Therefore, more specific information on regeneration of nerves is not captured by this technique, but only the secondary effects of healing in distal areas may be witnessed and recorded.

Nine-Hole Peg Test (NHPT) is used to measure upper limb dexterity and was initially developed by Kellor et al. in 1971 for use in neurological diagnoses, such as stroke, Parkinson's, and brain injury[28], and has since been validated and applied to other diseases[29–31]. The NHPT administration tasks participants to place and remove nine pegs into nine holes, respectively, in the least amount of time possible. The NHPT score represents the time in seconds it takes for participants to complete the task. Its advantages include the test is relatively inexpensive and can be administered in a short amount of time. In the context of nerve regeneration following trauma, the NHPT provides little information prior to muscle reinnervation, as the outcome measure reports on the behavioral aspects of the injury. In addition, multiple pathological factors (e.g., muscle atrophy, axonal degeneration, demyelination) can impact performance, which minimizes the specificity of the test.

Another clinical assessment of peripheral nerve degeneration that has been developed specifically for inherited neuropathies is the Charcot-Marie-Tooth Neuropathy Score (CMTNS). The test was initially developed in 2005 as a reproducible and inexpensive method of measuring natural history and response to therapy and was based largely on the Total Neuropathy Score (TNS), which was developed in 1999 for detecting and quantifying peripheral neuropathies. Parameters of the CMTNS include sensory symptoms, motor symptoms for arms and legs separately, pinprick sensibility, vibration, strength for arms and legs separately, median and ulnar nerve CMAP (mV), and radial SNAP amplitude (µV)[32]. All of these measures are combined for a composite score that related to degree of disease disability. Limitations for this test include the time it takes to administer to a patient, its low responsiveness to change over 2 years, and floor and ceiling effects in some of sub-score measures[33].

2.2.3 Limitations of Current Assessments and the Need for Imaging

In all of the clinical functional and behavioral assessments, limitations exist (e.g., subjective, floor/ceiling effects, limited to distal nerves, unavailable in some cases) as to the information they afford physicians and surgeons. Therefore, new methods are needed to overcome these obstacles. While ultrasound has been a standard radiological assessment of nerves that lie within a 5 cm deep from the skin surface, magnetic resonance imaging (MRI) provides assessment for proximal nerves that are more medial in the body, such as the sciatic nerve of the thigh. Many applications of MRI have been developed for the brain, and while some have been translated to the peripheral nervous system, there are still many unexplored areas for applying these methods to a new area of the body. MRI as a non-invasive assessment that is sensitive to aspects of nerve pathology that may improve clinical decision-making in areas where current clinical measures fail to provide relevant information. Developing methods to provide quantitative data in the PNS with MRI can give more specific biological outcomes that relate not only to severity, but progression over time. MRI also affords us the ability to look at deep structures with high resolution that would not be possible otherwise. In the following two chapters, we will provide an overview of MRI and some of its' techniques that have been developed and proven useful for assessing nerve degeneration in the studies detailed in the following chapters.

CHAPTER III

MAGNETIC RESONANCE IMAGING

3.1 Magnetic Resonance Imaging Overview

3.1.1 Basics of MRI

Magnetic Resonance Imaging (MRI) is a medical imaging technique that uses strong magnetic fields and radio waves to create images of tissues and organs within the body. These images can give medical professionals an unparalleled insight into the body, which has dramatically changed how we approach treatment for multiple diseases and injuries. MRI has its roots in nuclear magnetic resonance (NMR), which has been used historically to look at the structure and dynamics of organic molecules in pharmaceutical drugs research, environmental science, and materials research[34–38]. Felix Bloch, Edward Purcell, Raymond Damadian, Paul Lauterbur, and Peter Mansfield are all credited for contributing to what has evolved into modern MRI today, with many receiving a Nobel Prize for their specific contributions[34,39–42]. In this section, an overview of the basic principles of MRI and specific techniques that are applied in this dissertation will be disseminated.

In the first section of this chapter, we established that the body is composed of multiple systems that integrate with each other to form our experience of the world, and that each of these systems are responsible for specific organs within the body. If we continue breaking down these systems into their respective parts, we find that organs are composed of specific tissues, and these tissues are composed of specific cells that relate to function. These cells can be broken down into molecules that determine the composition of the cell, and those molecules can be separated into their atomic constituents.

Atoms are composed of charged particles, protons and electrons, and uncharged particles, neutrons. All particles have a fundamental, quantum property known as spin. Within nuclei, protons and neutrons tend to “pair up” and cancel out each other’s spins, resulting in only nuclei with an odd number of protons/neutrons possessing net spin angular momentum, which can take on zero, whole, or half integer values.

The hydrogen nucleus (^{1}H) is studied primarily in MRI because it possesses a spin angular momentum of ½ and the body is abundant in hydrogen, as it is composed mostly of water and adipose tissue. The human body is composed of 70% water and a water molecule is composed of two hydrogen and an oxygen atom (H_2O). Triglycerides are composed a glycerol backbone that is connected to three fatty acid hydrocarbon chains. Triglycerides are stored in adipocytes, which store energy as fat and are the primarily composition of adipose tissue. Since water and adipose tissue contain large amount of hydrogen, it is possible for us to quantify the abundance of these molecules in human tissue with MRI. Furthermore, applications for measuring the effect of tissue barriers to water diffusion, measuring the ratio of water molecules and macromolecules, as well as quantification of fat and water in tissue will be discussed in the latter part of this section, which will tie in heavily to the other chapters of this dissertation.

At the center of a hydrogen atom is a single proton that possesses charge and spin. This charged spin can be thought of classically as creating a current loop around the proton, which induces a magnetic field perpendicular to the axis of rotation that gives rise to a magnetic moment ($\vec{\mu}$). When a static magnetic field ($\vec{B}$) is externally applied, the magnetic moment of the single particle will experience torque or rotation about this static magnetic field. This can be described as the time rate of change of the magnetic moment orientation via the following equation of motion:

$$\frac{d\mu}{dt} = \gamma\vec{\mu} \times \vec{B}, \tag{3.1}$$

where γ represents the gyromagnetic ratio, $\vec{\mu}$ represents the magnetic moment vector of a single particle, and $\vec{B}$ represents the magnetic field vector. The gyromagnetic ratio (γ) is the ratio of the magnetic moment of a given atomic particle and its spin angular momentum. The gyromagnetic ratio for a hydrogen proton is γ = 42.58 MHz/Tesla (T). The formula simply states that the rate of change of the magnetic moment is proportional to the cross-product of the magnetic moment and the externally applied magnetic field, which results in a torque (or precession) when these two are not aligned.

Rather than focus on a single particle, in MRI we look at the ensemble of particles. When this ensemble of particles possessing spin are placed in an external magnetic field, the spins will align with the magnetic field in a state that is either parallel (α, low energy state) or anti-parallel (β, high energy state) to this field. The ratio of spins in each energy state is governed by the Boltzmann distribution. As the magnetic field strength increases, we see a larger separation in energy levels between α and β, and this larger separation of energy states the basis for use of higher magnetic field strength for MRI machines (i.e., 3 T, 7 T, etc.). The parallel and anti-parallel hydrogen nuclei will cancel each other out by having equal and opposite magnetic moments, but there will always be some excess parallel hydrogen nuclei. The vector sum of these nuclei's magnetic moments is the net magnetization vector ($\vec{M}$). Similar to the individual nuclei described above, when $\vec{M}$ is placed in an external magnetic field, it also precesses about this field. This phenomenon can be thought of as similar to the precession of a spinning top about the gravitational field direction. Once again, an external field produces torque on $\vec{M}$, and the rate at which this precession can be shown to be governed by the Larmor equation:

$$\omega = \gamma B, \qquad [3.2]$$

where omega (ω) is the Larmor frequency, gamma (γ) is the gyromagnetic ratio, and B is the amplitude of the magnetic field.

Knowing the Larmor frequency of the net magnetization vector allows us to selectively excite/differentiate a proton for a given molecular environment. This was the main contribution of both Felix Bloch and Edward Purcell, who independently verified that the manipulation of magnetic spins that resonate at a given frequency by applying a frequency pulse that corresponds to the energy difference between α and β energy states[35,39] (or the Larmor frequency). More specifically, when $\vec{M}$ is aligned with B_0, the spins in a magnetic moment are at a state of equilibrium. In MRI, we use an applied magnetic field (B_1) to perturb this equilibrium and create coherent transverse magnetization that we can detect. The frequency of B_1 will be in the radiofrequency (RF) range and is referred to as the "applied RF field" in an MRI experiment. B_1 fields are applied perpendicular to the direction of B_0, and the duration that B_1 is applied will determine the flip angle (designated by θ).

In summary, $\vec{M}$ is the result of an ensemble of spins interacting with a constant external field (B_0). After net magnetization is created in parallel to B_0, it is then possible to perturb $\vec{M}$ with another applied RF field near the Larmor frequency for a given molecule. Once turned off, $\vec{M}$ will "relax" back to its equilibrium state, and we can get information as to the type of tissue based on the rate at which the net magnetization returns to equilibrium with B_0. The effects of relaxation in an MRI experiment will be covered in the following section.

3.1.2 Relaxation

Once the RF pulse is turned off, $\vec{M}$ will "relax" back to its lower energy equilibrium state and coherent magnetization will decay. This process has two components: longitudinal (or spin-lattice) and transverse (or spin-spin) relaxation, which are described by T_1 and T_2 time constants, respectively. Alternately, relaxation is often described via rate constants $R_1 = 1/T_1$ and $R_2 = 1/T_2$. The phenomena of how net magnetization changes over time due to the application of RF pulses (as described in the previous section) and these relaxation processes can be described with the Bloch equations[34]:

$$\frac{dM_x(t)}{dt} = \gamma\left[M_y(t)B_0 - M_Z(t)B_{1_y}\right] - \frac{M_x(t)}{T_2} \qquad [3.3]$$

$$\frac{dM_y(t)}{dt} = \gamma\left[M_z(t)B_{1_x} - M_x(t)B_0\right] - \frac{M_y(t)}{T_2}$$

$$\frac{dM_z(t)}{dt} = \gamma\left[M_x(t)B_{1_y} - M_y(t)B_{1_x}\right] - \frac{M_z(t) - M_0}{T_1}.$$

Here, subscripts *x*, *y*, and *z* represent magnetization along the cardinal axes in three-dimensional space, *t* represents time, B_0 is the static magnetic field, M_0 represents the equilibrium magnetization, B_1 is the applied RF field, T_1 is the longitudinal component of relaxation, and T_2 the transverse component. The measured signal we achieve from a majority of MRI experiments is the result of time-varying phenomena described by these equations.

The easiest way to evaluate the solutions to the Bloch equations is through examining the result of specific sequences. For example, the restoration of longitudinal magnetization equilibrium after a 90° pulse can be described with the following formula:

$$M_z(t) = M_0\left(1 - e^{-\frac{t}{T_1}}\right). \quad [3.4]$$

In addition, the decay of transverse magnetization following this same pulse is described as

$$M_{xy}(t) = M_0 e^{-\frac{t}{T_2}}, \quad [3.5]$$

where $M_{xy}(t)$ represents transverse relaxation as a function of time. The rates of T_1 and T_2 for white and gray matter in the human brain at 3T are illustration in Figure 3-1.

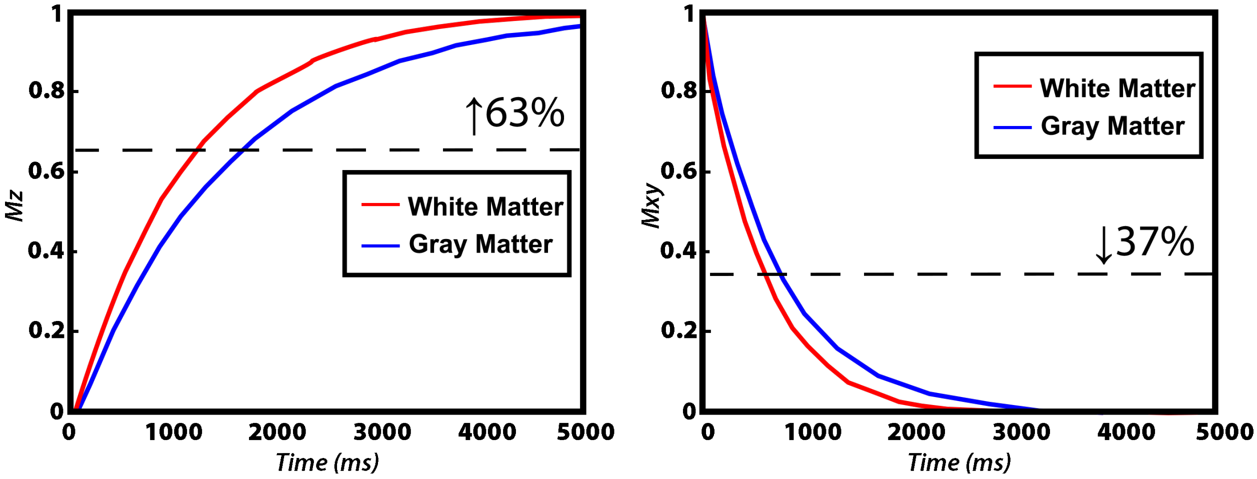

Figure 3-1: T_1 and T_2 relaxation in the brain. T_1 recovery (left) and T_2 decay (right) curves for white matter (red) and gray matter (blue). Milliseconds (ms). Values illustrated here are taken from literature at 3 T[43]. T_2 represents the time it takes for transverse relaxation to fall 37% from its initial value, while T_1 represents the time it takes for longitudinal magnetization to recover to 63% of its equilibrium value.

Relaxation varies across tissue types primarily based on random molecular tumbling of water molecules and their interaction with the local molecular environment within the tissue itself. For instance, white matter in the brain has more large macromolecules than gray matter, and as such, T_1 and T_2 values are shorter for white matter at 3 T (White matter: T_1 = 1110 ms, T_2 = 56 ms; Gray matter: T_1 = 1470 ms, T_2 = 71 ms)[43]. This is due to white matter being mostly myelinated axons and gray matter being mostly neuronal cell bodies[44]. Thus, we understand the variation of relaxation times in different tissues as mostly reflective of interactions between water molecules in the tissue environment. It's worth mentioning that T_1 and T_2 relaxation rates can also be affected by certain disease, such as iron deposits in diseased liver[45]. Additionally, field strength can also drastically affect T_1 relaxation rates but has a smaller effect on T_2 [43]. It should be noted that the experiments in this dissertation all occur at 3 T, and any mention of high field strengths are for explanatory purposes.

The signal we collect in an MRI sequence is referred to as an echo. As such, the echo time (TE) is the time in between the initial RF pulse and the peak (or center) of the echo signal, during which the coherent magnetization decays. The repetition time (TR) refers to the time between consecutive excitation pulses, during which time longitudinal magnetization is restored. After excitation, the signal decays according to T_2^* (i.e., effective T_2 in the presence of magnetic field variations) and a gradient-echo is formed when the area under the read gradient is zero (more detail in Section 3.2.2). In a spin echo (SE) pulse sequence, the accelerated signal loss due to magnetic field variations is rephased with a 180° pulse applied halfway between excitation and TE, which generates a so-called spin-echo that decays according to T_2 (more detail in Section 3.2.1). This concept can be expanded to efficiently acquire multiple echoes per TR (via multi-echo sequences. For example, multi-echo gradient-echo sequences involve a series of dephasing and rephasing read gradients to generate multiple gradients echoes within a single shot, which can be used to determine fat and water contributions and estimate T_2^* (more detail in Section 3.2.3). Thus, pulse sequence design and timing of parameters are important in generating different types of contrast.

3.1.3 Image Formation

To obtain images that yield contrast from T_1 and T_2 relaxation in an MRI experiment, we require a receiver coil to detect the coherent transverse magnetization after an RF pulse. Faraday's law of induction states that a change in the magnetic field will induce voltage in a conductor close to the field. As such, the receiver coil allows us to acquire measurements of signal intensity over time. Thus, when we conduct an MRI experiment, it is the receiver coil that detects the MR signal and further computations must be done to assess where the signal is located and translate that information into an image. In this section, we will briefly overview the processes involved for spatial encoding and image formation.

In the previous sections, we discussed how protons are manipulated in an MRI experiment. The next step is to localize this phenomena to gain understanding of tissue composition. To accomplish this, we need to spatially encode the information we get from an MR scanner through the use of magnetic field gradients. Gradients are loops of conductive wire that surround the bore of an MR scanner, with three sets of gradient coils for localizing signals in the x, y, and z directions respectively. When the gradients are turned on, the magnetic field will change linearly as a function of position depending on the amplitude and direction of the applied gradients. When these gradients are on, this results in a spatial variation in frequency (according the Larmor equation) that can be detected by the receiver coil. In an MRI experiment, signals are measured with different gradient amplitudes and/or durations (or spatial frequencies) and directions in this frequency domain, which is often referred to as k-space. The Fourier Transform (FT) is then applied to convert k-space information into an image that shows signal intensity as a function of its position in space.

This concept is described in more detail in the MRI pulse sequence in Figure 3-2, which describes the timing of the RF pulses and gradients required for image formation. We will introduce pulse sequences in more detail in the following sections, but for now we will limit the discussion by giving a simple example to explain how we travel through k-space. In this sequence, an RF pulse is applied to generate coherent transverse magnetization and gradients are applied to sample different spatial frequencies, which can be thought of as moving through k-space. In Figure 3.2, we see the gradient for the x-direction (also called frequency encoding gradient or readout gradient) is applied simultaneously as the gradient for the y-direction (also called phase encoding gradient). For a cartesian grid, this would move the k-space position from the center to the top-right of k-space. Next, another x-direction gradient is applied with the opposite polarity, during which a gradient echo is formed and one line of k-space is sampled, or “filled out”. Extending this to cover the remainder of the Cartesian grid is performed by repeating this experiment at different y-gradient amplitudes to fill out all lines of k-space needed for image formation.

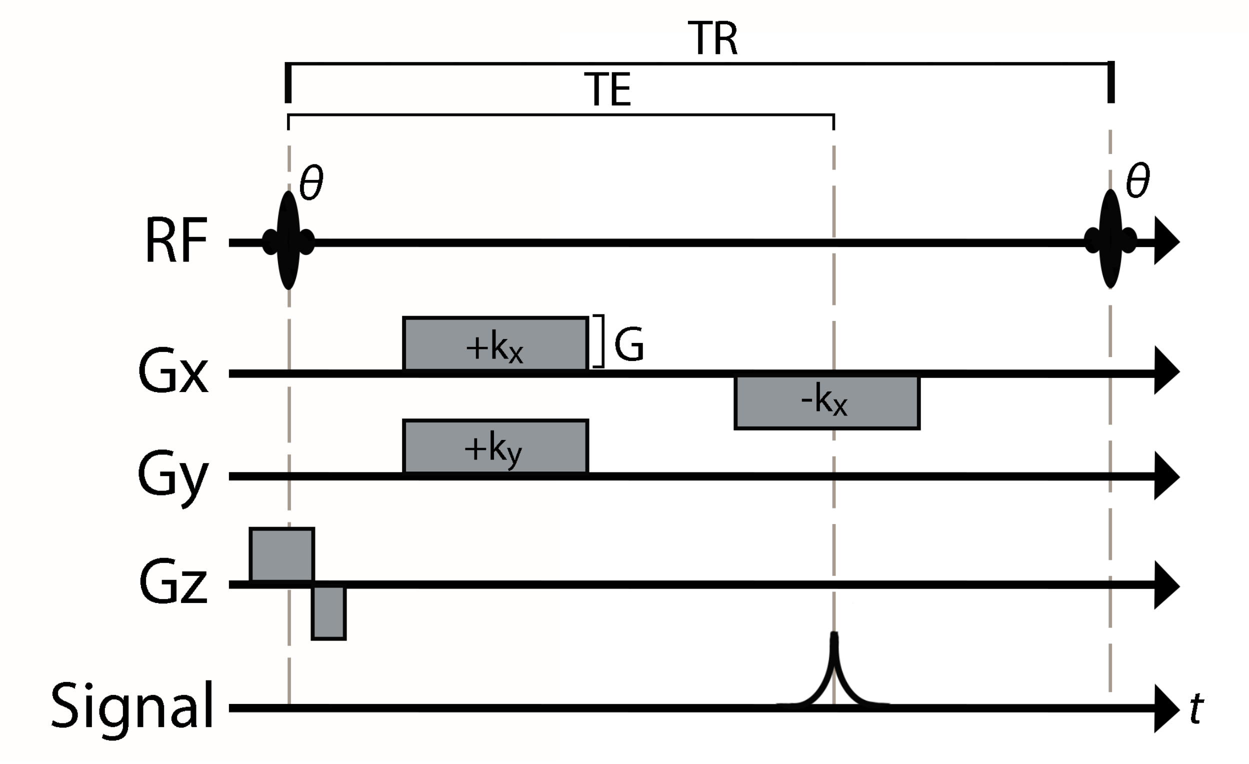

Figure 3-2: Simple Pulse Sequence. *TR* for repetition time, *TE* for echo time, *RF* for radiofrequency pulse, theta (θ) for flip angle, *G* for strength of gradient, *Gx* for gradient in x-direction, *Gy* for gradient in y-direction, *Gz* for gradient in z-direction, *t* for time. Trajectories moving positive (+) or negative (-) per k-space direction (k_x, k_y).

There are many ways in which we can choose to cover k-space, and these approaches are referred to as k-space trajectories. Standard trajectories simply acquires each k_y line during each repetition time, or TR. This approach is often too slow and is sensitive to motion between TRs. Echo Planar Imaging (EPI) addresses this by acquiring multiple lines of k-space per shot. This was first described by Sir Peter Mansfield[46] and useful in fast acquisitions like fMRI and acquisitions that are sensitive to motion like DTI. Non-cartesian (e.g., spiral trajectories) have also been shown to be useful in ultra-fast 3D acquisition and can reduce motion as well as field distortions[47]. While many other approaches exist, as well as many options within each approach, the few examples provided herein should shed light to the reasons why we chose the various readout for our experimental studies in nerve. As we've moved from basic MRI physics, to spin relaxation and image formation, the remainder of this section will be dedicated to specific contrast mechanisms used for studying pathology in this dissertation.

3.2 Quantitative MRI Techniques

3.2.1 Basics of Diffusion MRI

Botanist Robert Brown observed what we now refer to as "Brownian Motion" in 1827 while witnessing naturally pollen vibrate under a microscope. In 1905, Albert Einstein showed that molecular diffusion is the result of Brownian Motion. Molecular diffusion describes the random motion of molecules that results from their inherent thermal energy. In an environment where there are no barriers (i.e., a "free" environment), displacement will occur in three-dimensions and follow a Gaussian displacement probability distribution. The diffusion coefficient (D) describes the rate at which this process occurs over a period of time. For example, in the "free" environment scenario mentioned previously, absence of barriers and boundaries will allow molecules to travel freely in all directions over time (i.e., isotropic) and the diffusion coefficient of water molecules (at 37°C) would be 3×10^{-9} m^2/s^{-1}, resulting in a mean-squared displacement of approximately 17 µm over 50 milliseconds [48]. However, in biological tissue, water molecules encounter restrictions such as cell walls, membranes, myelin sheaths, and macromolecules which impede their motion in tissue, resulting in reductions in this mean-squared displacement. This results in diffusion becoming time and direction dependent only if the underlying spatial restrictions to diffusion are anisotropic. Applying a diffusion gradient along different directions during an MRI experiment sensitizes the diffusion of water molecules along these directions and allows us to create contrast in our images that is sensitive to these microstructural processes.

The most notable early application of this method to study human physiology was a technique called Diffusion Weighted Imaging (DWI)[49]. The pulse sequence for this technique was pioneered from Stejskal and Tanner, who made image contrast possible with the implementation of a diffusion gradient[50,51].

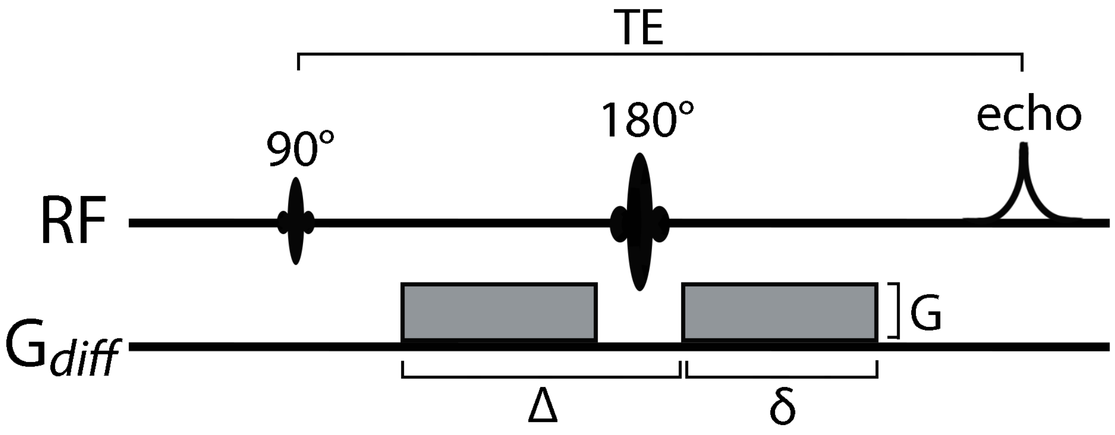

Figure 3-3: Pulse sequence for PGSE scan from Stejskal & Tanner. Gradients shown applied to one direction for the purpose of illustration. G_{diff} represents strength of diffusion gradient. Uppercase delta (Δ) represents the difference in time between diffusion gradients, with lowercase delta (δ) representing gradient duration.

A typical Stejskal and Tanner diffusion sequence (Figure 3-3), or pulsed gradient spin echo (PGSE), can be described as follows: (i.) a 90 degree RF pulse is applied to generate coherent transverse magnetization, (ii.) a gradient introduces phase to water protons (i.e., tag spins), (iii.) a 180 degree RF pulse is applied to refocus the spins of protons and minimize losses due to variations in B_0, then (iv.) a second gradient is played that reverses the phase of the first gradient (i.e., untag spins). Stationary protons experience opposite and equal gradients and no signal loss.

However, diffusing molecules that are not stationary between diffusion gradients will not be in their original location at the end of the second gradient, resulting in phase difference during these two gradients and a loss in signal intensity. The observed signal in a DWI experiment then is related to the diffusion weighting applied and the amount of diffusion the water undergoes during the diffusion time. The contrast provided by DWI has had an extensive history of clinical applications in the fields of brain imaging and oncology[52].

In a diffusion experiment, a PGSE sequence is typically acquired first without the gradients, resulting in a non-diffusion-weighted, or "b_0", image that is used to normalize the diffusion weighted acquisition and estimate the diffusion parameter maps. Next, the sequence is run with the gradients at a particular strength, direction, and duration (or diffusion-weighting), referred to as "b-value". DW data, normalized by the b_0 acquisition, can be combined to estimate the apparent diffusion coefficient (ADC) in a given direction. In addition, the gradients can be applied in different directions and combined to create trace diffusion-weighted images. Trace DWI and ADC maps have been implemented clinically to study stroke, which was pioneered by previous work that established DWI as clinically relevant from Le Bihan et al., Taylor et al., and Merboldt et al. as early as 1985[48,53,54]. When MRI scanners arrived with EPI, acquisition for diffusion scans became feasible in a clinical setting, leading to widespread adoption of these techniques.

Further advancements have occurred in diffusion MRI where calculation of directional tensors are estimated and fiber tracts are reconstructed to explore in vivo microstructure[49]. For example, diffusion tensor imaging (DTI) is an advanced DWI technique that gives us additional information as to the anisotropy of water diffusion in tissue, and is currently a well-established method for investigating white matter microstructure in the human brain[50,55]. In this technique, diffusion is not explained by a single coefficient, but instead by direction-dependent diffusion coefficients. Basser et al. established the formalism for quantifying diffusion properties as a tensor by constructing an orthogonal system based on principle directions of diffusivity in three dimensional space[56]. The resulting diffusion tensor:

$$\mathbf{D} = \begin{bmatrix} D_{xx} & D_{yx} & D_{zx} \\ D_{xy} & D_{yy} & D_{zy} \\ D_{xz} & D_{yz} & D_{zz} \end{bmatrix} \qquad [3.6]$$

is a 3x3 matrix that defines diffusion along the orthogonal axes in the laboratory frame. In this tensor, the diagonal elements account for diffusion along these axes and the off-diagonal elements accounts for the correlations in the diffusion coefficients between axes. Recall that diffusion is often impeded by cell membranes, resulting in anisotropic and/or hindered diffusion that occurs along various directions as described by **D**[57]. Since D is symmetric (D_{xy}=D_{yx}, D_{zx}=D_{xz}, and D_{zy}=D_{yz}), it only has six independent parameters. As a result, a minimum of six gradient directions and a single non-diffusion-weighted image and are required to estimate the parameters in **D**. Once calculated, **D** is often decomposed into eigenvectors (noted with epsilon: ε1, ε2, ε3) that define the local frame of reference within the tissue (with ε1 representing the direction with fastest diffusion); and corresponding eigenvalues (noted with lambda: λ_1, λ_2, λ_3) that define the diffusion coefficients within this frame of reference.

These eigenvalues are often used to calculate scalar indices that quantify anisotropy, including the fractional anisotropy (FA), mean diffusivity (MD), axial diffusivity (AD), and radial diffusivity (RD). Mean diffusivity is calculated the same way as the ADC maps previously mentioned ($MD = (\lambda_1 + \lambda_2 + \lambda_3)/3$) . AD reflects the diffusion along the principle eigenvector (AD =

λ_1), while radial diffusivity is a combination of the eigenvectors perpendicular to the principle direction (RD = $(\lambda_2 + \lambda_3)/2$). While MD, AD, and RD can give us valuable information, FA is a measure that combines the effects of all eigenvalues, calculated as:

$$Fractional\ Anisotropy\ (FA) = \sqrt{\frac{1}{2}}\sqrt{\frac{(\lambda_1 - \lambda_2)^2 + (\lambda_2 - \lambda_3)^2 + (\lambda_3 - \lambda_1)^2}{\left({\lambda_1}^2 + {\lambda_2}^2 + {\lambda_3}^2\right)}} \quad [3.7]$$

As such, FA values fall between 0 and 1. An FA of 0 would indicate perfect isotropic diffusion as the tensor ellipsoid would resemble a sphere, with equal diffusion occurring in all directions (i.e., $\lambda_1 = \lambda_2 = \lambda_3$). Conversely, an FA closer to 1 would indicate anisotropy, and the tensor ellipsoid would look like a stick rather than a sphere (Figure 3-4).

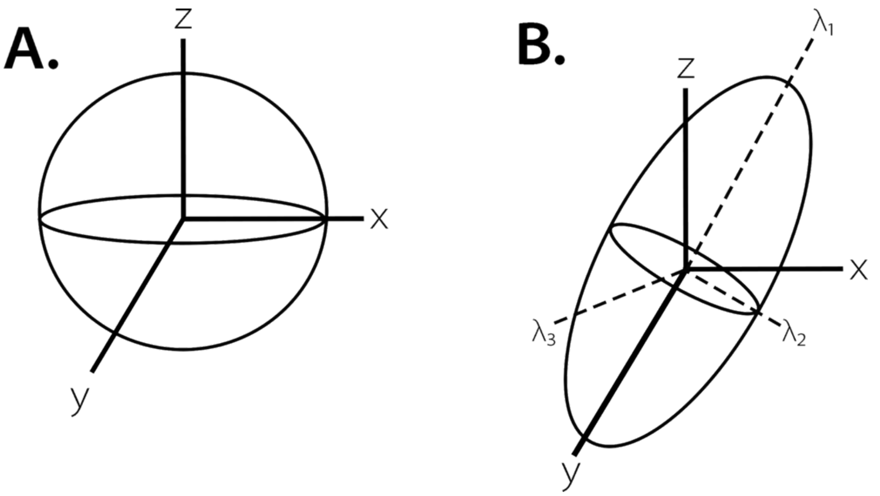

Figure 3-4: Diffusion sphere and ellipsoid. Representative tensors for (A.) isotropic, where diffusion is equal in all directions, and (B.) anisotropic environments, where diffusion is greatest along λ_1.

In the case of nerve degeneration in the upcoming chapters, we would expect healthy nerve to have a higher FA value than injured tissue, mostly due to the effects of reduced RD. Implications for this finding will be discussed further in Chapter 6 of this dissertation. In addition to the scalar indices, information from the principal eigenvector (ε1) can be used to infer the primary course of axons in tissue and reconstruct fiber tracts.

The measures we derive from DTI are sensitive to the pathological features in tissue. AD is sensitive to axonal integrity and can assess axonal degeneration[58,59]. RD is sensitive to myelin integrity and increases in cases where edema is present[60,61]. MD is sensitive to overall displacement of molecules and the presence of obstacles, and has proved useful in assessing ischemic stroke[62]. FA is sensitive to alterations in structure from disease and assesses both axonal and myelin changes in tissue[63].

While DTI methods relate to pathology by measuring the effect of tissue barriers (e.g., cell membranes) on water diffusion, there are some notable limitations of DTI. These include partial voluming, the "crossing fiber problem", and how measures are sensitive, but not specific, to certain pathologies. Partial voluming is a result of image resolution limitations inherent to MRI. Within the large imaging voxels (3-dimensional pixels) required for DTI, there are water protons with different diffusion properties; however, all of this information is typically averaged together within a single voxel. Another example of partial voluming is the crossing fiber problem, where two fiber populations may cross within a voxel, resulting in an inaccurate reflection of microstructure that may lead to misdiagnosis when traditional DTI methods are used. Additionally, DTI measurements have been shown to be sensitive, but not specific, to various pathologies. For example, conventional DTI methods using pulsed gradients are sensitive to cell death, edema, inflammation, demyelination, and partial volume effects, all of which can lead to similar apparent changes in fractional anisotropy (FA).

Advanced diffusion methods have been developed to overcome these limitations[64–66]. One such method is multi-dimensional diffusion encoding and the diffusion tensor distribution model proposed by Westin et al.[64], which offers the ability to discriminate between the sizes, shapes, and orientation of the diffusion microenvironment in living tissue. More specifically, this method uses a combination of spherical and linear tensor encoding techniques and specialized post-processing to derive values for macroscopic anisotropy, orientation coherence, size variance, and microscopic anisotropy (μFA). This method may be a useful application to the PNS as it is composed of nearly the same white matter microtissue, with the exception of higher amounts of collagen[4]. Microtissue refers to the characterization of groups of cells that function together within a very small space of tissue. For example, after a nerve injury occurs, collagen production greatly surpasses the ideal response to the severed nerve, which often hinders the growth of sprouting, innervating axons and can impact diffusion measurements such as FA[60]. For our purpose, this sequence and model may provide measurements that can differentiate between myelin and axonal pathologies after surgery and neuropathic degeneration, which may be more predictive of long-term outcomes than traditional DTI measures. Multidimensional diffusion will be discussed further in this dissertation, as it is the main topic of Chapter 5.

3.2.2 Basics of Magnetization Transfer

Magnetization Transfer (MT) Imaging is used to detect the exchange of magnetization between solid-like macromolecular populations of protons and surrounding water, and was employed herein because it has been shown to be sensitive to myelin content[67]. In typical MRI experiments, we measure signal from water protons within tissue. However, as we discussed in the previous section, there are also protons that are associated with large macromolecules (e.g., solid parts of tissue) that exchange information with nearby water through dipolar and chemical exchange mechanisms. In an MT experiment, the intention is to saturate the macromolecular pool and transfer this saturation to the observed water pool to get indirect information on the macromolecular pool[68]. Note that while these macromolecules also affect relaxation rates and can impede the free diffusion of water, MT is thought to be a more specific assay of macromolecular content and exchange.

In the macromolecular pool, the immobile protons have a very short T_2 (<<1 ms) that results in a broad saturation lineshape. Mobile protons in the water pool tend to have a longer T_2 that results in a much narrower lineshape. In MT, we can exploit these different lineshapes and selectively saturate the broad macromolecular pool by applying an RF pulse that is off-resonance relative to water (in the 1 - 2 kHz range). In the ideal case, this will partially saturate the macromolecular protons without affecting the water protons, as shown in Figure 3-5. Since there is coupling between the two pools; the selective saturation of the macromolecular pool exchanges with water and results in a decreased free-water signal which can be measured.

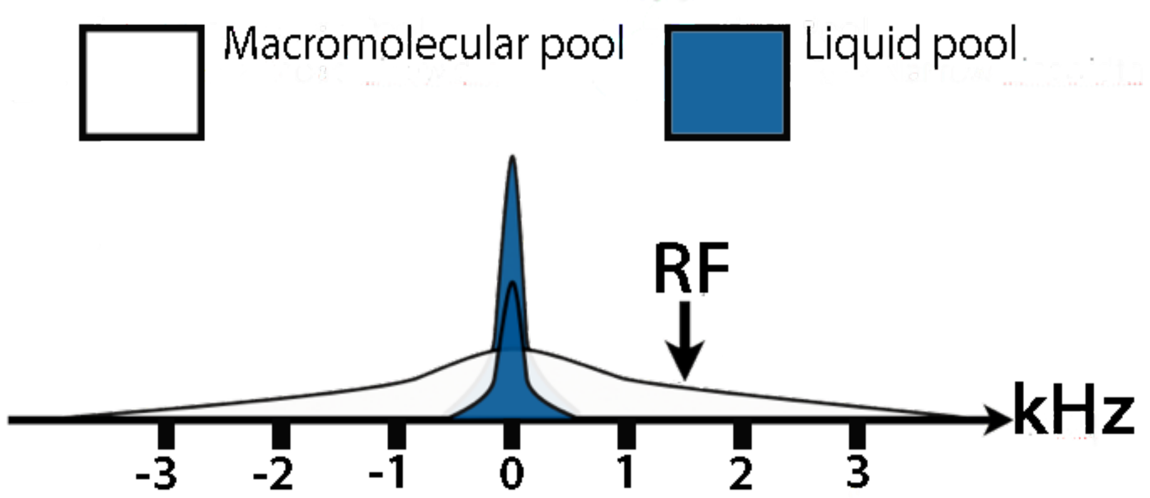

Figure 3-5: MT pulse saturation. Macromolecular (white) and liquid (blue) pool frequency linewidths in MT acquisition. Application of RF pulse at a specific Hertz (shown at 1.5 kHz) allows for saturation of the macromolecular pool. Large liquid pool in background represents liquid pool before saturation, while small liquid pool shows after saturation.

The Magnetization Transfer Ratio (MTR) is a common measurement of this phenomenon, and has been used as a measure which assesses myelin content in disease[69]. To measure MTR, imaging volumes are acquired with and without application of an MT saturation pulse. The signal with the MT-pulse (S_{MT}) and its reference without an MT-pulse (S_{REF}) are used to calculate MTR as shown:

$$MTR = (1 - S_{MT} / S_{REF}) \times 100\ (\%) \qquad [3.8]$$

MT pulse sequences have evolved over time to improve performance and scan time for patient applications. Continuous Wave MT pulse sequences were first developed, in which a constant RF pulse was applied for approximately a second before employing the imaging sequence. Because most clinical RF amplifiers on imaging systems were not designed to run in continuous wave mode, these constant RF pulses are often replaced with a train of shaped pulses followed by a readout. However, this results in long scans that are not clinically viable. As a result, pulsed saturation methods which perform the imaging sequence between each saturation pulse (rather than at the end of the MT sequence) are commonly used[70]. For our work in peripheral nerves, pulsed saturation was combined with a multi-shot EPI readout to reduce scan times and a water-selective excitation pulse (as described below in Section 3.2.3) to minimize the impact of fat as shown in Figure 3-6.

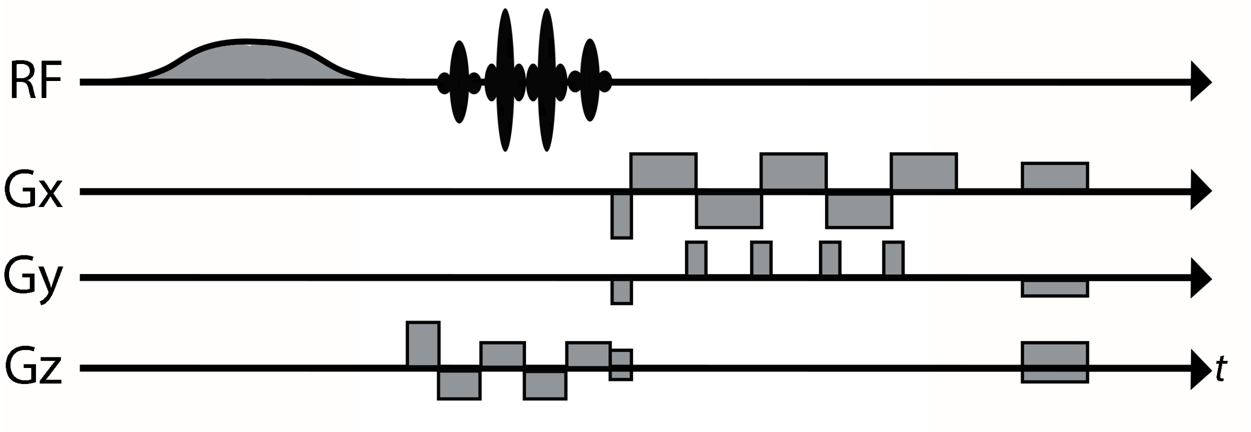

Figure 3-6: MT pulse sequence. *RF* for radiofrequency pulse, *Gx* for gradient in x-direction, *Gy* for gradient in y-direction, *Gz* for gradient in z-direction, *t* for time. At the beginning of the RF line, a Gaussian-shaped pulse represents the saturation pulse for MT. The RF pulses that follow are water-selective and designed to eliminate fat signal. An EPI readout was used to collect five lines of k-space per TR. The last set of gradients in G_{xyz} are spoiler gradients.

The magnitude of water signal attenuation (i.e., size of the MT effect) depends primarily on the size of the macromolecular pools, although MTR is also sensitive to the rate of MT between pools and T_1. In the case of unhealthy or demyelinated nerve, we would expect MTR values to be lower than healthy nerve due to a reduction in macromolecular content following demyelination.

A limitation of this technique is that the measurements can be sensitive to RF or B_1 effects, especially in outside the head (e.g., skeletal muscle in thigh), which can lead to bias in MTR values. Since this bias can be measured and occurs in an approximately linear fashion, B_1 can be measured in the same volume as the MTR data to calculate a correction for this bias[71]. In cases of neuropathy, teasing apart axonal loss from demyelination by MTR is difficult because both results in a reduction in total myelin content. In this case, a multi-parametric approach that also includes DTI might be beneficial. In addition, MTR is also sensitive to acquisition parameters and T_1, which can make comparisons across sites and field strengths difficult. Quantitative Magnetization Transfer (qMT) has been developed to alleviate these issues, whereby a series of MT-weighted images are acquired over a range of RF frequencies and power, and these data are fit with a model to extract more quantitative information (e.g., the relative size of the macromolecular pool). Although qMT has also been applied outside of the brain[72], it requires long scan times that often, but not always, limit clinical use. As a result, MTR was chosen in this project for its biological relevance and quick imaging speed.

3.2.3 Basics of Dixon Fat-Water Imaging

In in vivo MR experiments, the acquired images will often contain contributions from fat, which has its own unique signal characteristics. Since water is the primary signal of interest, the contribution of fat signals may result in unwanted artifacts that will have subsequent impacts on quantification. In these cases, fat suppression techniques are required to eliminate the unwanted fat signal. However, there are circumstances where detection of the fat signal is important to understanding disease in a patient population and could be a valuable tool for clinicians and physicians. Prospective fat suppression techniques remove the fat signal from tissue before measurements are taken, while retrospective techniques remove the signal of fat during post-processing of the acquired data. These strategies are a useful application in studying peripheral nerves as they are often surrounded by fat. This is especially useful to eliminate unwanted chemical shift artifacts in diffusion EPI sequences that can obfuscate measurements.

Common fat suppression techniques include water-selective excitation pulses (shown in Figure 3-6), gradient reversal fat suppression, Short-T_1 Inversion Recovery (STIR), and SPectral Attenuated Inversion Recovery (SPAIR) prepulses. Gradient reversal fat suppression reverses the polarity of the slice selection gradient for the refocusing relative to the excitation pulse, which results in slices that are shifted in opposite directions during excitation and refocusing for fat and a reduced fat signal[73]. STIR is accomplished by inverting the longitudinal magnetization of both water and fat protons and choosing an inversion time that nulls any material with a short T_1, including fat. SPAIR is similar to STIR, except that SPAIR is accomplished by using an adiabatic inversion pulse to on the fat resonance to selectively invert fat protons only, which results in less attenuation of the water signal than STIR at the expense of increased sensitivity to B_0 variations[74].

Rather than prospectively remove the fat signal before measuring, Dixon methods encode the chemical shift difference between fat and water protons during data acquisition, and then uses a post-processing algorithm to retrospectively separate each signal into independent fat and water signal maps of tissue[75]. In the original “two-point” method, two different echo times were acquired to create an image with water and fat signals in-phase and the other image with water and fat signals out-of-phase. Denoting in-phase image (IP), out-of-phase image (OP), fat signal (F), and water signal (W), these maps can be calculated with the following formulae:

$$IP = W + F \qquad [3.9]$$

$$OP = W - F$$

$$Fat\ only\ image = \frac{1}{2}(IP - OP)$$

$$Water\ only\ image = \frac{1}{2}(IP + OP)$$

This two point method, however, does not account for phase errors due to, for example, B_0 variations and T_2*. To account for these phase errors, a three point Dixon method was developed. By obtaining an additional measurement that accounts for field inhomogeneity-related phase error, it has been shown the precision and accuracy of the estimated fat and water signals can be improved.

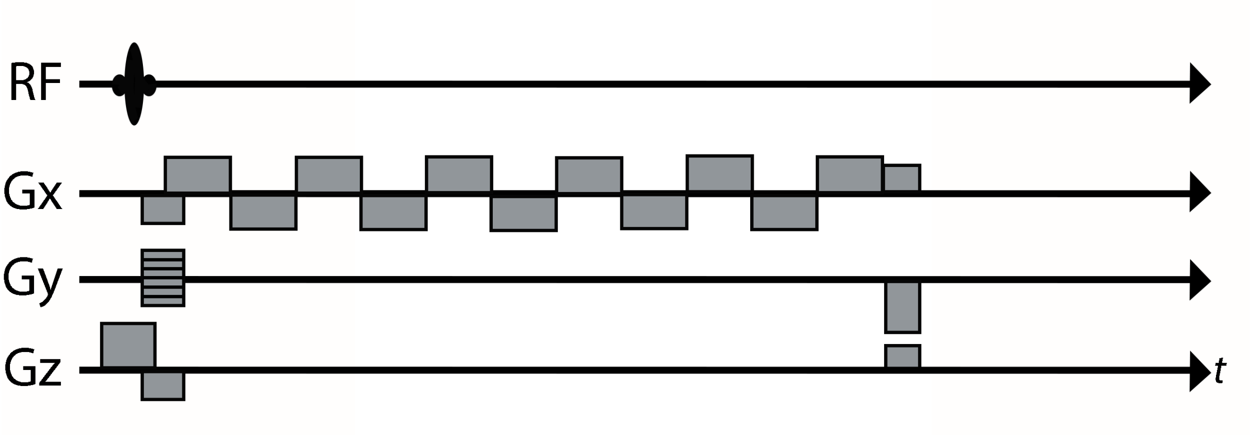

Figure 3-7: 6-Point Dixon pulse sequence. *RF* for radiofrequency pulse, *Gx* for gradient in x-direction, *Gy* for gradient in y-direction, *Gz* for gradient in z-direction, *t* for time.

Since the introduction of this method, modern developments have included improved phase correction (through acquisition, post-processing, or both) to remove B_0 inhomogeneity, multi-peak models to account for the fact that fat does not contain a single resonance, and methods that estimate T_2*. One such "six point" Dixon method (Figure 3-7) was applied herein to skeletal muscle in the lower extremity. The six point method acquires additional images to ensure accurate calculations for resulting fat and water maps, while also simultaneously accounting for T_2* effects.

The Dixon technique is helpful for studying neuropathy as axonal loss can lead to the target skeletal muscle becoming denervated and muscle wasting occurs. Since fat replacement follow muscle atrophy, there is an expectation that the percentage of fat in muscle can be used as a viable marker for disease and possibly progression of motor deficits. Dixon has been applied to many neuromuscular diseases in order to establish the method as a biomarker for disease, monitoring chronic inflammatory demyelinating polyneuropathy, diabetes, and muscular dystrophy[76–80]. For the scope of this project, the relative signal of the fat and water only images provided by the Dixon technique will be used to quantify inter-muscular fat percentage in the inherited neuropathy cohort. These measures will provide critical information to the degree of primary muscle atrophy and secondary axonal loss across two stations in the leg (proximal thigh and distal ankle) to assess length-dependent changes along the sciatic and tibial nerves of the leg.

Together, these three quantitative MRI techniques can provide clinicians and researchers with tools that can assess tissue microstructure in peripheral nerves. These procedures are non-invasive and can provide information that is difficult to acquire by current clinical assessment, such as in distal degenerating nerves in cases of trauma and disease. While this chapter serves as an overview of the DTI, MT, and Dixon imaging, specific applications of these techniques to the peripheral nervous system will be discussed in the following chapter.

CHAPTER IV

APPLICATIONS OF MRI TO PERIPHERAL NERVES

4.1 DTI MRI Applied to Peripheral Nerves

Application of DTI to peripheral nerves was first investigated in animal studies. Beaulieu et al. measured diffusion in crushed (self-resolving, regenerating) and cut (non-regenerating) injuries in frog sciatic nerve 4 weeks after injury. Results showed decreased anisotropic diffusion, with smaller changes in crushed/regenerating nerve[81]. In a crush and cut nerve injury rat model, Stanisz et al. measured FA in nerve that was proximal and distal to injury, finding that crushed nerves distal to injury recovered to healthy FA values, while cut nerves with no surgical repair did not recover[82]. Additionally, a study utilizing diffusion tensor fibertracking monitored injury and recovery post-injury and at three weeks post-injury. Results showed fibertracking continuity improved at three weeks after injury from post-injury, and that FA correlated with motor and sensory functional recovery[83]. Ex vivo results agree with these findings, showing lower FA in cut than crushed nerves and the use of tractography to assess nerve continuity[84]. Recent studies have shown DTI may predict failed repairs and identify cases that require re-operation[85]. The chorus of these studies demonstrate that there is a relationship between DTI and underlying pathology in animal models of nerve injury.

Early development of diffusion MRI in the human PNS started in the early 1990’s with Howe et al. showing the first known application to imaging the human nerves, calling the method “neurography”. However, in this experiment, diffusion was used to enhance contrast of the nerves rather than to estimate nerve integrity[86]. A few years later in 1996, Filler et al. showed that MR neurography can identify nerve discontinuity in severe trauma and localize nerve compressions prior to surgical examination[87]. Nearly a decade later after Basser's establishment of DTI, Hiltunen et al. showed in six subjects that DTI and nerve fiber tractography were feasible in the distal peripheral nerves at 3-Tesla. Another important piece of this study was that it supplied normative DTI values for the median, ulnar, radial nerves of the upper extremity and the tibial and peroneal nerves of the lower extremity[88]. Kabakci et al. continued this work in 2007 establishing normative values of FA (0.71 ± 0.05) and ADC (1.02 ± 0.13) for healthy median nerve and finding significant variations along the length of the nerve[89]. Additionally, Andreisek[90] assessed and established the optimal b-value for DTI and fiber tractography of the median nerve at 1.5 T to be approximately 1000 s/mm^2.

Further optimizations of DTI to human peripheral nerves are greatly contributed to Guggenberger and Zhou. In 2012, Zhou et al. developed a protocol for DTI of the whole forearm[91], and this acted as a pre-cursor to the next study in 2013, which optimized resolution and number of diffusion directions[92]. Around the same time, Guggenberger assessed DTI of the median nerve by intra- and inter-reader agreement and concluded and user- and software-dependent factors contribute little variance in calculating DTI measurements in peripheral nerve[93]. In the same year, Guggenberger would further refine the parameters for DTI fiber tracking in nerves[94]. Finally, Guggenberger showed that FA and ADC values of the median nerve were repeatable enough across scanners for larger group studies or in cases where substantial diffusion changes would be expected[95]. Another important development can be attributed to Heckel et al., who demonstrated the DTI indices in healthy nerve correlate with electrophysiology, paving the way for future clinical applications[96]. Together, these findings indicate that DTI is a viable tool that can i.) differentiate healthy and injured nerve pathology, ii.) assess nerve integrity, and iii.) relate to current clinical measures.

4.2 Magnetization Transfer MRI Applied to Peripheral Nerves

Applications of MTR to peripheral nerves also had its beginnings in animal studies. In 1995, Does et al. demonstrated in vivo frog sciatic nerve T_2 relaxation components for myelin (19ms, 26%), axon (63 ms, 29%), and connective tissue (241 ms, 45%)[97]. Later in 1998, Does et al. showed that each T_2 component of frog sciatic nerve had respective T_1 and MTR values, yet MTR values were similar across myelin water and intra/extracellular water in the nerve[98]. A study by Stanisz et al. from 2001 measured cut and crushed rat sciatic nerves with MT to look at proximal- and distal-to-injury changes after trauma[82]. Stanisz found that i.) MT of healthy nerves and proximal portions of the injured nerve had similar MT, ii.) distal portions of crushed nerve had a reduced MT, and iii.) distal portions of cut nerve had an even lower MT. These results correlated with tissue microstructural changes and were consistent when compared to histology. Further, they concluded that MT showed the largest difference in cut nerves, and it may serve as an indicator of regeneration. In 2005, Odrobina et al. showed in the sciatic nerve of rats that MR properties of excised neural tissue following experimentally-induced demyelination differed greatly from healthy myelinated tissue, concluding that MTR was a function of myelin[99]. Recent work using qMT on mice sciatic nerve showed significant differences in the pool-size ratio, reflecting underlying tomacula in HNPP and reduced myelination in CMT1A respectively[100].

Recent human applications showing the clinical importance of employing MTR have been shown by Dortch et al., where MTR values were significantly decreased in patients with CMT compared to controls and related to disability score[101]. In 2016, Morrow et al. showed that MTR could reveal early changes in muscles before significant intramuscular fat accumulation, and concluded that MTR may provide a measure of early disease before irreversible changes have occurred[76]. However, some have criticized MTR, claiming the measure may be influenced by other exchange processes such as edema and inflammation and may not be a direct measure of myelination[102]. As a result, MTR is often employed in a multi-parametric approach, where other measures may corroborate the findings from MTR and/or provide complementary information.

4.3 Dixon MRI Applied to Peripheral Nerves

Dixon MRI has shown useful in detecting downstream changes in skeletal muscles cases of inherited peripheral nerve neuropathy and neuromuscular disorders. These effects can be quantified by MRI, since the displacement of intramuscular water is followed by intramuscular fat innervation. Morrow et al. used Dixon imaging, specifically the fat only image (i.e., Fat Separation Fraction = F/(W+F); F = fat only image; W = water only image) longitudinally over a year in patients with CMT1A and Inclusion Body Myositis (IBM)[76]. Each subject had two scans, one baseline, and another one year later to assess disease progression. MRI measures were obtained in the thigh and calf to assess length-dependent changes along the course of the sciatic and tibial nerves. Results of CMT1A patients showed fat fraction increased at the one year follow-up scan in calf, but not in thigh. For IBM patients, they found that fat fraction from baseline to one year increased significantly in both the thigh and the calf. In addition, fat fraction measures correlated to the lower limb components of the Charcot-Marie-Tooth examination score and the IBM functional rating score. Conclusions from this study are that Dixon Fat-Water imaging can sensitively monitor fat accumulation across multiple cohorts and relate to current clinical measures of the respective disease/disorder. Similar findings for CMT have been reported in other studies, and others have used this method to probe in influence of fat in non-systemic vasculitic neuropathy[103,104]. It is worth noting for interpretation that fat accumulation is one of the later pathological changes that occurs, and so fat fraction measures may reflect an indirect measure of axonal loss. Aside from quantifying fat, Dixon techniques have also been utilized to suppress the fat signal in the optic nerve and diabetic neuropathy[105,106].

4.4 Challenges of Applying These Methods in Human Peripheral Nerves

Implementing these method in the human peripheral nervous system has numerous challenges. First, there is a competing need for high-resolution of images and scan time. For example, the sciatic nerve is 5 mm in diameter, making it a much smaller structure than typically imaged for neurological applications. To solve this in the studies detailed in the following chapters, high in-plane resolution images were typically acquired with thicker slices along the nerve to increase the signal-to-noise ratio (SNR). Second, the T_2 of nerve (around 40 ms) is much shorter than white matter in the brain; therefore, sequences were optimized to minimize TE when possible (e.g., lower b-value diffusion gradients were chosen for our DTI studies relative to studies optimized for the brain). Last, as previously mentioned, the influence of fat in peripheral nerve imaging is an important limitation to overcome to provide adequate measurements and reduce imaging artifacts. To accomplish this, various fat suppression were employed as described in Chapter 3 to ensure the estimated parameters were not influenced by fat surrounding the nerves.

CHAPTER V

LENGTH-DEPENDENT MRI OF HEREDITARY NEUROPATHY WITH LIABILITIES TO PRESSURE PALSIES

5.1 Summary

Hereditary neuropathy with liability to pressure palsies (HNPP) is caused by heterozygous deletion of the peripheral myelin protein 22 (*PMP22*) gene. Patients with HNPP present multifocal, reversible sensory/motor deficits due to increased susceptibility to mechanical pressure. Additionally, age-dependent axonal degeneration is reported. We hypothesize that length-dependent axonal loss can be revealed by MRI, irrespective of the multifocal phenotype in HNPP. Nerve and muscle MRI data were acquired in the proximal and distal leg of patients with HNPP ($n = 10$) and matched controls ($n = 7$). More specifically, nerve magnetization transfer ratios (MTR) were evaluated to assay proximal-to-distal gradients in nerve degeneration, while intramuscular fat percentages (F_{per}) were evaluated to assay muscle fat replacement following denervation. Neurological disabilities were assessed via the Charcot-Marie-Tooth neuropathy score (CMTNS) for correlation with MRI. F_{per} values were elevated in HNPP proximal muscle (9.8 ± 2.2%, $p = 0.01$) compared to controls (6.9 ± 1.0%). We observed this same elevation of HNPP distal muscles (10.5 ± 2.5%, $p < 0.01$) relative to controls (6.3 ± 1.1%). Additionally, the amplitude of the proximal-to-distal gradient in F_{per} was more significant in HNPP patients than controls ($P < 0.01$), suggesting length-dependent axonal loss. In contrast, nerve MTR values were similar between HNPP subjects (sciatic/tibial nerves = 39.4 ± 2.0/34.2 ± 2.5%) and controls (sciatic/tibial nerves = 37.6 ± 3.8/35.5 ± 1.2%). Proximal muscle F_{per} values were related to CMTNS ($r = 0.69$, $p = 0.03$), while distal muscle F_{per} and sciatic/tibial nerve MTR values were not related to disability. Despite the multifocal nature of the HNPP phenotype, muscle F_{per} measurements relate to disability and exhibit a proximal-to-distal gradient consistent with length-dependent axonal loss, suggesting that F_{per} may be a viable biomarker of disease progression in HNPP.

5.2 Introduction

Hereditary neuropathy with liability to pressure palsies (HNPP) is a dysmyelinating polyneuropathy caused by heterozygous deletion of the peripheral myelin protein 22 (*PMP22*) gene[107]. The clinical presentation consists of reversible, focal numbness, and weakness that may or may not be triggered by mechanical compression or repetitive limb movements. Pathological studies reveal "tomacula" (excessively folded myelin in paranodes)[108] and length-dependent axonal loss, the latter of which develops during aging[109]. Previous studies indicate that axonal loss, not demyelination, is correlated with disability in other inherited neuropathies, such as CMT1A[110]. However, it is still unclear if accumulative axonal loss in HNPP is correlated with disabilities due to the transient and multifocal nature of the disease phenotype.

Although tools are available to assess HNPP (e.g. nerve conduction studies [NCS], skin biopsies, and Charcot-Marie-Tooth neuropathy score [CMTNS][111]), they primarily target distal nerves, which may be degenerated in some patients, resulting in "floor effects."[112] Consistent with magnetic resonance imaging (MRI) studies in the brain[102,113,114], we demonstrated[101] that nerve magnetization transfer ratio (MTR) MRI can overcome these limitations and provide sensitive measures to myelin content changes from de/dysmyelination and axonal loss. Others have demonstrated that fat-water MRI of skeletal muscle assays atrophy and fat replacement in neuromuscular diseases[71,76,115,116], which indirectly reflects axonal degeneration.

The present study evaluated these nerve MTR and muscle fat-water protocols in patients with HNPP. Given that axonal loss may accumulate over time, we hypothesize that nerve/muscle MRI can reveal axonal degeneration in HNPP, thereby serving as a noninvasive, objective measure related to disease severity. Both the proximal and distal leg were scanned to assess length-dependence. Our results show a correlation between certain MRI findings and disability.

5.3 Methods

Human subjects and clinical information

Ten patients (100% female, age: 47.1 ± 12.5 years; body mass index, BMI: 29.3 ± 4.3) with genetic confirmation of a *PMP22* heterozygous deletion were recruited from the CMT clinic at the Vanderbilt University Medical Center, which is a part of the Inherited Neuropathy consortium. Seven healthy volunteers (100% female, age: 54.4 ± 3.5 years, BMI: 26.1 ± 6.3) were enrolled as controls by matching for mean age, gender, and BMI (see Table 5-1).

Clinical disability was assessed via the CMTNS version 2 in all patients. The CMTNS is an ensemble of sensory symptoms, muscle strength, as well as physical findings, with higher scores indicating more impairment (range: 0 - 36). All HNPP subjects also underwent NCS using conventional methods[117] (see Table 5-2). In the control group, subjects self-reported no symptoms that were suggestive of peripheral nerve diseases and physical examination indicated no evidence of peripheral neuropathies. Due to well-established normative values in normal controls, it is standard practice that NCS data from patients are evaluated by comparison to these normative values[118]. As a result, NCS data were not obtained in the control cohort, which did not allow for a correlation of MRI data and clinical findings in this cohort.

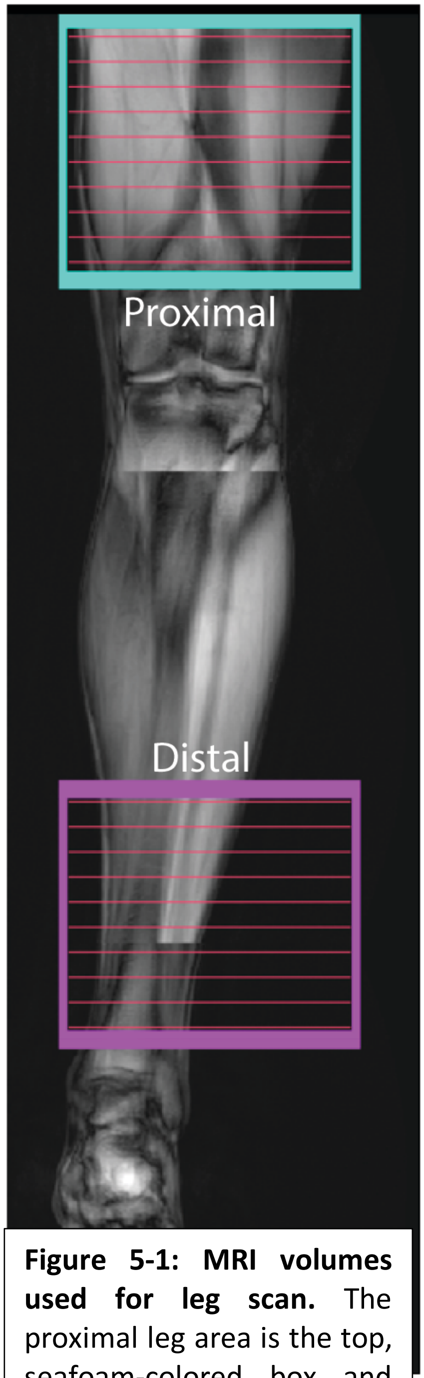

Figure 5-1: MRI volumes used for leg scan. The proximal leg area is the top, seafoam-colored box and the distal leg area is the bottom, magenta-colored box. Red lines inside indicate slice selection.

MRI data acquisition

Participants were examined via MRI, lying feet-first and supine in a Philips 3.0-T Acheiva MRI scanner (Philips Healthcare, Best, The Netherlands), with R5.3 software. A Philips dStream 16-channel anterior coil was used for full coverage of the lower extremities. The multi-parametric imaging protocol included nerve MTR and muscle fat-water MRI scans, which were used to estimate nerve MTR and intramuscular fat percentage (F_{per}), respectively. Two volumes were acquired in each subject as shown in Figure 5-1. The first volume was acquired proximal to the knee to estimate proximal muscle F_{per} and sciatic nerve MTR values. The second volume was acquired distal to the knee to estimate distal muscle F_{per} and tibial nerve MTR values.

MTR data were acquired via a 3D, multi-shot EPI of an MT-prepulse (1000° nominal flip angle, 1.5 kHz off-resonance) and the following: resolution = $0.8 \times 0.8 \times 6$ mm^3, TR/TE = 60/11 ms, water-selective excitation pulse (10°), k-space lines per shot = 5, SENSE factor = 1, NEX = 2, and a total scan time of ≈6 min. The RF transmit field (B_1) was estimated using the actual flip-angle imaging approach to correct MTR values for B_1 variations. Fat-water data were acquired via a six-echo gradient echo sequence: resolution = 0.75 x 0.75 x 3 mm^3, TR/first TE/echo spacing = 300/13/17 ms, and a total scan time of ≈2 min.

MRI data analysis

B_1-corrected MTR maps were estimated using our previously published method[101], and mean slice-wise MTR values were calculated for sciatic/tibial nerves. Recall MTR is calculated as follows:

$$\mathrm{MTR} = (1 - S_{MT} / S_{REF}) \times 100\,\%, \tag{5.1}$$

where S_{MT} represents the signal intensities of the MT-weighted volume and S_{REF} represents the signal intensities in the reference (no MT-weighting) volume. For MTR measurements, slice-wise regions-of-interest (ROIs) were manually selected for the sciatic (proximal volumes) and tibial nerves (distal volume) using in-house written software in MATLAB (Mathworks, Natick, MA, version 2017a)[119,120]. These ROIs were then multiplied by a mask from MIPAV's (NIH, Bethesda, MD) fuzzy C-means segmentation algorithm, which eliminated background voxels as well as voxels that had been partially volume averaged with fat, and mean slice-wise MTR values were estimated.

The ratio of the fat-to-water signal, or fat percentage (F_{per}), was estimated from the multi-echo gradient data via the optimized tools within the ISMRM Fat-Water Toolbox[121]. From these maps, the entire muscle volume was segmented from surrounding fat and the median F_{per} was tabulated to ensure that the reported value was indicative of intramuscular fat replacement.

Statistical analysis

All statistical analyses were conducted using MATLAB. Tests were performed to evaluate (i.) differences between patients and controls for each MRI measure, (ii.) within-cohort differences between scanning locations (proximal vs. distal) for each MRI measure, (iii.) across-cohort differences in the strength of the effect of scanning locations (distal minus proximal) for each MRI measure (i.e. tests for whether length-dependent effects were more significant in patients), and (iv.) the relationship between MRI measures and clinical disability score (CMTNS) in patients. Nonparametric statistical approaches were primarily employed for analysis due to the small sample size of the study. Given the exploratory nature of this study, we did not correct for multiple comparisons and deemed a threshold of $p < 0.05$ as indicative of relationships that warrant further investigation.

Four MRI parameters were included in these analyses: sciatic nerve MTR, tibial nerve MTR, proximal muscle F_{per}, and distal muscle F_{per}. We first tested for differences in each MRI parameters across cohorts with a Wilcoxon rank sum test. In addition, Wilcoxon signed rank tests were employed within each cohort to test for length-dependent differences in each MRI parameter per subject (proximal and distal leg measurements). The difference between proximal and distal measures was then estimated for each subject and MRI measure, and linear regression analyses were performed across cohorts to test for significant inter-cohort differences in these length-dependent effects. Finally, associations between MRI parameters and CMTNS were tested via Spearman’s rank correlations.

Although we attempted to match our control and HNPP cohorts for age and BMI, subtle differences between cohorts may influence findings. As a result, we tested for (i.) differences in age and BMI across cohorts using a Wilcoxon rank sum test and (ii.) associations between the

MRI parameters and both age and BMI in our control cohort using Spearman's rank correlations. In addition, NCS values in patients with HNPP were compared to normative values using a Wilcoxon signed rank test.

5.4 Results

Clinical features of patients

Significant differences for age (*p* = 0.10) and BMI (*p* = 0.19) were not detected across the control and HNPP cohorts. In addition, significant relationships were not observed between BMI (p > 0.12) and age (p > 0.43) and any of the reported MRI parameters.

	***Controls** (n = 7)*	***HNPP** (n = 10)*	***p-value***
Age (years)	54.4 ± 3.5 (50-59)	47.1 ± 12.51 (18-63)	0.10
BMI (kg/m^2)	26.1 ± 6.3 (16.95-37.67)	29.3 ± 4.3 (19.79-34.45)	0.19
Female (%)	100	100	-
MTR – sciatic (%)	39.4 ± 2.0 (35.89-41.34)	37.6 ± 3.8 (34.27-45.94)	0.16
MTR – tibial (%)	34.2 ± 2.5 (30.44-36.75)	35.5 ± 1.2 (33.50-37.38)	0.47
Intramuscular Fat – proximal (%)	6.9 ± 1.0 (4.89-7.69)	9.8 ± 2.2 (6.71-13.72)	0.01 *
Intramuscular Fat – distal (%)	6.3 ± 1.1 (5.17-8.09)	10.5 ± 2.5 (6.94-15.14)	< 0.001 *

Table 5-1: Summary demographic and MRI data. Data collected in all subjects within each cohort and presented as mean ± standard deviation (range). P-values from Wilcoxon Rank Sum analyses are presented, with an asterisk indicating significance.

	n	*Mean ± SD*	*Range*	*Norm*[a]	*p-value*
CMTNS	10	6.6 ± 3.1	2.0-12.0	-	-
MCV (m/s)					
Median	10	49.30 ± 4.30	44.0-58.0	49	0.91
Ulnar - proximal	10	48.70 ± 5.85	41.0-57.0	49	0.79
Ulnar - distal	8	44.88 ± 10.15	24.0-55.0	-	-
Peroneal - proximal	7	37.29 ± 3.04	32.0-41.0	44	0.02 *
Peroneal - distal	7	45.43 ± 8.56	36.0-61.0	-	-
DML (ms)					
Median	10	5.59 ± 1.04	3.9-7.0	4.4	0.01 *
Ulnar	10	3.64 ± 0.83	2.9-5.8	3.3	0.28
Peroneal	7	7.21 ± 1.64	5.3-9.7	6.5	0.30
Tibial	9	6.34 ± 2.27	4.6-12.1	-	-
CMAP (mV)					
Median	10	8.50 ± 2.73	3.9-12.0	4	0.004 *
Ulnar	10	11.77 ± 7.27	5.2-31.0	6	0.004 *
Peroneal	7	2.76 ± 1.16	1.0-4.8	2	0.11
Tibial	9	5.12 ± 3.77	0.8-10.7	-	-
SPL (ms)					
Median	9	4.56 ± 1.08	3.2-6.7	3.5	0.02 *
Ulnar	10	3.66 ± 0.57	2.8-4.6	3.5	0.45
Radial	7	2.77 ± 0.27	2.4-3.1	-	-
Sural	5	4.60 ± 0.31	4.2-5.0	4.4	0.31
SNAP (mV)					
Median	9	13.90 ± 7.55	1.1-22.7	22	0.02 *
Ulnar	10	15.04 ± 7.90	5.8-34.4	10	0.04 *
Radial	7	25.84 ± 13.72	11.0-52.0	-	-
Sural	5	5.84 ± 2.18	3.2-9.2	6	0.88

Table 5-2: Electrophysiologic findings of HNPP subjects. P-values from Wilcoxon Signed Rank analyses are presented, with an asterisk indicating significance.

[a]Normative values from Hu et al. 2016[122]. Distal latency numbers listed are the upper limit of normal. Amplitude and conduction velocity numbers are listed in the lower limit of normal. Ulnar and Peroneal MCV reported contains both proximal and distal measures.

All patients with HNPP reported 1–3 incidents of reversible focal sensory loss and weakness throughout their life, which may or may not be triggered by mechanical compression. Results of NCS show focally slowed nerve conduction at the sites susceptible to mechanical pressure. For instance, eight out of 10 patients had a significantly prolonged distal latency of the median motor nerve across the wrist (average value in Table 5-2 = 5.59 ± 1.04 ms), but only two out of 10 patients had a mildly prolonged distal latency of ulnar motor nerve across the wrist (average value in Table 5-2 = 3.64 ± 0.83). A similar difference was observed between peroneal and tibial motor nerves. In addition, a focal slowing of conduction velocities was observed in the (i.) ulnar motor nerves across the elbow in two patients and (ii.) peroneal motor nerve across the fibular head in the other two patients. All these features suggest a representative population typical of the HNPP phenotype[122,123].

In addition, only one patient had a reduced amplitude of sensory nerve action potential (SNAP) in the ulnar nerves, but sural nerves in all patients were either nonresponsive or had a reduced amplitude of SNAP.

Muscle F_{per} values are elevated in HNPP

Figure 5-2 shows sample MRI findings in the proximal and distal leg, respectively, and these results are further quantified for each cohort in Figure 5-3 and Table 5-1. As shown in the zoomed insets, the sciatic and tibial nerves can be readily distinguished from surrounding fat (appears

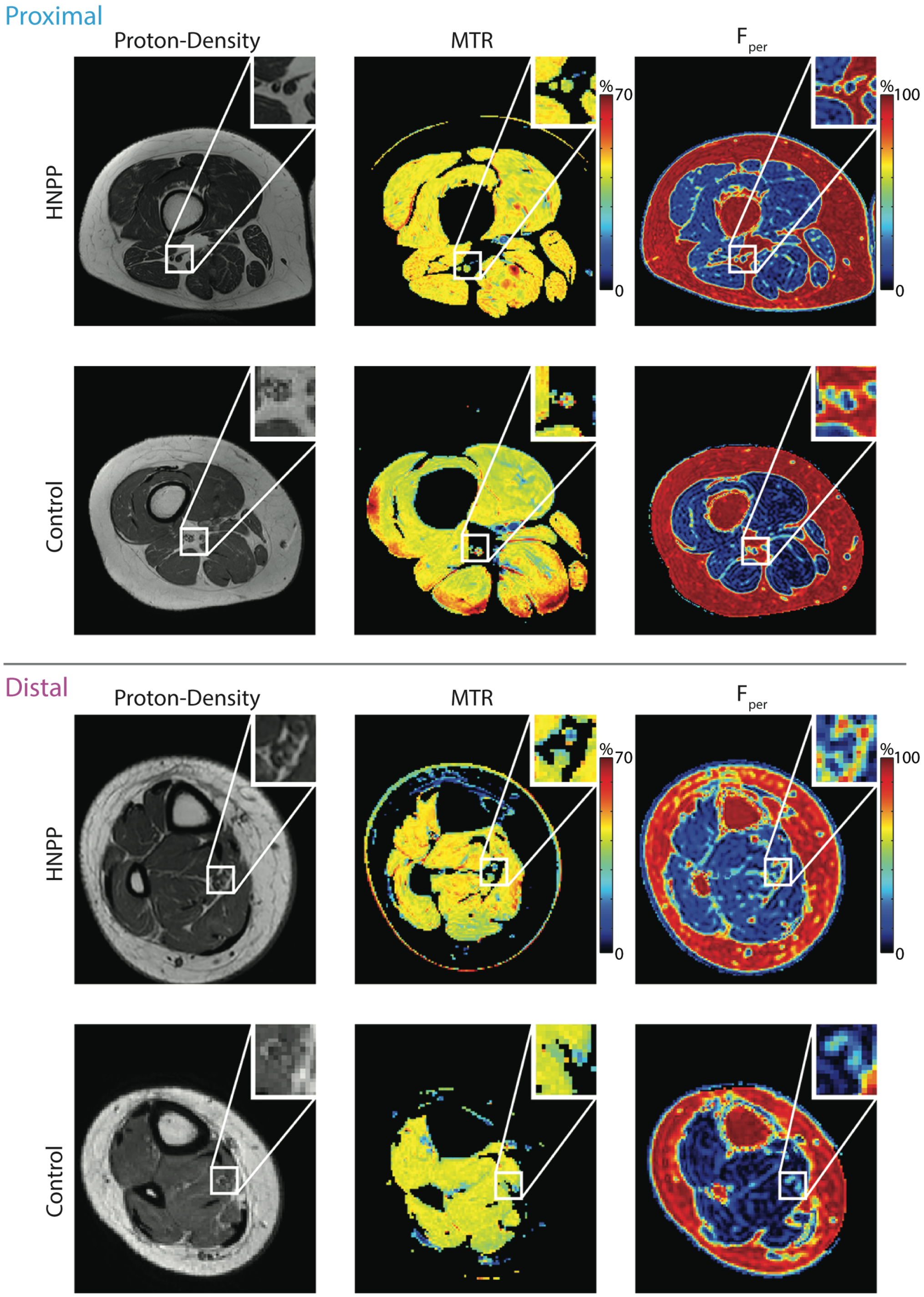

Figure 5-2: MRI findings. Proximal: Sample results of proton density (left), MTR (middle), and fat-water (right) imaging in proximal leg (thigh) for a representative HNPP patient (top row) and control subject (bottom row). Each imaging result includes a zoomed-in detail (top-right) showing the location of the sciatic nerve. Distal: Sample results of proton density (left), MTR (middle), and fat-water (right) imaging in distal leg (ankle) for a representative HNPP patient (top row) and control subject (bottom row). Each imaging result includes a zoomed-in detail (top-right) showing the location of the tibial nerve.

bright in the proton density images), muscle, and blood vessels in all slices. Across cohorts, F_{per} values in patients with HNPP were significantly elevated in proximal (*p* = 0.01) and distal muscles (p < 0.01) relative to controls (Figure 5-2). In contrast, MTR values were similar across cohorts in both the sciatic nerve (*p* = 0.16) and tibial nerve (*p* = 0.47).

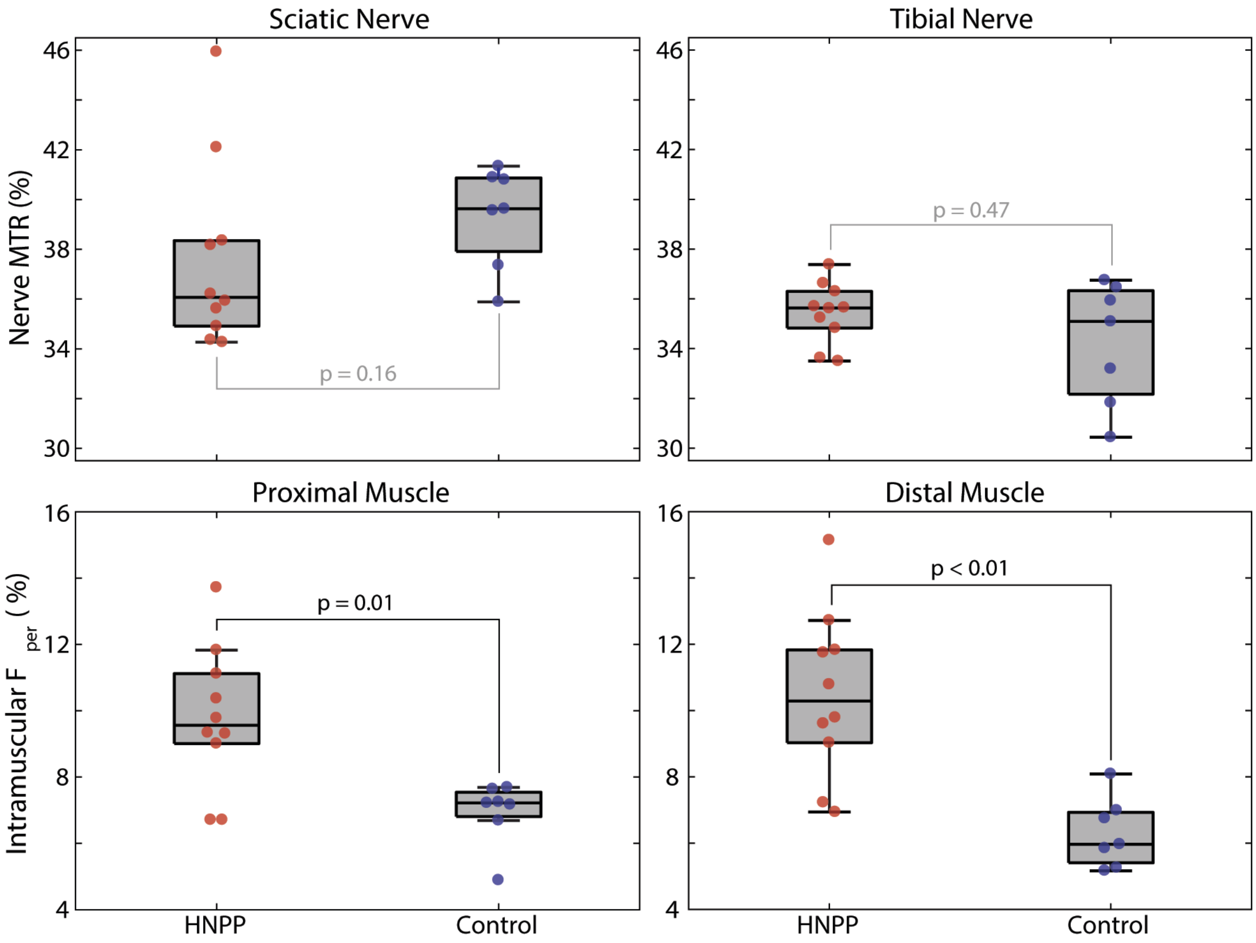

Figure 5-3: Differences between groups per MRI measure. Sciatic/tibial nerve MTR and proximal/distal leg Fper values were compared across HNPP and control groups. For the boxplots, the central mark is the median, the edges of the box are the 25th and 75th percentiles, and the whiskers extend to all data points not deemed outliers. Corresponding data from individual patients with HNPP (red) and controls subjects (blue) are overlaid. Significant differences across groups are indicated with black text, while non-significant difference are indicated with gray text.

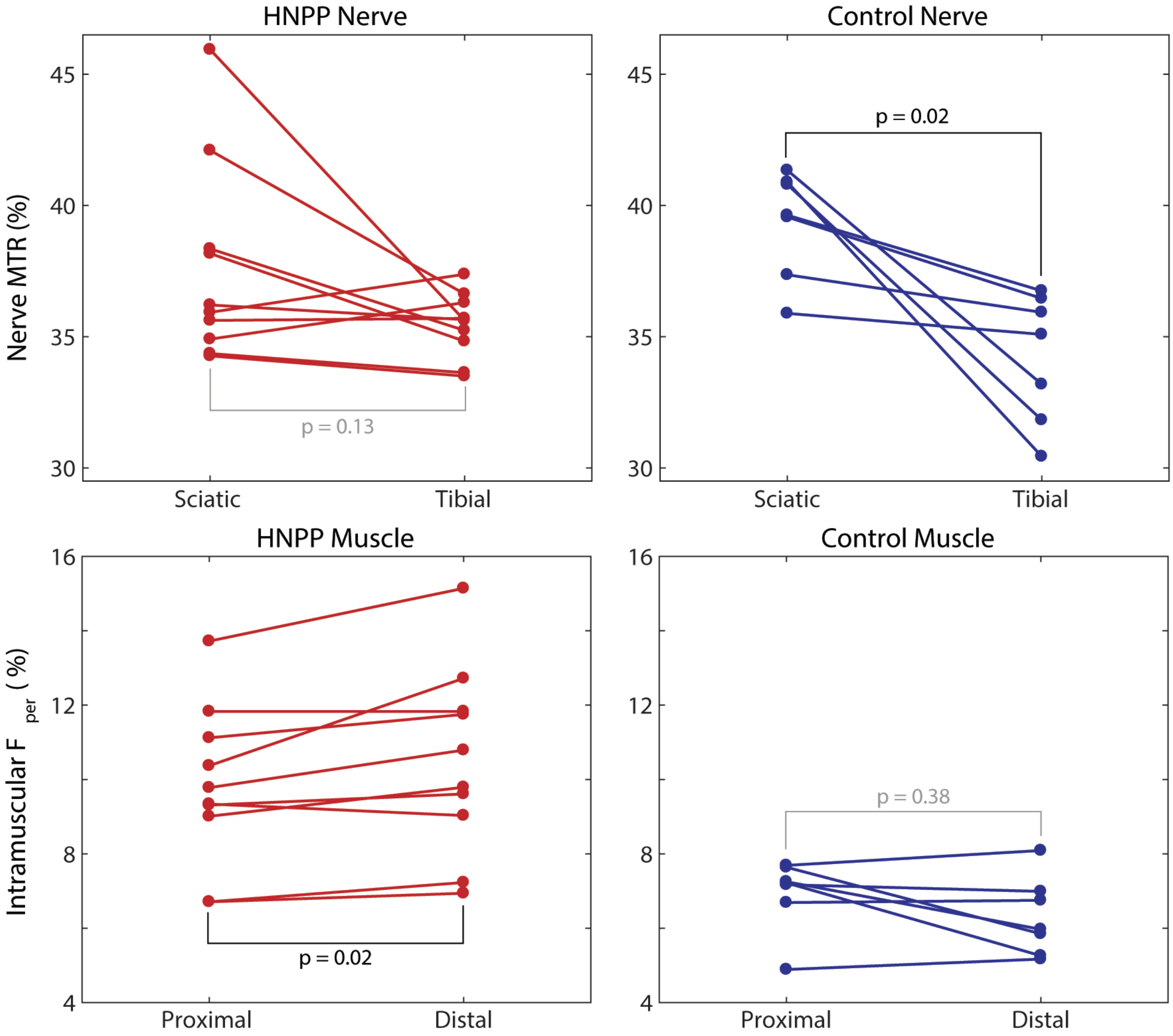

Figure 5-4: Differences between scanning locations per group. HNPP (red) and control (blue) MRI measures (MTR and Fper) were compared across scanning locations (proximal and distal). Each line represents the difference that occurred in a single subject between both scanning locations. Significant differences across locations are indicated with black text, while non-significant difference are indicated with gray text.

Muscle F_{per} values exhibit length-dependent changes

Paired MRI results between proximal and distal tissues per group and MRI metric are shown in Figure 5-4. A significant increase in distal F_{per} values was detected in HNPP patients (proximal/distal muscle = 9.8 ± 2.2/10.5 ± 2.5%, p = 0.02), but not controls (proximal/distal muscle = 6.9 ± 1.0/ 6.3 ± 1.1%, *p* = 0.38), which is consistent with the length-dependent nature of axonal loss. Furthermore, linear regression of the difference between proximal and distal measures across cohorts showed that HNPP patients exhibited significantly stronger length-dependent changes compared to controls (*p* = 0.01, *adjusted* R^2 = 0.35).

In contrast, sciatic and tibial nerve MTR values were similar in HNPP subjects (sciatic/tibial nerves = 39.4 2.0/34.2 2.5%, *p* = 0.13). In addition, although controls (sciatic/tibial nerves = 37.6

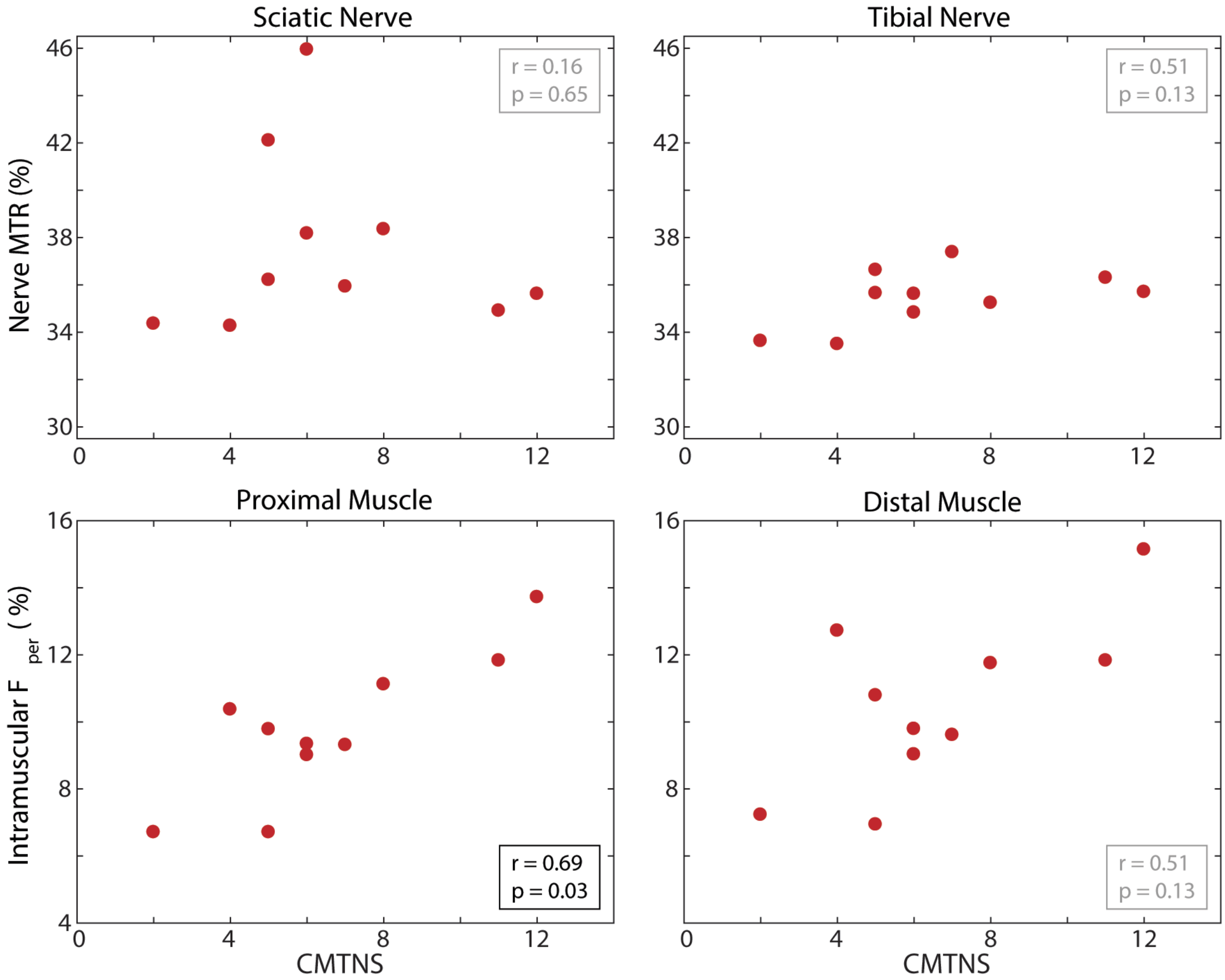

Figure 5-5: MRI measures in patients with HNPP relate to clinical neuropathy score. Sciatic/tibial nerve MTR and proximal/distal muscle Fper measures were correlated to CMTNS scores in the patient group. Significant relationships between MRI measures and CMTNS are indicated with black text, while non-significant relationships are indicated with gray text.

± 3.8/35.5 ± 1.2%, p = 0.02) showed significantly lower values in distal tibial nerves, linear regression of the difference between proximal and distal measures across cohorts did not indicate that this affect was stronger than that observed in patients (p = 0.13, *adjusted* R^2 = 0.09).

Muscle F_{per} *values relate to disability*

As shown in Figure 5-5, a significant relationship was observed between proximal muscle F_{per} and CMTNS measures (r = 0.69, p = 0.03). Sciatic nerve MTR (r = 0.16, p = 0.65), tibial nerve MTR (r = 0.51, p = 0.13), and distal muscle F_{per} (r = 0.51, p = 0.13) were not significantly related to CMTNS.

5.5 Discussion

In this study, we demonstrated that muscle Fper values are elevated in patients with HNPP. The changes in F_{per} support a length-dependent process of denervation that results from axonal loss in the disease. Therefore, despite the multifocal nature of phenotype in HNPP, pathology accumulated over time still results in length-dependent axonal degeneration, which is consistent with previous reports in animal models[122] and human studies in older subjects[124]. In line with previous literature in other types of neuropathies[17], this axonopathy in HNPP appears to be the key factor leading to disabilities since F_{per} value is correlated with CMTNS.

Although numerous biomarkers have been proposed for CMT subtypes (NCS[125], quality of life assessments, sensorimotor testing, CMTNS), they may be compromised in HNPP due to the disease phenotype. For example, although quality of life is affected in HNPP, these surveys are not particularly sensitive to disease progression in inherited neuropathies[80,126]. In addition, CMTNS may be inadequate to describe the progression of HNPP given the transient nature of clinical deficits. For instance, proximal arm weakness by brachial plexopathy may result in a high score of CMTNS, but only lasts a few weeks. Once the weakness recovers, CMTNS would decrease substantially, presenting difficulties in assessing disease progression.

In contrast, MRI can be used as a noninvasive, quantitative, and objective tool to simultaneously assess pathologies in the proximal and distal nerves and muscles of patients with HNPP. In other words, the quantitative MRI methods presented herein may improve our ability to longitudinally study HNPP, provide viable biomarkers for disease progression and treatment response independent of the clinical presentation of HNPP, and may provide insight into the pathogenesis of the disease.

Fat-water MRI exploits the chemical shift difference inherent in fat and water protons in order to generate fat percentage maps of tissue[116,127,128]. Developments in skeletal muscle MRI methods[129,130] have allowed researchers to assay the possible downstream effects of denervation in other inherited neuropathies such as Charcot-Marie-Tooth neuropathy type 1A (CMT1A)[76]. Fat-water measurements have been shown to be valid, reliable[131], and sensitive to CMT1A progression[76], making this method a viable option for use as a disease biomarker for HNPP as they arise from abnormalities in the *PMP22* gene[107].

However, previous studies have focused on single-slice acquisitions. Here, we applied this method to HNPP patients for the first time at multiple levels of limbs. To better assess the relationship between length-dependent axonal loss and disease progression, we performed MRI in the proximal and distal leg, noting that the optimal level of deployment for these measurements may vary across patients and time due to the length-dependent nature of CMT. In this study, we found (i.) F_{per} measures were elevated in HNPP patients relative to controls consistent with previously published findings[76], (ii.) the observed elevation was significantly higher in the distal leg muscles consistent with the length-dependent nature of this disease, and (iii.) F_{per} measures were related to CMTNS disability scores.

One potential drawback of these findings is that fat replacement represents the downstream effect of the nerve pathology and is the chronic endpoint of disease progression and, thus, is unlikely to be reversed with treatment. Additionally, the method only gives us information on motor fibers, and muscle atrophy patterns are not consistent between patients[132]. It should also be noted that these differences may be influenced by factors not associated with the disease process, such as the degree and frequency of exercise[133].

As a result, we deployed our previously developed nerve MTR protocol to overcome these limitations and directly assay peripheral neuropathy in the nerves of the leg. Previous studies have shown that MTR correlates with myelin content changes[67,99,134] that result from de/dysmyelination and axonal loss in the central and peripheral nervous system[135]. Furthermore, previous work has indicated that nerve MTR (i.) is reliable and related to disability across multiple cohorts with inherited neuropathies[101] and (ii.) exhibits proximal-to-distal gradient in controls that increases with age, which is consistent with the findings from the older control cohort studied herein (Figure 5-4, upper-right panel)[136]. In the current study, we measured proximal nerve MTR in HNPP for the first time and used this method in distal leg nerves to probe length-dependent effects. We found that, surprisingly, MTR was similar in controls and patients with HNPP. We postulate that these findings are due to the competing effects of axonal loss, which reduces MTR values, and the formation of tomacula, which is expected to increase MTR values. This is consistent with previous ex vivo nerve studies in mouse models of HNPP, where similar

MT effects were observed in the sciatic nerve of mice with *PMP22* deletions and age-matched wild-type mice[100]. The MTR findings herein are consistent with these ex vivo studies and are supportive of a length-dependent axonal loss superimposed on the aforementioned focal abnormalities in HNPP. When axons degenerate, denervated muscles become atrophic with a fraction of muscles replaced by fat tissues. Thus, muscle F_{per} by MRI provides complementary, albeit indirect, information on axonal loss[137].

Despite promising results, the current study had several limitations. Most notable of these limitations is the sample size. HNPP is a rare disease with an estimated prevalence of 2–5:100,000, although the actual prevalence may be underestimated[111]. The second main limitation is the cross-sectional design of this study. Testing the relationship of BMI and age with our MRI parameters suggests that the observed differences in MRI parameters across cohorts are not confounded by these demographic factors. Nevertheless, longitudinal studies are warranted to investigate the responsiveness of each metric to progression over time. Finally, MTR is only a semiquantitative measure as it is difficult to implement and is sensitive to differences in hardware. For example, although we attempted to correct for B_1 errors, our previous results[101] showed that this can be a source of variance. This can be further visualized in the superficial muscle regions in the control MTR map shown in Figure 5-1, where MTR was overestimated due to large B_1 errors within these regions (red hues). Although we did not observe similar errors within the nerves themselves, this could partially explain why we did not observe a significant relationship between MTR and CMTNS in our analysis. Future work will focus on quantitative MT methods that can overcome these issues and provide more reliable and specific measures of myelin content[138]. In addition, the novel contrast from the MTR sequence may also be useful in other more common neuropathies and/or aid in the anatomical segmentation of nerves[139].

5.6 Conclusion

In conclusion, this study demonstrates the importance of implementing multi-parametric acquisitions (MTR/F_{per}) at multiple scanning locations (proximal/distal leg) to assess HNPP. Our measurements show that (i.) fat percentage is elevated in the HNPP population, (ii.) there are length-dependent changes of fat percentage occurring between the proximal and distal leg locations, and (iii.) fat percentage in proximal muscle correlates with clinical disability in patients with HNPP. Our MTR measures did not detect significant differences between cohorts, and this may be due to the fact that (i.) our HNPP sample size is small and (ii.) MTR values are affected by both myelin content and the formation of tomacula – both of which are occurring in HNPP. These results herein suggest that these measures, particularly muscle fat percentages, may be of value as a biomarker for HNPP disease and warrant further investigation in larger longitudinal studies.

CHAPTER VI

ASSESSMENT OF TRAUMATIC PERIPHERAL NERVE INJURY AND REPAIR WITH DIFFUSION TENSOR IMAGING

6.1 Summary

Clinical management following traumatic peripheral nerve injury requires physicians to rely on qualitative measures from patient history, EMG, and physical exam. The final success or failure of a nerve repair can take months or even years for proximal injuries. The resulting delays in clinical decision-making can lead to a negative impact on patient outcomes because if the nerve repair fails, permanent muscle atrophy and loss of sensorimotor function may occur. The current study aims to test the feasibility of performing diffusion tensor imaging (DTI) in the nerves of the wrist after trauma and surgical repair to provide a noninvasive and reliable assay of regeneration, which may improve clinical decision-making and possibly alter outcomes after surgical interventions. Measurements from subjects with milder compressional injury (Carpal Tunnel Syndrome) and healthy control subjects will shed light to the relationship between DTI indices and injury severity. Results showed that not only was DTI sensitive in measuring differences between healthy, compressed, and injured nerves, but that longitudinal measures in two injury subjects related to clinical outcomes.

6.2 Introduction

Peripheral nerve damage following injury can result in catastrophic clinical outcomes if not detected or treated in a timely manner. Etiologies of peripheral neuropathy can be divided into traumatic (e.g. motor vehicle, penetrating, crush, iatrogenic injuries, etc.) and nontraumatic causes (e.g. compression, infection, and inflammatory, etc.). Traumatic peripheral nerve injury (TPNI) typically has devastating impacts on quality of life and may result in temporary or permanent paralysis, irreversible muscle atrophy, and/or formation of painful neuromas[140]. TPNI's occur in 3-5% of Level 1 trauma cases and result in approximately 100,000 surgeries in North America per year[141,142] and have been noted in recent military missions[143,144]. Literature has shown[140,141,145,146] that upper extremities are more frequently involved in TPNI, most commonly affecting the brachial plexus, median, ulnar, and radial nerves.

Neurotmesis of the upper extremities is a common, but severe, injury wherein a single nerve is completely transected or severely lacerated. This injury type typically warrants surgical intervention to reestablish connections between the proximal and distal ends of the injured nerve. Successful recovery requires axons grow from the repair site to the target tissue at a growth rate of approximately one inch per month[140]. Nerve grafts can reduce the length of axonal growth required to reach target tissue; however, approximately 40% of surgical repairs fail following these injuries[147,148]. Clinical management following a TPNI entails electrodiagnostic testing, often paired with “watch and wait” methodology for weeks to months, forcing physicians to rely mostly on the patient's history and physical exams. Using current management, nerve growth failure goes unnoticed for extended periods, during which the window of opportunity for a revisional surgery closes, leading to irreversible muscle atrophy due to prolonged muscle denervation[149].

Following a traumatic extremity injury, current diagnostic tools are limited to clinical examinations and electrodiagnostic tests[17]. For example, nerve conduction studies (NCS) and electromyography (EMG) remain the mainstay for defining the severity and distribution of motor and sensory function following a TPNI; however, reinnervation typically does not begin until three to six weeks following an inciting event. During regeneration, NCS and EMG together provide incomplete pictures of nerve pathology[150]. Additionally, these tests fail to definitively discriminate a severe neurotmesis (axonotmesis laceration), involving division of axons and elements of the epineurium, from a mild self-resolving neuropraxic injury[17,150–153], such as compression, in the acute setting prior to surgical intervention.

Given the time sensitive nature of nerve regeneration, high resolution ultrasonography (HRUS) and magnetic resolution neurography (MRN) imaging have been proposed to mitigate current diagnostic limitations and to explore peripheral nerve regeneration mapping. HRUS can accurately identify transected nerves[154,155]; however, its use is limited in traumatic injuries due to associated large hematomas, edema, skin lacerations, and alterations of the normal anatomy[154]. Conventional magnetic resonance imaging (MRI) of nerves allows for both longitudinal and cross-sectional fascicular images to detect nerve discontinuity, localize nerve compression, and decipher intraneural masses from perineural[87]. Areas affected by peripheral neuropathy demonstrate hyperintense changes on MRI T_2-weighted sequences which can characterize myelin and axonal health; however, MRN alone cannot discriminate between myelin and axonal pathologies and, therefore, lacks specificity[156].

Diffusion Tensor Imaging (DTI) is a quantitative MRI method that has been shown to be particularly effective in detection and monitoring of central nervous system (CNS) pathologies such as traumatic brain injury, spinal cord injury, and even multiple sclerosis[157–159]. This method has also shown promising results in the detection of myelin and axon pathology in distal nerves of the wrist[96,160]; and DTI has previously been shown useful for detecting peripheral nerve regeneration as early as one to three months in humans[92,161,162]. DTI provides a noninvasive, quantitative approach to probe tissue microstructures throughout the recovery process by measuring the apparent diffusion of water molecules in tissue over multiple directions[163]. In the absence of barriers, diffusion is isotropic or equal in all directions. Conversely in ordered, elongated biological tissue like peripheral axons, water diffusion is anisotropic due to its interactions with surrounding tissue structures and cellular membranes, resulting in an apparent diffusivity that is highest along the primary direction of the axons[161,163,164].

To address the present clinical shortcomings in treatment and detection of traumatic peripheral nerve injury, we aimed to determine the sensitivity of DTI indices to monitor nerve degeneration and regeneration following TPNI and surgical repair. In previous animal studies, high-resolution DTI was used to successfully identify and grade complete and partial transections of sciatic nerves in ex vivo rats[165,166]. In this study, we employed DTI on distal nerves of the human wrist to longitudinally evaluate nerve repair procedures. In addition, we included a cohort of CTS patients to compare the sensitivity of this method to less severe, compression injuries. If successful, these DTI strategies could help improve patient outcomes by predicting failures much earlier than current techniques, and even provide evidence for re-operation.

6.3 Methods

Human Subjects and Clinical Information

Three subjects with TPNI, eight subjects with CTS, and eight healthy control subjects were enrolled in this study. All TPNI subjects underwent surgical repairs of the fully lacerated median and/or ulnar nerve(s) and were treated with the standard nerve anastomosis procedure for clinical care at Vanderbilt University Medical Center (VUMC). All CTS subjects underwent carpal tunnel release surgery and were treated with the standard clinical care procedure at VUMC. All healthy controls were volunteers. Subjects and healthy volunteers were excluded from recruitment if they reported a history of other concurrent neuropathies (e.g., diabetic neuropathies) or wrist trauma.

For TPNI cases, a Brunner's incision was made and dissected proximally and distally. The nerves and/or tendons were explored and the damage was identified. If necessary, the Brunner's incision was extended across the carpal tunnel, and care was taken to preserve branches of the median nerve throughout the dissection. Transected nerve endings were inspected, edges were refreshed to healthy tissue, if needed, and epineural repair was performed with 8-0 nylon sutures, taking care to all align vascular structures to optimize fascicular repair.

In carpal tunnel release surgery, an incision was made at the base of the palm of the hand. Through this incision, surgeons located the carpal tunnel ligament, which lies between the skin and the median nerve in the carpal tunnel. By lacerating the carpal tunnel ligament, more room was given to free up space in the already crowded, and sometimes inflamed, carpal tunnel. Giving this free space typically allows for compression of the median nerve to be alleviated and relieves painful symptoms of CTS.

As detailed in Table 6-1, the median nerve was affected by compression in the CTS cohort. From the TPNI cohort, two of the three TPNI subjects had an injury where only one nerve was affected (TPNI 1 and TPNI 3). The other TPNI subject had both median and ulnar nerve injuries (TPNI 2) on the right arm and was dual-enrolled in another clinical trial at VUMC in which a sealant material composed of polyethylene glycol (PEG) and hypotonic calcium free saline was applied directly to the repaired nerve adjunctive to the microsurgical repair. PEG has demonstrated safety in human usage[167,168] and PEG fusion has proven effective in terms of functional outcomes and speed of nerve recovery in human digital nerves when compared to standard nerve repair[169,170]. More specifically, TPNI 1 presented with a linear laceration of the median nerve in the dominant right arm. Along with repair of the median nerve, surgical repair was done on the complete transections of the flexor capri radialis tendon, the palmaris longus tendon, the flexor pollicis longus tendon, and partial transection of the flexor distal phalanx tendon. TPNI 2 presented full transection of the median nerve and partial transection of the ulnar nerve in the dominant right arm. Concomitant with this trauma was a flexor tendon injury, which was also repaired. TPNI 2 received PEG gel as part of the median nerve repair. TPNI 3 presented partial transection of the ulnar nerve on the non-dominant left arm. Along with nerve trauma, TPNI 3 had damaged the flexor carpi ulnaris and flexor digitorum superficialis tendons. Additionally, carpal tunnel release surgery was performed on the median nerve as part of the repair procedure. After the second longitudinal timepoint clinical information indicated that the initial repair surgery was not successful; therefore, TPNI 3 was re-operated with an Avance 70 x 5 mm nerve graft.

All TPNI subjects underwent MRI one to three months after surgical repair. Additional longitudinal data were collected in three-month intervals after previous scanning in two of the three TPNI subjects. All CTS subjects had an MRI one to five months after carpal tunnel release surgery, with the exception of one subject who had MRI less than a month before surgery. Additional longitudinal data were collected in six of the eight CTS subjects when available. Additional clinical assessments were conducted on TPNI subjects, including: Michigan Handedness Questionnaire (MHQ), Grip test, and 9-hole Peg Test (9-HPT). Clinical assessments for CTS subjects are not reported. During the consenting process, subjects self-reported no symptoms that were suggestive of peripheral nerve diseases and physical examination indicated no evidence of other peripheral neuropathies. Each subject’s demographic information and clinical scores (when available) are reported in Table 6-1.

	Demographics:			**Time:**	**MHQ:**		**Grip test:**		**9-HPT:**	
	Age (Sex)	BMI	Arm - Nerve		Injured	Healthy	Injured	Healthy	Injured	Healthy
TPNI 1	26 (F)	19.7	R - M	1	N/A	N/A	N/A	N/A	N/A	N/A
TPNI 2	22 (M)	19.8	R - M & U	1	33	83.3	Unable	92	Unable	23
				4	69	83.3	30	100	100	27
TPNI 3	52 (M)	31.8	L - U	3	5.0	75.1	30	75	43	27
				6	0.8	81.5	18	74	51	26
				9*	5.8	81.5	N/A	N/A	N/A	N/A
Group:	***33.3 (66% M)***	***31.8***								
CTS 1	73 (M)	23.5	R - M							
CTS 2	48 (F)	34.4	R - M							
CTS 3	58 (F)	26.6	R - M							
CTS 4	40 (M)	26.6	R - M							
CTS 5	44 (F)	30.8	L - M							
CTS 6	48 (F)	38.4	R - M							
CTS 7	52 (F)	32.0	R - M							
CTS 8	68 (M)	31.4	R - M							
Group:	***53.3 (38% M)***	***30.5***								
Control 1	57 (M)	23.1	R - M							
Control 2	54 (F)	32.7	R - M							
Control 3	23 (M)	23.8	R - M							
Control 4	27 (M)	19.3	R - M							
Control 5	27 (M)	28.8	R - M							
Control 6	20 (M)	26.5	R - M							
Control 7	25 (M)	30.1	R - M							
Control 8	26 (M)	21.0	R - M							
Group:	***32.4 (88% M)***	***25.7***								

Table 6-1: Demographic information and clinical scores for all subjects. Includes Michigan Handedness Questionnaire (MHQ) and 9-hole Peg Test (9-HPT). Score of N/A indicates where measures were not obtained. Score of unable may also be considered a score of zero. Multiple scores for TPNI 2 and TPNI 3 reflect measures gained at subsequent clinical visits. R = Right arm and L = Left arm. M = Median nerve and U = Ulnar nerve. Time listed in months since surgery (* indicates measures acquired after second surgery in TPNI 3).

MRI Data Acquisition

Subjects were imaged in the prone position with one arm extended above the head (i.e., "superman" position) with a 3.0-T Philips Achieva MR scanner. An 8-channel wrist coil was used for RF reception in all subjects expect one, where a larger 16-channel knee coil was used due to a cast covering the arm. In each MRI session, the arm with the most recent injury and surgery were scanned followed by the contralateral, uninjured arm next as an internal control. A high-resolution, single-shot DTI scan was performed at a slice thicknesses of 4-mm with 10-16 slices in each subject. Additional parameters included: resolution = 0.75 x 0.75 x 4 mm^3 (wrist coil) or 1.25 x 1.25 x 8 mm^3 (knee coil), TR/TE = 3000/53 ms, number of acquisitions = 12, 16 directions, max b-factor of 800 s/mm^2, and scan time ≈ 11 minutes.

MRI Data analysis

MATLAB[171] was used for tensor estimation and image registration. Regions of interest (ROIs) were manually selected using the MIPAV[172] imaging software on all slices for the injured and contralateral nerve(s), and mean slice-wise values were estimated for fractional anisotropy (FA), mean diffusivity (MD), radial diffusivity (RD), and axial diffusivity (AD). In addition, these results are reported in Table 6-2.

Subject	Time Post-Surgery	State (Nerve)	FA ± SD	MD ± SD	AD ± SD	RD ± SD
TPNI 1	1 month	Injured (Ulnar)	0.45 ± 0.11	1.08 ± 0.23	1.72 ± 0.31	0.77 ± 0.22
	N/A	Contralateral	0.57 ± 0.15	0.92 ± 0.18	1.64 ± 0.26	0.56 ± 0.19
TPNI 2	1 month	Injured (Median)	0.29 ± 0.05	1.39 ± 0.19	1.86 ± 0.24	1.16 ± 0.17
	N/A	Contralateral	0.55 ± 0.13	1.10 ± 0.25	1.90 ± 0.40	0.70 ± 0.20
	4 months	Injured (Median)	0.33 ± 0.07	1.45 ± 0.22	1.99 ± 0.30	1.18 ± 0.20
	N/A	Contralateral	0.53 ± 0.17	1.18 ± 0.34	2.00 ± 0.50	0.77 ± 0.31
	1 month	Injured (Ulnar)	0.33 ± 0.07	1.45 ± 0.17	1.99 ± 0.18	1.18 ± 0.19
	N/A	Contralateral	0.51 ± 0.17	1.12 ± 0.34	1.83 ± 0.49	0.76 ± 0.30
	4 months	Injured (Ulnar)	0.37 ± 0.10	1.36 ± 0.28	1.93 ± 0.34	1.07 ± 0.27
	N/A	Contralateral	0.60 ± 0.18	1.04 ± 0.29	1.93 ± 0.48	0.59 ± 0.23
TPNI 3	3 months	Injured (Ulnar)	0.31 ± 0.07	1.46 ± 0.22	1.97 ± 0.26	1.21 ± 0.22
	N/A	Contralateral	0.41 ± 0.13	1.15 ± 0.30	1.74 ± 0.46	0.85 ± 0.25
	6 months	Injured (Ulnar)	0.17 ± 0.06	1.81 ± 0.27	2.13 ± 0.32	1.65 ± 0.26
	N/A	Contralateral	0.32 ± 0.11	1.28 ± 0.36	1.78 ± 0.47	1.03±0.32
	9 months*	Injured (Ulnar)	0.29 ± 0.12	1.29 ± 0.24	1.68 ± 0.27	1.09 ± 0.26
	N/A	Contralateral	0.36 ± 0.08	1.22 ± 0.21	1.75 ± 0.27	0.96 ± 0.20
Group:		***Injured***	***0.32 ± 0.06***	***1.41 ± 0.15***	***1.91 ± 0.19***	***1.16 ± 0.15***
		Contralateral	***0.48 ± 0.14***	***1.13 ± 0.28***	***1.82 ± 0.42***	***0.78 ± 0.25***
CTS 1	5 months	Compressed (Median)	0.45 ± 0.04	1.24 ± 0.08	1.88 ± 0.09	0.92 ± 0.09
	16 months	Compressed (Median)	0.46 ± 0.03	1.20 ± 0.05	1.87 ± 0.05	0.87 ± 0.06
	20 months	Compressed (Median)	0.41 ± 0.03	1.10 ± 0.07	1.59 ± 0.07	0.85 ± 0.08
	24 months	Compressed (Median)	0.46 ± 0.03	1.20 ± 0.05	1.87 ± 0.05	0.87 ± 0.06
CTS 2	4.5 months	Compressed (Median)	0.43 ± 0.03	1.37 ± 0.05	2.04 ± 0.06	1.03 ± 0.06
	13.5 months	Compressed (Median)	0.35 ± 0.02	1.27 ± 0.04	1.77 ± 0.04	1.02 ± 0.05
	16.5 months	Compressed (Median)	0.43 ± 0.02	1.15 ± 0.04	1.74 ± 0.05	0.85 ± 0.04
CTS 3	1 month	Compressed (Median)	0.41 ± 0.02	1.23 ± 0.04	1.84 ± 0.04	0.93 ± 0.05
	12 months	Compressed (Median)	0.43 ± 0.02	1.33 ± 0.04	2.01 ± 0.06	0.99 ± 0.05
	16 months	Compressed (Median)	0.41 ± 0.02	1.20 ± 0.19	1.80 ± 0.28	0.90 ± 0.17
CTS 4	4 months	Compressed (Median)	0.46 ± 0.02	1.23 ± 0.05	1.90 ± 0.07	0.89 ± 0.05
	14 months	Compressed (Median)	0.42 ± 0.04	1.32 ± 0.07	1.95 ± 0.07	1.00 ± 0.08
CTS 5	<1 month	Compressed (Median)	0.51 ± 0.04	1.24 ± 0.08	1.97 ± 0.08	0.88 ± 0.09
	3.5 months	Compressed (Median)	0.43 ± 0.04	1.31 ± 0.06	1.94 ± 0.05	0.99 ± 0.07
CTS 6	1 month	Compressed (Median)	0.44 ± 0.01	1.36 ± 0.02	2.09 ± 0.04	0.99 ± 0.03
	14 months	Compressed (Median)	0.45 ± 0.02	1.28 ± 0.04	1.98 ± 0.06	0.93 ± 0.04
CTS 7	6 months	Compressed (Median)	0.30 ± 0.04	1.47 ± 0.08	1.87 ± 0.10	1.28 ± 0.09
CTS 8	2 months	Compressed (Median)	0.46 ± 0.03	1.23 ± 0.05	1.91 ± 0.04	0.89 ± 0.06
Group:			***0.43 ± 0.03***	***1.27 ± 0.06***	***1.90 ± 0.06***	***1.01 ± 0.06***

Control 1	N/A	Healthy (Median)	0.54 ± 0.03	1.13 ± 0.04	1.91 ± 0.04	0.74 ± 0.05
Control 2	N/A	Healthy (Median)	0.39 ± 0.03	1.25 ± 0.05	1.82 ± 0.05	0.96 ± 0.06
Control 3	N/A	Healthy (Median)	0.54 ± 0.02	1.07 ± 0.06	1.79 ± 0.05	0.71 ± 0.06
Control 4	N/A	Healthy (Median)	0.61 ± 0.03	1.04 ± 0.05	1.86 ± 0.05	0.62 ± 0.05
Control 5	N/A	Healthy (Median)	0.64 ± 0.03	1.09 ± 0.08	1.99 ± 0.09	0.64 ± 0.08
Control 6	N/A	Healthy (Median)	0.70 ± 0.02	0.95 ± 0.03	1.89 ± 0.04	0.49 ± 0.04
Control 7	N/A	Healthy (Median)	0.64 ± 0.04	1.07 ± 0.04	2.00 ± 0.03	0.60 ± 0.06
Control 8	N/A	Healthy (Median)	0.66 ± 0.03	1.11 ± 0.03	2.10 ± 0.03	0.61 ± 0.04
Group:			***0.59 ± 0.03***	***1.09 ± 0.05***	***1.92 ± 0.05***	***0.67 ± 0.05***

Table 6-2: Results of DTI metrics for each subject at each timepoint for each nerve. N/A refers to no surgery. CTS 5 had diagnosis of carpal tunnel syndrome, but had not yet received treatment at first scan. The units of mean diffusivity (MD), axial diffusivity (AD),and radial diffusivity (RD) are 10^{-3} mm^2/s. * indicates measures acquired after second surgery in TPNI. 3.

Statistical Analysis

All statistical analyses were conducted using MATLAB Statistics and Machine Learning Toolbox Release 2017a[119]. All measures for comparison were derived from DTI metrics, including FA, MD, RD, and AD. Non-parametric statistical approaches were used in this study's analysis due to the small sample size of the study, and raw p-values are reported given the exploratory nature of this study. To test the effect of slice measurements in healthy data and see if there are any significant differences in the area in which we image, slice-wise variations in FA were evaluated via a Kruskal-Wallis test. Next, we conducted a cross-sectional analysis across all cohorts (TPNI, CTS, Control) and timepoints to evaluate the effect of injury severity on the observed DTI metrics in nerves via Wilcoxon Rank-Sum tests. In addition to this, we compared mean (across all slices and timepoints, when available) DTI metrics between injured and contralateral nerves in the same TPNI patients via Wilcoxon Rank-Sum tests. Finally, we compared FA of injured and healthy nerves in individual TPNI subjects longitudinally (when available) via Wilcoxon Rank-Sum to assess each subjects' recovery over time.

6.4 Results

Clinical data

Clinical measures obtained from all subjects in injured and healthy arms are summarized in Table 6-1. TPNI 1 did not participate in these clinical measures. Clinical findings for TPNI 2 show improvement between timepoints (1/2) across all measures for MHQ (33.0/69.0), Grip test (Unable/30), and 9-HPT (Unable/100 sec.). TPNI 3 participated in all clinical assessments for the first and second timepoints, but only participated in the MHQ assessment at the third timepoint. Results of TPNI 3 show decline in all measures between timepoints (1/2) for MHQ (5.0/0.8), Grip test (30/18), and 9-HPT (43 sec./51 sec.). After re-operation, the MHQ score rose above the first measure (5.8).

Representative Data in Control, TPNI, and CTS

The MRI scanning procedure was well-tolerated by all subjects. The MR images acquired were artifact-free from chemical shift from fat and had very little motion. In the anatomical and diffusion images, the nerves were easily distinguishable from surrounding tissue (Figure 6-1).

Kruskal-Wallis results of healthy data from control subjects were not significant (p = 0.182), indicating that slice-wise measures of FA did not differ along the area in which we scanned. This finding allowed us to treat healthy data as a constant measure in the individual TPNI subjects' results, thus contralateral nerve values were averaged across all slices with confidence intervals included to display the range of healthy measures per TPNI individual. Additionally, there were no significant changes over timepoints after surgery in FA of CTS subjects ($r^2 = 0.039$, $p = 0.430$).

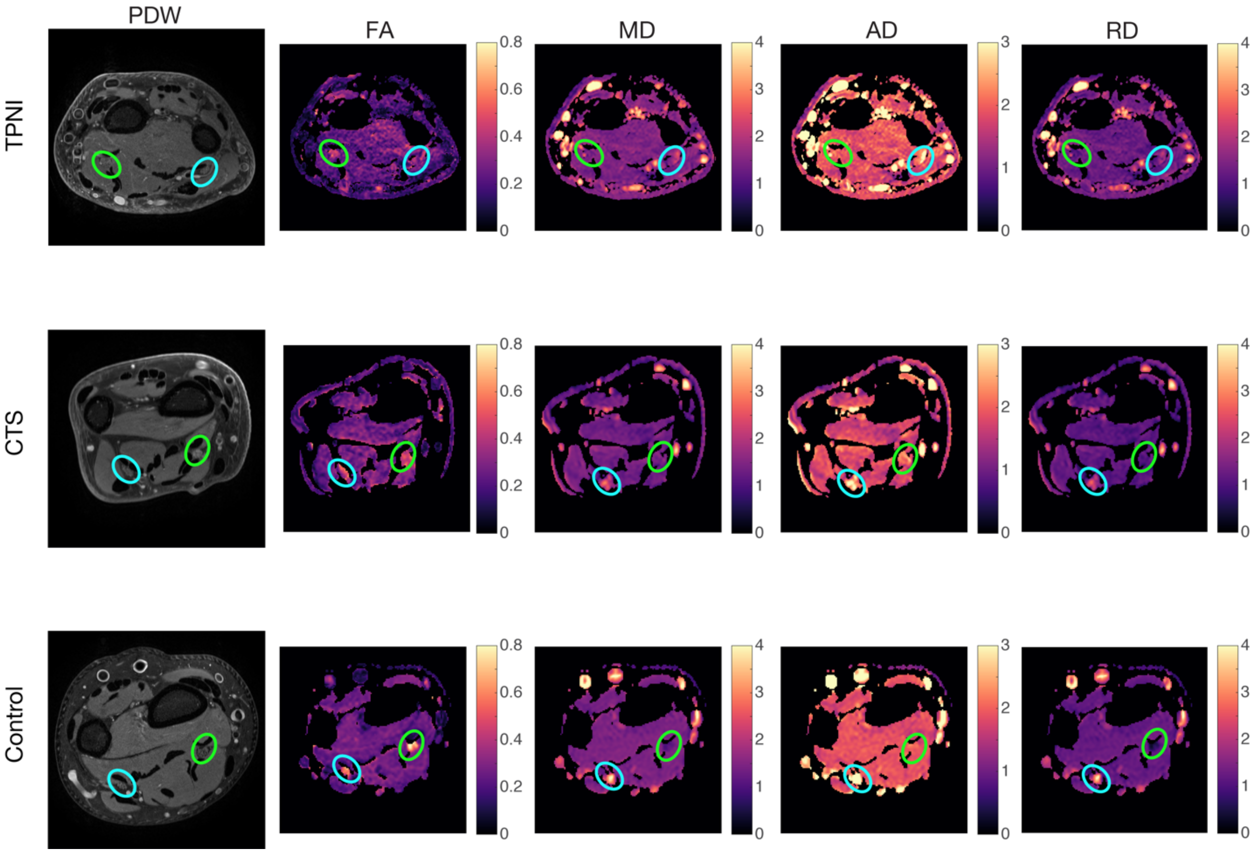

Figure 6-1: Representative Images of all groups and all metrics: Proton-Density Weighted (PDW), fractional anisotropy (FA), mean diffusivity (MD), axial diffusivity (AD), and radial diffusivity (RD) maps show for traumatic peripheral nerve injury cohort (TPNI), carpal tunnel syndrome cohort (CTS), and control cohort. Green circles indicate the median nerve. Blue circles represent the ulnar nerve.

Cross-sectional analysis across cohorts with different injury severities

For comparison to milder injury and heathy nerve, all the TPNI data that was acquired across time was compared to carpal tunnel syndrome and control data (Figure 6-2). TPNI showed significant differences when compared to CTS for FA ($p = 0.004$), MD ($p = 0.024$), and RD ($p = 0.008$); and when compared to control data for FA ($p < 0.001$), MD ($p = 0.002$), and RD ($p < 0.001$). Additionally, carpal tunnel and control data showed significant differences for FA ($p = 0.002$), MD ($p = 0.001$), and RD ($p = 0.001$). There was no significance for AD in any of these cohort comparisons ($p > 0.846$). This analysis included all longitudinal timepoints for both TPNI and CTS groups.

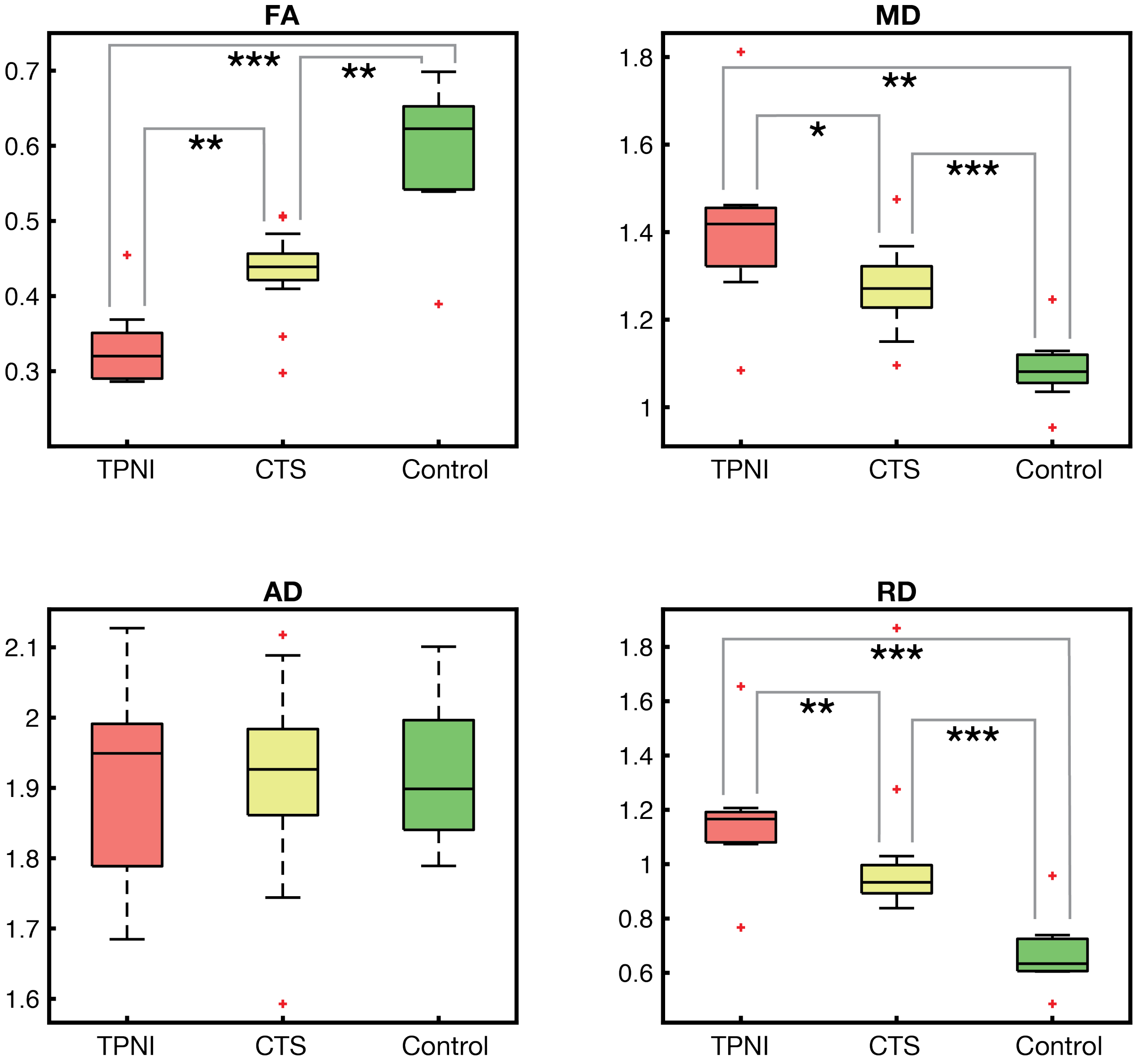

Figure 6-2: Results of all TPNI, CTS, and Control subjects and timepoints for all DTI metrics acquired. FA (top-left), MD (top-right), AD (bottom-left), and RD (bottom-right). The black central mark represent the median, whiskers represent the most extreme data points not considered outliers, and the red crosses are individually plotted outliers. Significant relationships indicated by Wilcoxon Rank Sum test between groups are indicated by asterisk ($p < 0.05$ *, $p < 0.01$ **, $p < 0.001$ ***). Includes all longitudinal data for TPNI and CTS subjects. The units of mean diffusivity (MD), axial diffusivity (AD),and radial diffusivity (RD) are 10^{-3} mm^2/s.

Cross-sectional analysis of Injured & Contralateral Nerve in TPNI

At the group level, injured and healthy nerves indicated significant differences across all slices for FA (p = 0.007), MD, (p = 0.005), and RD (p = 0.001), but not AD (p = 0.279). These results are illustrated in Figure 6-3. It is worth noting there exist more variability for injured DTI parameters than healthy, which is likely due to combining the measurements of the proximal and distal slices of the injured nerve data in this analysis.

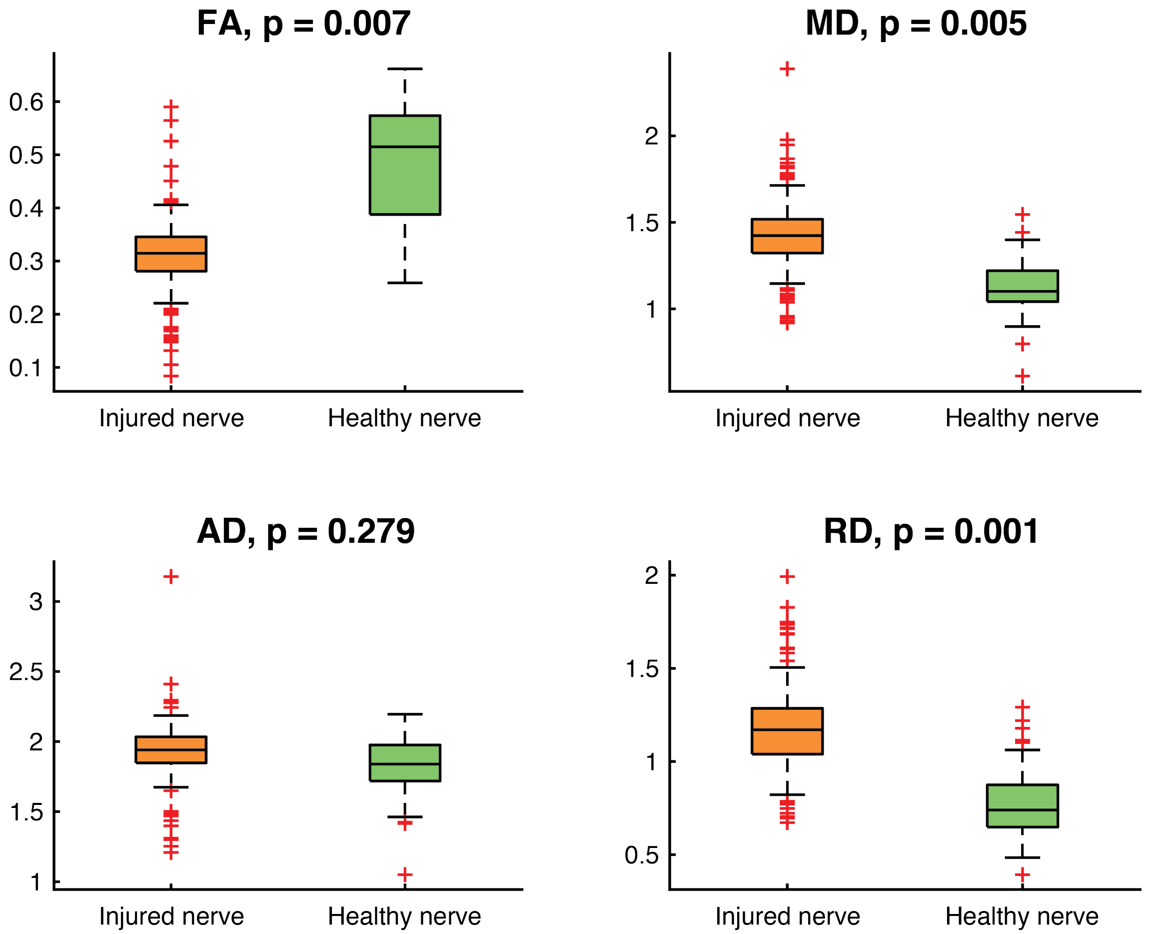

Figure 6-3: Injured and healthy nerves. Results of TPNI subjects and timepoints comparing injured nerve data to the contralateral healthy nerve data for all DTI metrics acquired: FA (top-left), MD (top-right), AD (bottom-left), and RD (bottom-right). The red central mark represent the median, blue boxes indicate the 75th and 25th percentile, whiskers represent the most extreme data points not considered outliers, and the red crosses are individually plotted outliers. P-values of Wilcoxon Rank Sum test are shown above each boxplot. The units of mean diffusivity (MD), axial diffusivity (AD),and radial diffusivity (RD) are 10^{-3} mm^2/s.

The difference in measures between the injured and healthy nerve is further illustrated for a single subject in Figure 6-4, where lower FA values are present in the injured ulnar nerve, and higher FA values in the healthy ulnar nerve in both proximal and distal images. Note that while Figure 6-4 shows images of TPNI 3, this phenomenon was observed in the other two TPNI subjects as well.

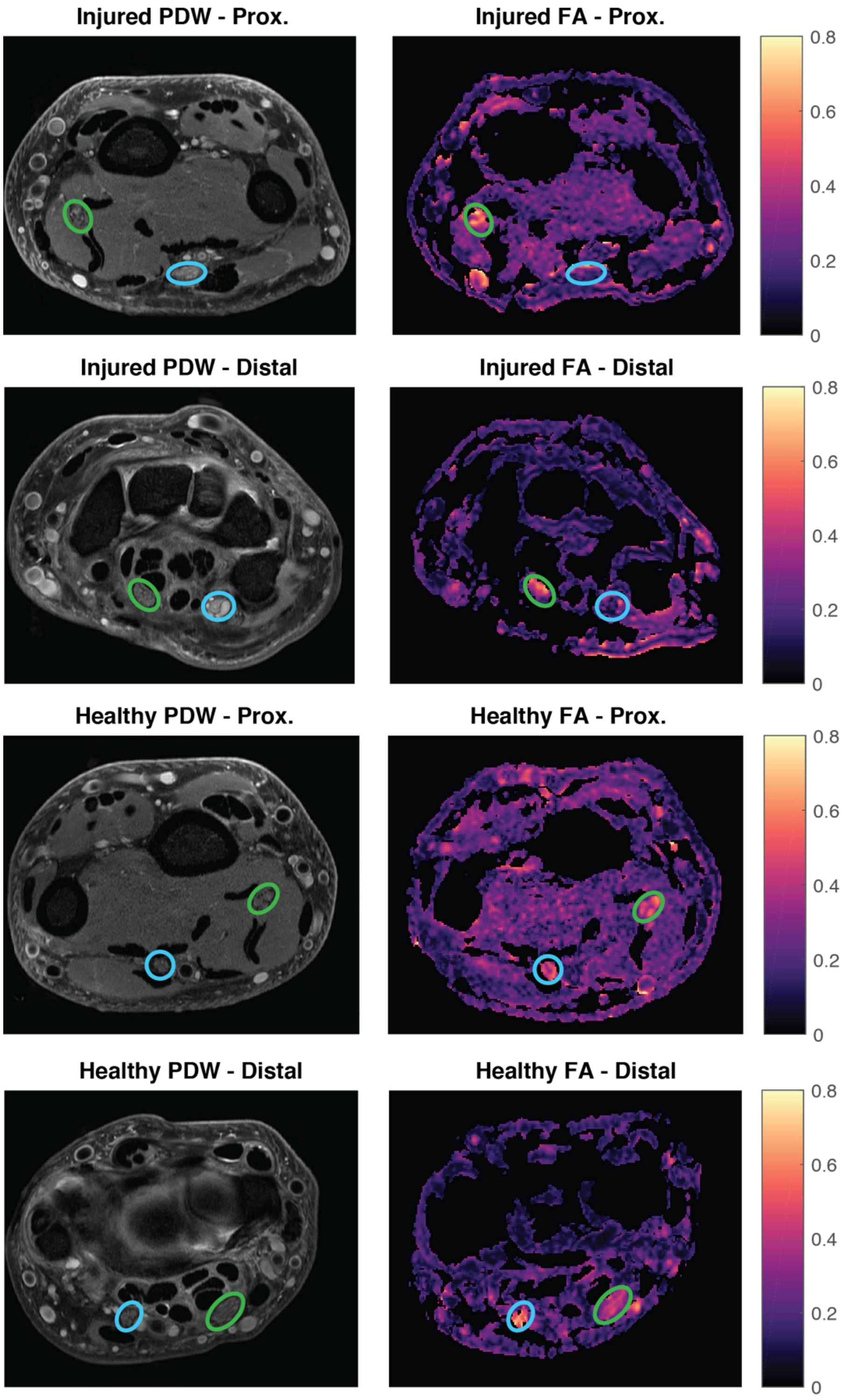

Figure 6-4: Proton Density-Weighted (PDW) and Fractional Anisotropy (FA) maps for injured and healthy nerves in TPNI 3. Green circles indicate the median nerve. Blue circles represent the ulnar nerve. Worth nothing are the differences in intensity between the injured ulnar nerve and healthy ulnar nerve.

Figure 6-5 further illustrates the differences seen between the four DTI measures in TPNI 3. The FA map shows the healthy median nerve with higher values than the injured ulnar nerve. MD, AD, and RD maps show the opposite effect, where values in the injured ulnar nerve are higher than the healthy median nerve, which we could expect would calculate low FA. This was also observed in the other two subjects.

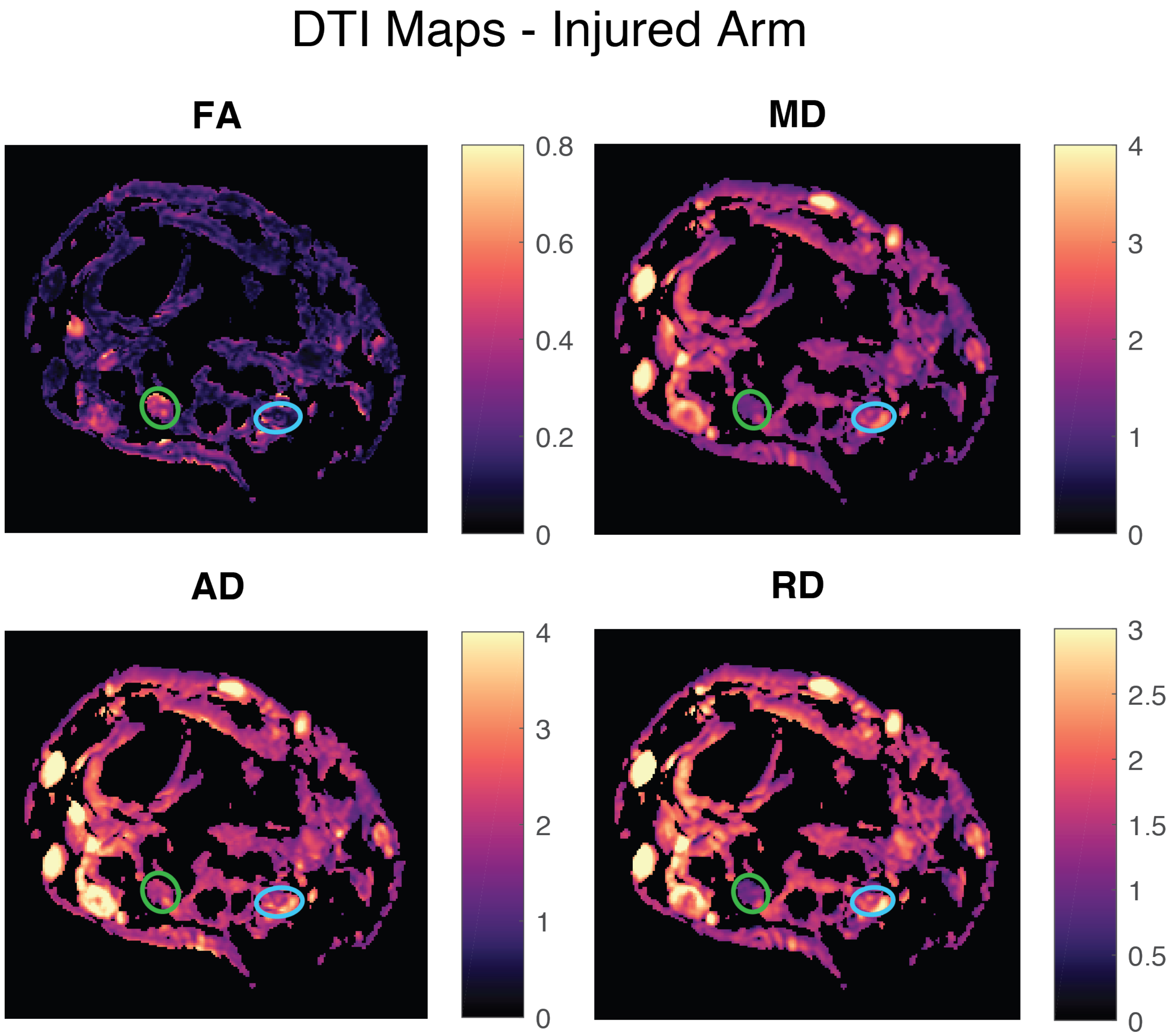

Figure 6-5: Diffusion Tensor Imaging (DTI) maps: Fractional Anisotropy (FA), Mean Diffusivity (MD), Axial Diffusivity (AD), and Radial Diffusivity (RD) in Patient 3. Green circles indicate the median nerve. Blue circles represent the ulnar nerve. The units of mean diffusivity (MD), axial diffusivity (AD),and radial diffusivity (RD) are 10^{-3} mm^2/s.

Subject TPNI 1:

In the first subject, TPNI 1, a comparison of FA between the right arm with the repaired median nerve to the left arm with the uninjured median nerve was shown to be significant (*p* = 0.021). Figure 6-6 shows the slice-wise measurements for FA in the injured and uninjured median nerves of Subject 1, with more proximal slices (slice 1-4) of the injured nerve within the boundary of the measures we observed in the healthy nerve. As we move more distal towards the injury site in slices (5-8), we can see that the FA values now fall outside of the confidence intervals, with the lowest measure being at slice 6 and continuing upwards as we move down distal slices.

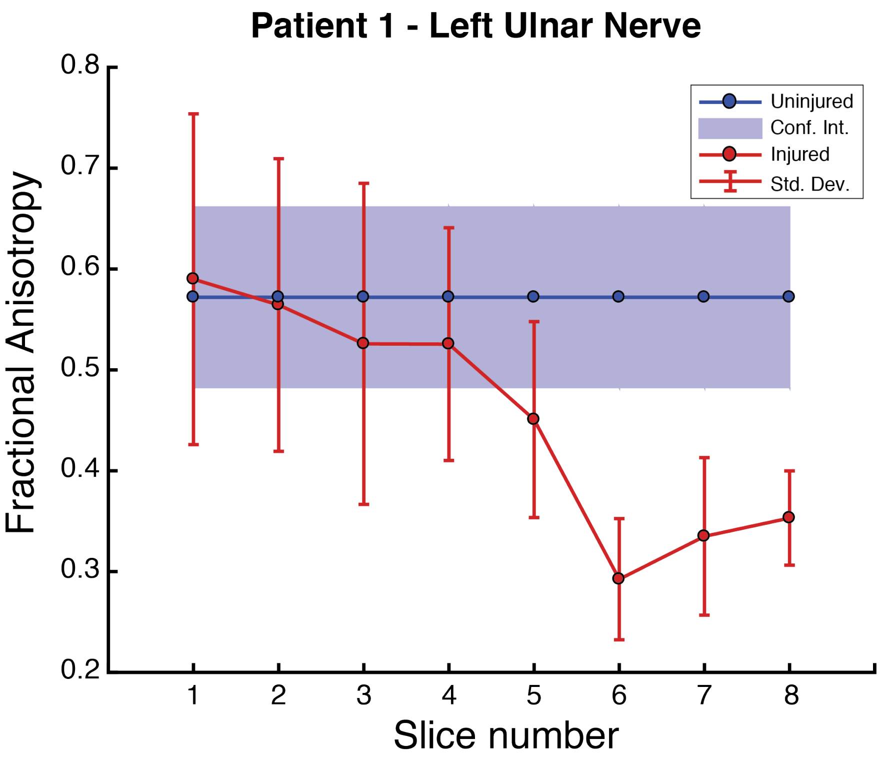

Figure 6-6: Results for TPNI 1: Fractional Anisotropy plotted by slice. Blue line/dots reflect averaged healthy ulnar nerve across all slices; shaded blue areas are the 95% confidence interval for averaged healthy data. Red line/dots reflect individual data points of the injured ulnar nerve, with bars showing slice-wise standard deviation.

Figure 6-7 visualizes this data through diffusion fibertracking of the injured median nerve in the right arm, showing site of injury and how FA values drop as we move distal from the injury towards the hand.

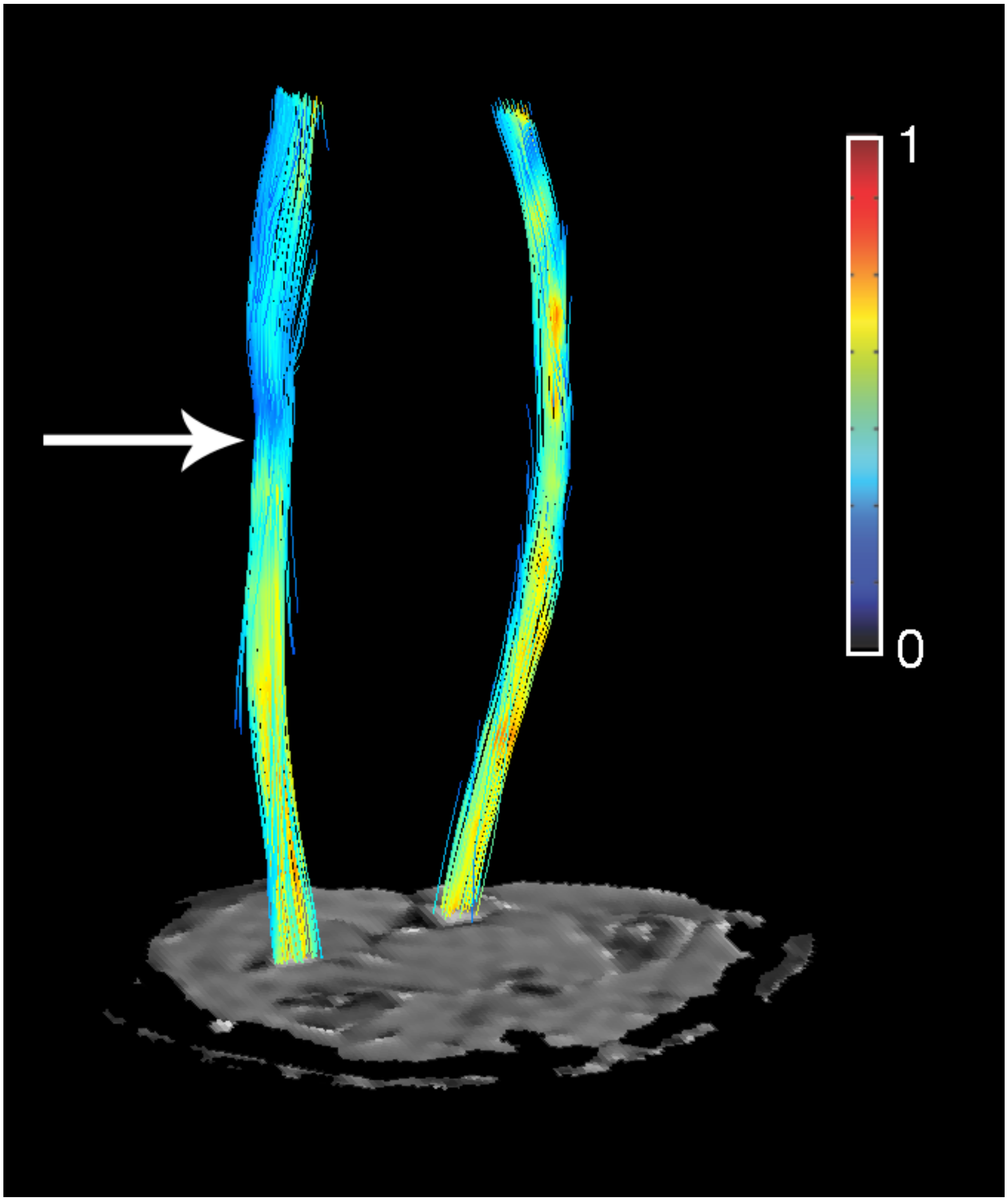

Figure 6-7: Fibertracking results of TPNI 1 with right arm median nerve injury. Proximal slice shown at the bottom of the image with ascending fiber tracking of the injured ulnar nerve (left) and healthy median nerve (right). White arrow indicates area of injury. Nerve is color-coded to fractional anisotropy (FA). Colorbar on right.

Subject TPNI 2:

In the second subject, TPNI 2, a comparison of the FA of the right arm, injured median and ulnar nerves, to the left arm, uninjured median and ulnar nerves, showed significance across both longitudinal timepoints ($p < 0.001$, in all cases). Figure 6-8 shows the slice-wise measurements for FA in the injured and uninjured median and ulnar nerves of TPNI 2. From 1 month post-surgery to 4 months post-surgery, we can see that all of the injured nerve data falls well below the range of healthy nerve in the contralateral arm, with overall increases of FA in the injured nerve from scan 1 to scan 2, indicating a return to healthy values over time.

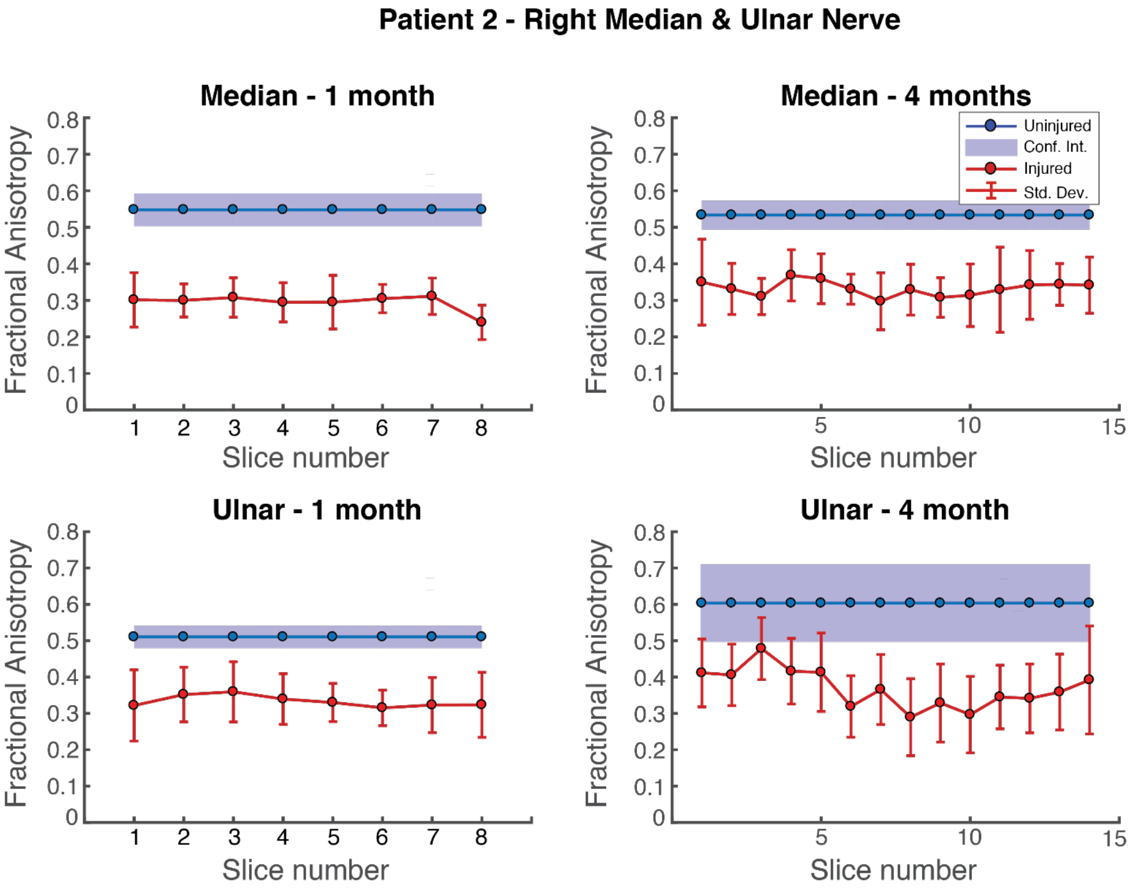

Figure 6-8: Results for TPNI 2: FA plotted by slice. Blue line/dots reflect averaged healthy nerves across all slices; shaded blue areas are the 95% confidence interval for averaged healthy data. Red line/dots reflect individual data points of the injured nerves, with bars showing slice-wise standard deviation. Top charts show measures for median nerve across two timepoints. Likewise, the bottom charts show measures for the ulnar nerve across the same timepoints.

Subject TPNI 3:

Following this trend, a comparison of FA of the left arm, injured ulnar nerve to the right arm, uninjured ulnar nerve showed significant differences over all three timepoints in the third subject, TPNI 3 ($p < 0.001$/$p < 0.001$/$p = 0.028$). Figure 6-9 shows slice-wise measures for FA in the injured and contralateral, healthy ulnar nerve in Subject 3. The reduction of FA values at 6 months related to 3 months were consistent with clinical findings reported in Table 6-1, which indicated an unsuccessful initial repair. Following a secondary repair procedure, FA values overlapped the 95% CI of the contralateral nerve by 9 months (relative to the first procedure), which was once again consistent with clinical findings and is indicative of a successful re-operation.

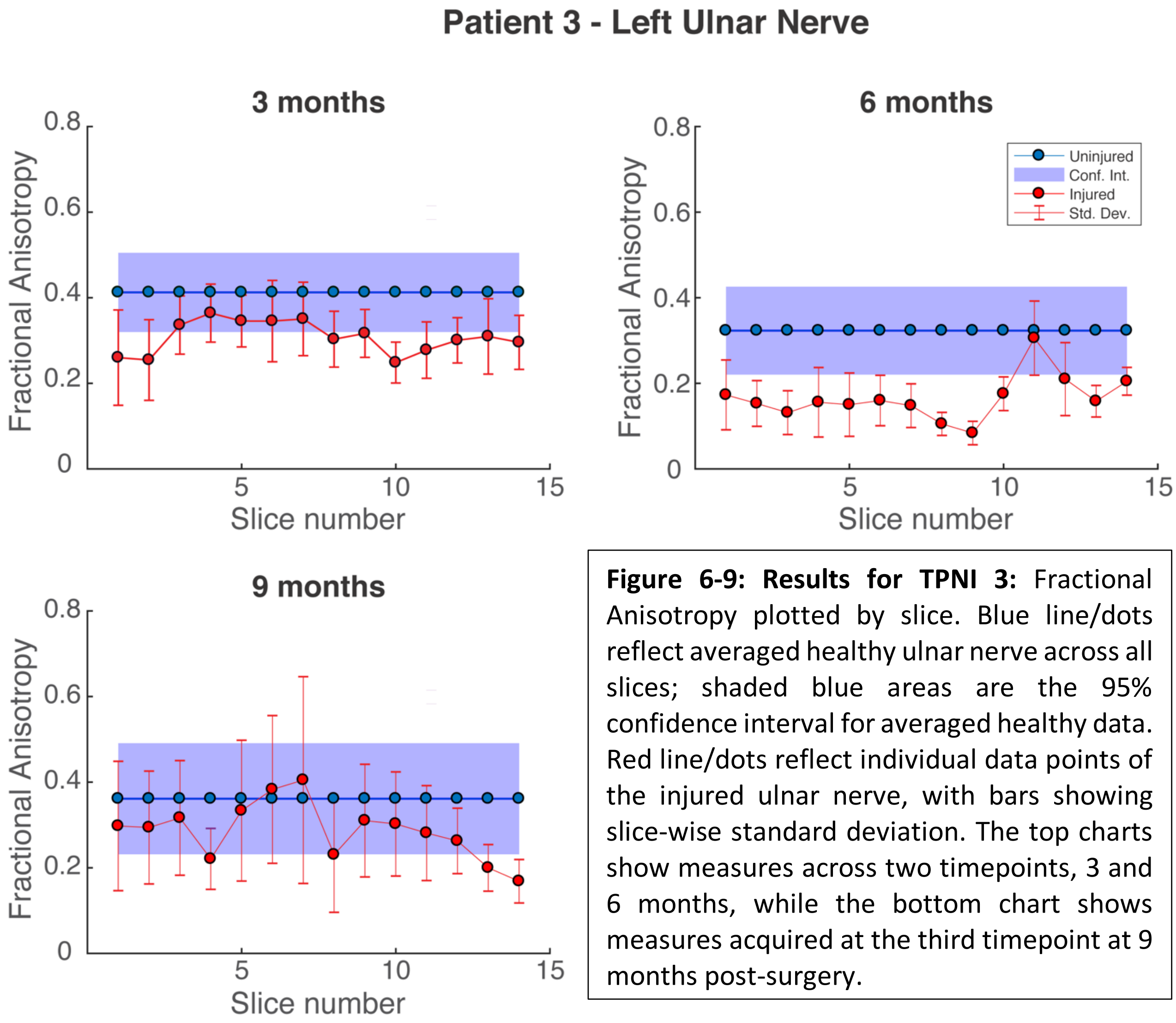

Figure 6-9: Results for TPNI 3: Fractional Anisotropy plotted by slice. Blue line/dots reflect averaged healthy ulnar nerve across all slices; shaded blue areas are the 95% confidence interval for averaged healthy data. Red line/dots reflect individual data points of the injured ulnar nerve, with bars showing slice-wise standard deviation. The top charts show measures across two timepoints, 3 and 6 months, while the bottom chart shows measures acquired at the third timepoint at 9 months post-surgery.

6.5 Discussion

Herein we have demonstrated that DTI is a non-invasive and sensitive measure to traumatic injury and recovery over time. While the clinical measures do reflect the degree of behavioral deficits following TPNI, they are not specific to the degree to injury, which may limit the ability of surgeons to determine when to re-operate. Across all subjects, the observed DTI metrics varied with injury severity (across TPNI and CTS cohorts) and were consistent with changes in clinical measures across time and indicative of nerve regeneration and degeneration over time. More specifically, we found that DTI measures improved after a re-operation procedure (due to no sensorimotor improvement after the first procedure) in one subject (TPNI 3) and after repair-promoting PEG treatment in another patient (TPNI 2). Together, these findings demonstrate the feasibility of performing DTI in the nerves of the wrist after trauma and surgical repair. Furthermore, these measures may provide a noninvasive and reliable assay of regeneration, which may improve clinical decision-making and possibly alter outcomes after surgical interventions.

TPNI 1 suffered a right arm median nerve injury and showed large differences for FA between the injured median nerve compared to the uninjured median nerve of the right arm. These results indicate that DTI can differentiate between injured and uninjured nerves. TPNI 2 suffered a median and ulnar nerve injury at the forearm of the right arm. At the first timepoint, TPNI 2 showed significant differences between both the injured median and ulnar nerves of the right arm when compared to the contralateral uninjured median and ulnar nerves of the left arm. This trend continued three months later at the second timepoint, where significant differences between nerves and arms were observed. For the median nerve, this is likely due to the PEG gel that this subject received at the time of this study. For the ulnar nerve, it was expected recovery would be easier, as this nerve experienced a partial transection (the median nerve was fully transected). As these results indicate, DTI can also show improvement over time. TPNI 3 suffered a left arm, ulnar nerve injury that was captured with longitudinal MRI. At the first timepoint, there is clear delineation between healthy and injured ulnar measures for FA , similar to what was witnessed in the previous two subjects. At the following timepoint, however, mean FA measures decreased over time. This is in agreement with the clinical assessment, which indicated that the initial repair had failed. This subject was returned to the operating room and a secondary re-repair was performed. Three months later, FA values increased above what was observed at the first timepoint, indicating that the re-repair was successful. Our MRI findings showed before re-repair that this subject was not healing. The failure rate on repairs is approximately 40% and being able to identify these failures early, re-operate, and see that the second intervention had benefits to the patient is the ideal application of using DTI to monitor recovery of nerve trauma over time to inform these kinds of operative decisions.

These longitudinal findings also indicate that recovery is not homogeneous between subjects. Considering that these traumatic injuries occur in a variety of ways, and often by mistake, the rate of recovery can be dramatically different between subjects due to a multitude of factors. Factors such as diet, exercise, or in some cases after injury, overexertion during recovery can slow the healing process. Given this heterogeneity, the objective measures provided by DTI may improve clinical decision making by identifying cases that require re-operation earlier than existing methods, although additional data in larger cohorts are required to evaluate this claim.

Observed FA Changes are Driven by RD rather and AD

Upon close inspection of the data, it is apparent that RD is the biggest driver of apparent changes in FA in the TPNI subjects injured nerve data. Studies have shown that RD is reflective of myelin integrity and axon density as it measures diffusion perpendicular to the axon, while AD is reflective of acute axonal degeneration as it measures diffusion along the axon[173,174]. As TPNI subjects experience remyelination and axonal sprouting over time as healing occurs, we might anticipate that differences in RD between injured and healthy nerve would arise, as we observed (p = 0.001), due to the reduced myelination and/or axonal density in recovering nerves. In traumatic peripheral nerve injury, axonal sprouting occurs primarily before secondary remyelination to establish a reconnection from the axon to its target muscle fiber after damaged tissue has been removed via the process of Wallerian degeneration[175]. However, it is difficult to separate axonal regeneration from remyelination using measures of RD alone, and a more myelin-specific measure, like MTR, could allow separating these effects. Previous animal studies have shown that AD is sensitive to axonal regeneration in the first two weeks after injury[85]. Since we imaged the TPNI subjects at the earliest of 1 month post-surgery, it would likely explain why we did not observe any significant differences for AD between injured and contralateral, healthy nerves (p = 0.279), as the axon is present and is connected with target muscle fiber. However, DTI metrics can also be affected by inflammation and edema[176]. In these kinds of injuries, it would be expected to see edema and/or inflammation occur around the injury site that would diminish over time during the healing process. MD will also be altered by edema, or anything that changes AD and/or RD for that matter, and as edema increases MD will also increase[177]. The lingering effects of edema over healing may reflect the observed differences we see for MD in comparing injured and healthy nerves (p = 0.005), however, this may be due to the effect of low RD witnessed in the TPNI cohort. Estimating FA involves all diffusivity measures used for MD, AD, and RD. Because RD has the largest statistical difference between healthy and injured nerves, we can view RD as the main contributor for lower FA in the injured nerves of TPNI subjects.

Comparison to milder injury and healthy controls

The comparison of TPNI, CTS, and healthy subjects showed that DTI was sensitive to the degree of injury across cohorts. Interestingly, this comparison used the data points acquired from all timepoints, which could also be considered as over the time that healing has occurred. In the TPNI cohort, we saw 2 out of the 3 subjects improve over time, indicating that the nerve surgery was successful in regeneration of peripheral nerve. However, in the CTS cohort, we did not observe a significant change of FA over time after CTS release surgery. This may be due to the fact the CTS release surgery is not as invasive, as is the case with TPNI treatment, and the surgery doesn't reconnect detached nerve but rather seeks to relieve painful symptoms by alleviating compression of the nerve. In TPNI surgeries, reconnection of proximal and distal injured nerve are attached together, with some of the damaged tissue removed to promote proper healing. However, in CTS release surgery, only the carpal tunnel ligament is cut, which frees up room around the nerve and causes the compression to be less severe. Additionally, the times we measured CTS subjects may in some cases be after full recovery, as the time course of full recovery for CTS release surgery is typically 4-6 months[178]. This would agree with our observation of the control group showing higher values for FA than CTS, leading to the idea that the median nerve in CTS subjects is not healthy.

Challenges & Limitations

MRI of peripheral nerve has its own unique challenges that set it apart from imaging in the CNS and one of these restraints is a need for high-resolution images. To meet this challenge, we used non-isotropic voxels with a high in-plane (axial) resolution, with thick slices along the nerve. This helps us to visualize the nerve in with sufficient SNR, while also acquiring our imaging in a subject-friendly time course not exceeding 10-15 minutes. Another challenge is the influence of fat which is more present in PNS imaging than CNS imaging. Nerve and fat tissue exhibit different diffusion properties that can cause unwanted artifacts and/or affect our quantification of DTI metrics[179]. In addition, injuries that affect sensorimotor function may result in muscle loss and allow for fat infiltration at the injury site, which further exacerbates this issue. To account for this, we combined three fat suppression methods (SPAIR, gradient reversal, and olefinic saturation) to ensure robust fat suppression.

It is worth mentioning the limitations of the current study for accurate interpretations of the findings. We obtained a small cohort, and as such, chose to look at the data mostly as a case-study per subject. In addition, the affected nerve (median and/or ulnar), injury severity (full/partial transection), and treatment (PEG, reoperation) varied across TPNI subjects, all of which have large impacts on patient outcomes. For these reasons, we expect not only different delays in recovery, but also different presentations in the rate of recovery. To overcome these limitations, we analyzed each TPNI subject individually, comparing results in the injured nerve(s) to the contralateral arm. Finally, the CTS and control groups were not age- and sex-matched, which if done correctly would lead to greater generalizable findings and eliminate the possibility of cofounding variables. Future work will focus on developing study designs that account for these limitations by establishing collaborations with physicians who have a large pool of subjects that could enroll. Also broadening the time of the study may provide additional subjects as traumatic injury and carpal tunnel subjects come to physicians at invariable times. A larger pool of TPNI subjects will also allow us to group by types of injury (full/partial laceration) and by which nerve(s) was damaged (median, ulnar, both).

6.6 Conclusion

DTI is sensitive to injuries in the median and ulnar nerves of the wrist and can be employed in vivo to human subjects for monitoring nerve recovery over time. Across three subjects with traumatic peripheral nerve injuries, this study has shown how DTI can detect abnormalities between injured and healthy nerves, measure the rate at which recovery is happening or not, and measure if re-operation was successful. Additional comparison to carpal tunnel and healthy data show that DTI is sensitive to degree of impairment.

CHAPTER VII

MULTIDIMENSIONAL DIFFUSION OF THE HUMAN SCIATIC NERVE IN VIVO

7.1 Summary

Multi-dimensional diffusion MRI has been developed as a promising new tool to assess tissue microstructure for applications in the brain. In the current study, we adapted this method to the peripheral nervous system on a Philips scanner, specifically, on the sciatic nerve in the thigh of human subjects in vivo. Results showed that measures for microscopic FA (µFA) in thigh were consistent with measures found in white matter of the brain. These scans were also repeatable, as demonstrated with multiple scans per a subset of subjects, and yielded unique information on tissue anisotropy as compared to conventional diffusion tensor imaging of the sciatic nerve.

7.2 Introduction

Diffusion MRI is well-established as a method for investigating white matter microstructure in the human brain[50,55]. A popular method of diffusion MRI in neuroscience and clinical research is DTI. DTI methods work by measuring the diffusion of water molecules in tissue, which can be impeded by the presence of structures such as cell membranes. As a result, DTI is used to derive information that is sensitive to average cell size, shape, orientation, and diffusivity of water molecules, described as a single tensor for a given voxel.

A recent development in diffusion MRI called multi-dimensional diffusion encoding proposes to isolate the different tensors within a voxel[180]. These multi-dimensional diffusion methods, as proposed by Westin et al., provide a higher specificity compared to DTI by preserving the integrity of individual tensors in a voxel, rather than providing the ensemble average where information that exists at the sub-voxel level if often lost[64]. For instance, the "crossing fiber problem" in which two fiber populations are not parallel to each other within a voxel, results in a single tensor that will not accurately reflect the direction of each fiber population (but rather the average direction) when traditional DTI is used. In contrast, multi-dimensional diffusion methods can estimate tensors for each of these populations and differentiate changes in tissue microstructure that result from fiber coherence (e.g., from fiber crossing) from those related to microstructural anisotropy (e.g., from degeneration/regeneration within each fiber population).

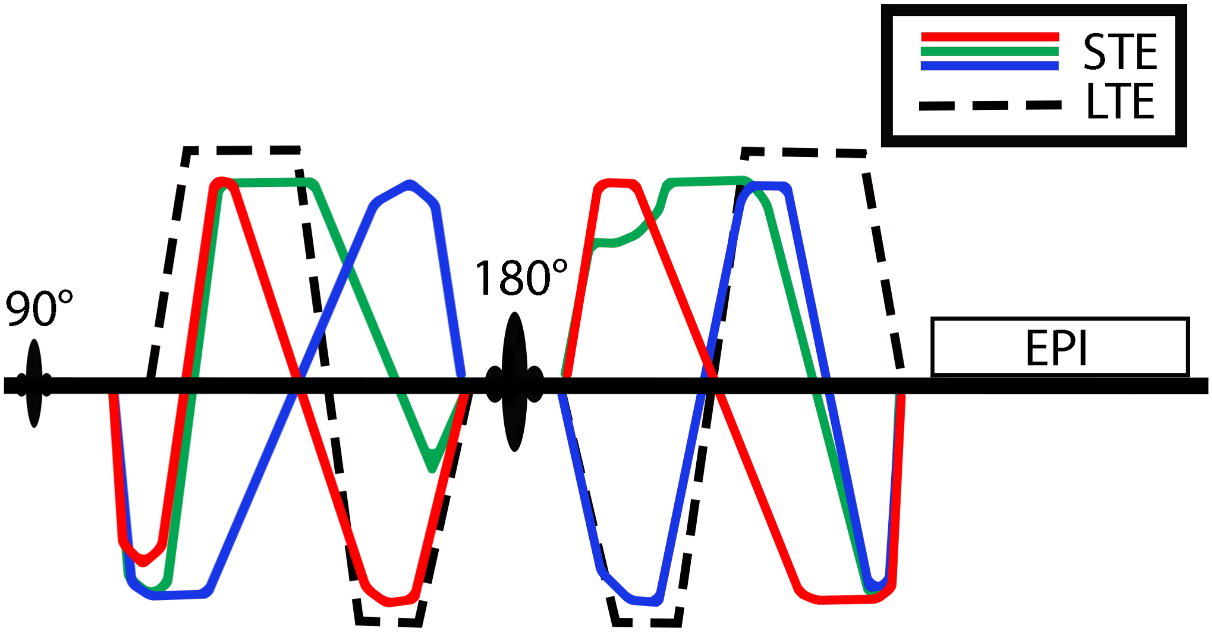

Figure 7-1: Pulse sequence design for multi-dimensional diffusion. Linear tensor encoding (LTE) gradient waveform shown in black dashed line. Spherical tensor encoding (STE) waveforms shown for each gradient in red (Gx), green (Gy), and blue (Gz) lines.

This method uses a pulse sequence that is very similar to Stejskal and Tanner PGSE (Figure 3-3 in Chapter 3), but with some notable exceptions to the diffusion gradient waveforms (Figure 7-1). Instead of only using a standard linear encoding diffusion gradient, where a single diffusion direction is sampled during each acquisition, this method also uses a spherical encoding scan that encodes diffusion along three orthogonal directions equally within a single acquisition. In doing so, this spherical tensor encoding (STE) scheme provides contrast related to the geometric mean across all diffusion directions followed by the arithmetic mean across all fibers/populations (i.e., averaging signal within a voxel). In contrast, the linear tensor encoding (LTE) schemes calculates the arithmetic mean across all fibers/populations (averaging signal within a voxel) and the arithmetic mean across all directions (i.e. powder averaging). Since the geometric mean is not a linear operation, the switch in the order of operations gives us information not available in the linear tensor encoding and the ability to isolate different tensors within a voxel. By combining these two acquisitions, one can estimate metrics that relate to the different sizes, shapes, and orientations of tensors reflecting different sub-voxel tissue compartments.

Specifically, the four main metrics from this method include macroscopic anisotropy (C_M), orientation coherence (C_C), size variance (C_{MD}), and microscopic anisotropy ($C\mu$, or µFA). Macroscopic anisotropy is analogous to FA in DTI, with low measures indicating an isotropic microenvironment ($C_M = 0$), and high measures indicating an anisotropic microenvironment ($C_M = 1$). Orientation coherence takes into account the degree to which anisotropic tensors are either randomly oriented ($C_C = 0$) or coherently oriented ($C_C = 1$). Size variance describes the degree to which, for example, spherical tensors are of equal proportion within tissue, with low measures indicating no variance in size ($C_{MD} = 0$) and high measures indicating varying sizes of spherical tensors in the sample ($C_{MD} = 1$). Microscopic anisotropy describes the relationship between size variance and anisotropy within a sample, with low measures indicating varying sizes of isotropic tensors ($C\mu = 0$) and high scores indicating size invariant anisotropic tensors ($C\mu = 1$). While literature often reports microscopic anisotropy measures as Cµ, we will refer to this metric as µFA in this study[66].

Several models have been introduced to estimate these parameters from STE and LTE acquisitions[181]. In a microenvironment consisting of randomly oriented anisotropic compartments (high µFA), the signal from spherical tensor encoding decreases linearly as b-value increases. However, the signal from the linear tensor encoding decays more slowly at higher b-values (i.e., deviates from a linear decay). In this case , a clear separation is observed between STE an LTE decays that is indicative of microscopic anisotropy. This model will be compared later to results from known high (sciatic nerve) and low anisotropy (muscle surrounding nerve). In an isotropic compartment, we would expect both spherical and linear tensor encoding to have little to no differences in the relationship between signal and b-value.

This newly developed method has been evaluated in the brain [64], yet it's extension to the PNS has yet to be conducted. Given the high specificity of diffusion measurements of multi-dimensional encoding, we propose this method could provide us with novel insights as to neural degeneration and repair after injury of peripheral nerves. Peripheral nerves are structurally similar to white matter, with the exception of higher amounts of collagen and larger axon diameters in the PNS[4]. After an injury occurs, numerous microstructural features that can impact water diffusion (and FA) change concurrently. For example, collagen production greatly surpasses the ideal response, which often hinders the growth of sprouting axons and can impact diffusion measurements such as FA[60]. Because these changes often occur in the presence of Wallerian degeneration and edema, conventional DTI methods may fail to accurately capture the complexity of nerve degeneration and regeneration after injury. This impedes the ability to relate these measures to anatomical and neuropathological changes in the peripheral nervous system. As mentioned previously, multi-dimensional diffusion encoding and the diffusion tensor distribution model offers the ability to discriminate between the sizes, shapes, and orientation of the diffusion environment in living tissue; and the resulting μFA seeks to disentangle the effects of orientation coherence and restricted diffusion[180,182–186]. This sequence and model may provide measurements that can differentiate between myelin and axonal pathologies after surgery and neuropathic degeneration, predicting long-term outcomes. If successful, the adaptation of a multi-dimensional diffusion will be able to provide quantitative values that will allow us to isolate the pathological components of degeneration and regeneration.

This study details the first translation of this method into the human sciatic on a Philips R5.3.0 DDAS system, with results evaluated for repeatability and compared to a conventional sciatic nerve DTI protocol. The steps of implementation, derived results, and interpretation will be described in the remainder of this chapter.

7.3 Methods

Human Subjects and Clinical Information

Six healthy controls volunteered for this study and were scanned lying feet-first and supine. In all subjects the thigh of the right leg was scanned immediately proximal to the knee. Three subjects returned for a repeat scan approximately one week after the first scan to evaluate inter-scan repeatability on the same scanner. All subjects were consented and indicated no signs or symptoms of peripheral neuropathy.

Programming

The pulse sequence for this method was originally developed for Philips systems by Markus Nilsson and upgraded to a Philips Achieva 3T scanner with R 5.3.1 software package by Dr. Guillaume Gilbert (Philips Healthcare; Markam, ON, Canada). The scanners used at Vanderbilt University were Philips Achieva 3T scanners with a previous release of the software, R 5.3.0. As such a “down-porting” of the pulse sequence code was initiated to complete this project. Dr. Gilbert sent us the scanner patch that was created and tested for the use in the brain. This patch was integrated into the Philips virtual machine that is housed at VUIIS, and the process was initiated to program this patch to the previous software version. The differences between releases were minimal, with additional features existing in the R 5.3.1 version that had no impact of the parameters needed to implement the multidimensional diffusion method. This programming was conducted manually in the Philips Virtual Machine environment, and later successfully applied to the scanner for testing.

Implementation

The first step towards validating this method on our scanner was to test our patch in the human brain and compare results to published values. A healthy volunteer was scanned twice, and while these findings are not reported in this manuscript, values for white matter (specifically, in the corpus collosum: µFA = 0.98) agree with the available literature (Westin et al.: µFA = 0.99), suggesting the methods were correctly implemented on our system[64].

Based on these positive initial results in the brain, we translated the method from the brain to the sciatic nerve of the leg. The previously designed spherical tensor encoding scheme for the brain had a max b-value of 2000 and a minimum TE of 160 milliseconds[64]. However, this scheme would result in only 2 percent of the remaining signal in the nerve (assuming T_2 = 40ms), so additional modifications to the protocol were required. In addition, PNS axon diameters are much larger than in the CNS[187], allowing us to achieve similar diffusion weightings at lower b-values in our sciatic nerve scheme.

With this in mind, we designed a spherical tensor encoding scheme optimized specifically for the nerves that had a lower b-value (1300 s/mm^2)[188]. Additional design parameters included a max gradient amplitude = 75 mT/m, max slew rate = 90 mT/m/s, and heat dissipation factor = 0.7. Together, this resulted in the spherical encoding gradients (waveform shown in Figure 7-2) and a minimum TE = 85 ms, boosting our acquired signal to 13% of the signal remaining in the nerve (over six times as much from the previous brain protocol). It is worth noting that the spherical tensor encoding was our main challenge in reducing TE while achieving a high b-value. The linear tensor encoding sequence wasn’t as demanding on the gradient amplifiers, and the TE for this acquisition was simply reduced to match the spherical encoding scheme.

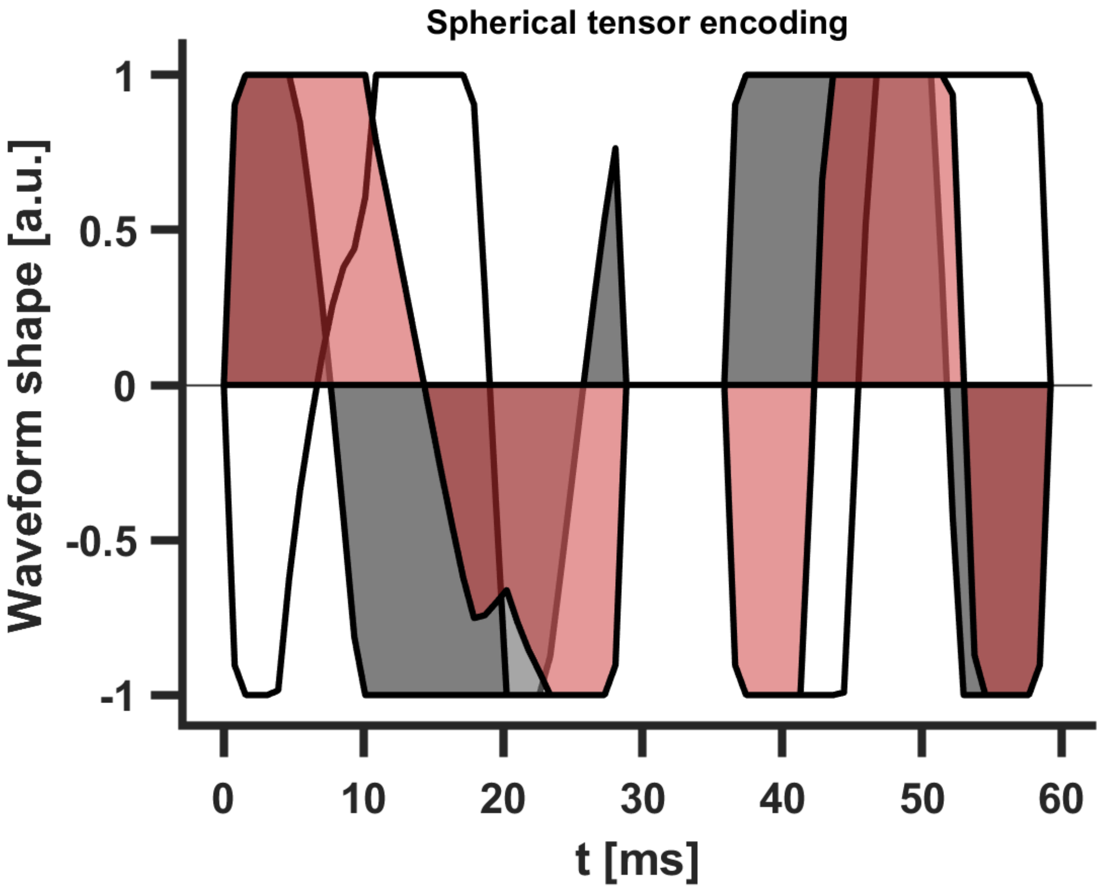

Figure 7-2: Spherical Tensor encoding waveform. Tailored gradient waveforms (Gx - red, Gy - gray, Gz - white) applied to the human sciatic nerve for the multi-dimensional diffusion method. *t* represents time. A.u. represents arbitrary units for maximum gradient amplification.

MRI Data Acquisition

Subjects were scanned with a 3.0 T Philips Achieva MR scanner using a 16 channel knee coil for RF reception. The multi-dimensional diffusion protocol for spherical and linear tensor encoding included: combined SPAIR and gradient reversal fat suppression, max b-value = 1300 s/mm^2, 45 diffusion-encoding directions, TR/TE = 4500/85 ms, resolution = 1.5 x 1.5 x 10 mm^3, NSA = 1, scan time = 5 minutes for LTE or STE scans (10 minutes total). Recall, Figure 7-2 shows the gradient waveform for the spherical tensor encoding scan that was applied to the sciatic nerve. The gradient waveform for the linear tensor encoding was similar to the one shown in Figure 7-1.

Note the average diffusion time of the spherical tensor encoding scan was designed to approximately match the diffusion time of the linear tensor encoding scan to minimize the impact of diffusion time effects on our results. Table 7-1 shows the difference between the brain protocol we received from Dr. Gilbert and the sciatic nerve protocol developed for this study. The conventional diffusion protocol included: combined SPAIR and gradient reversal fat suppression, max b-value = 900 s/mm^2, 16 diffusion-encoding directions, TR/TE = 4000/62 ms, Resolution = 1.5 x 1.5 x 9.6 mm^3, NSA = 6, scan time = 10 minutes.

	Lasič Brain Protocol[186]:	**Sciatic Nerve Protocol:**
Scanner:	Philips 3.0 Tesla Achieva	Philips 3.0 Tesla Achieva
Coil:	Head (32 ch)	Knee (16 ch)
TR/TE (ms):	6000/160	4500/85
B-values (s/mm^2):	50/250/500/1000/2000	0/100/500/900/1300
Diffusion-encoding Directions:	6-30 per b	45 total
Field of View	288 x 288 x 60 mm^3	160 x 160 x 80 mm^3
Resolution:	3 x 3 x 3 mm^3	1.5 x 1.5 x 10 mm^3
Scan Time:	10 minutes	10 minutes

Table 7-1: Scan parameters for brain and sciatic nerve. Brain protocol adapted from Lasič et al., 2014 (left) and resulting sciatic nerve protocol from this study (right).

MRI Data Analysis

The multi-dimensional diffusion data for spherical and linear encoded scans were processed with the Matlab code for multi-dimensional diffusion MRI, provided by Markus Nilsson[189]. This processing pipeline yields estimates of µFA from LTE and STE signals via the diffusional variance decomposition (DIVIDE) model[66]. The conventional diffusion data was processed via Camino for DTI-based parameter maps and FA. In both sequences, regions of interest (ROIs) were manually selected using Matlab on all slices for the sciatic nerve and mean (and standard deviation) slice-wise values were estimated for µFA and FA. In addition, ROIs were selected in surrounding skeletal muscle for comparison to previously established microenvironment models.

Statistical Analysis

A paired t-test analysis was performed to compare the conventional FA measures to the µFA measures. Additionally, coefficient of variation was estimated across scans for measures of µFA to estimate inter-scan repeatability of this method.

7.4 Results

Representative maps for T_1-weighted, multidimensional diffusion methods, and conventional DTI of the proximal thigh are shown in Figure 7-3. Overall, conventional FA were consistent with published values in sciatic nerve[190]. Measures for µFA were also consistent with values of white matter in the brain[183].

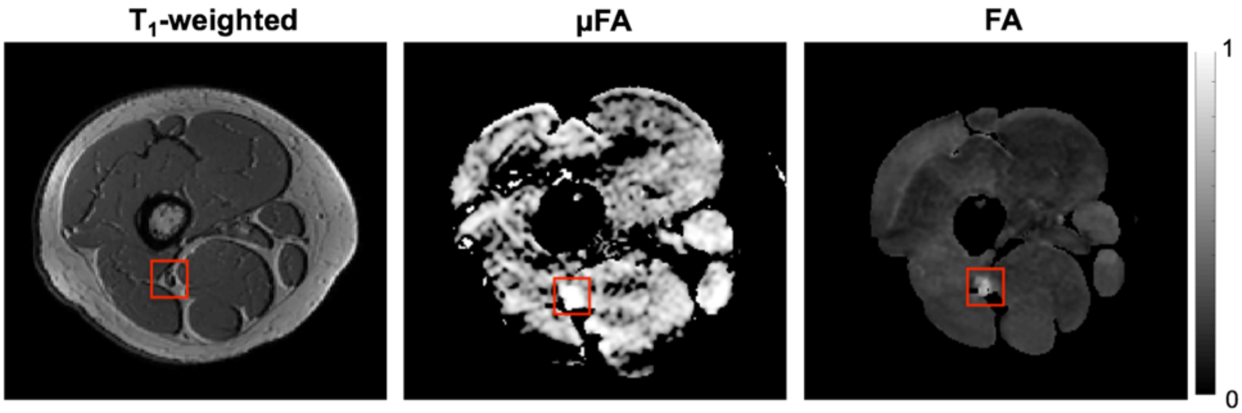

Figure 7-3: T_1-weighted, µFA, and FA maps shown for proximal thigh in a representative subject. µFA and FA images have a mask applied that removed signal from skin and adipose tissue from the resulting image in processing. Colorbar on right represents data on µFA and FA image. The red box indicated the location of the sciatic nerve within muscle. Note the values in the red box on the µFA map are visually more homogeneous than in the FA image.

Group measures for FA under the conventional DTI protocol were lower (FA ± SD = 0.536 ± 0.083) than µFA of the multidimensional diffusion protocol (µFA ± SD = 0.947 ± 0.143). Paired t-test results showed that µFA was significantly higher than conventional FA ($p < 0.001$). Results for all subjects and scans are reported on Table 7-2.

	FA	**± SD**	**µFA (Scan 1)**	**± SD (Scan 1)**	**µFA (Scan 2)**	**± SD (Scan 2)**
Subject 1	0.570	0.051	0.943	0.185	0.960	0.118
Subject 2	0.568	0.085	0.954	0.121	0.938	0.102
Subject 3	0.620	0.107	0.942	0.158	1.022	0.094
Subject 4	0.456	0.074	0.885	0.131		
Subject 5	0.471	0.059	0.940	0.132		
Subject 6	0.533	0.123	1.020	0.129		
Group:	*0.536*	*0.083*	*0.947*	*0.143*	*0.973*	*0.105*

Table 7-2: Results from ROIs include mean of diffusion measures for all slices. Metrics shown for conventional DTI scheme (FA ± SD) and multidimensional diffusion scheme (µFA ± SD) for when scan 1 and scan 2 where available in subjects. Blank spaces indicate subjects who did not return for a rescan.

For the three subjects who returned for a rescan a week later, group measures for µFA were similar between the first scan (µFA ± SD = 0.947 ± 0.068) and second scan (µFA ± SD = 0.973 ± 0.033). Coefficient of variation analysis between scan 1 and scan 2 subjects resulted in 3.7%, indicating low differences between the measures gained between timepoints. Measures for µFA in the sciatic nerve between scan 1 and 2 are shown for each subject who returned for a second scan to assess rescan producibility (Figures 7-4, 7-5, 7-6). These plots further illustrate that measurements were similar across longitudinal scans.

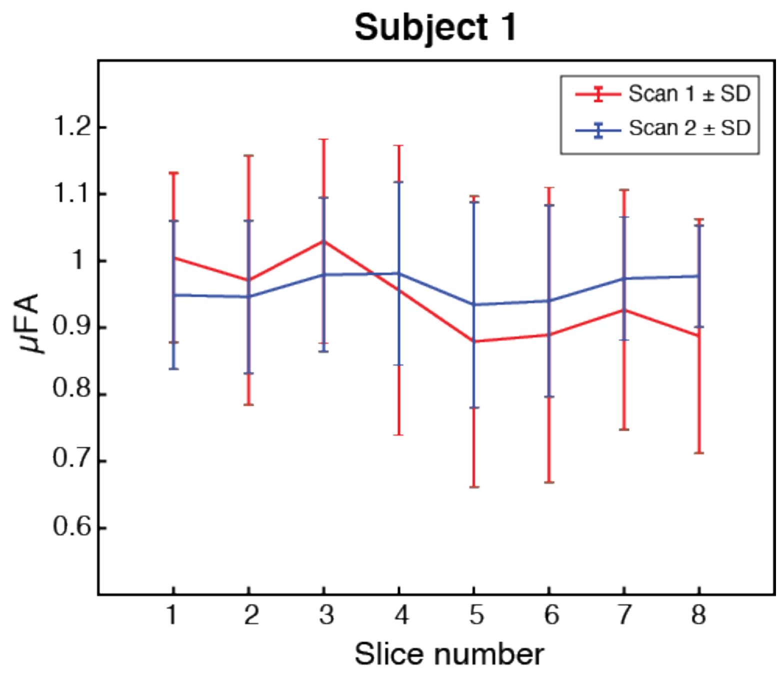

Figure 7-4: Scan-Rescan results from Subject 1. Microscopic fractional anisotropy (µFA) shown for Subject 1. Data include slice measurements from scan 1 and scan 2 a week later. Error bars indicate standard deviation (SD) of measures. Mean ± SD for each scan: Scan 1 µFA = 0.94 ± 0.19; Scan 2 µFA = 0.96 ± 0.12.

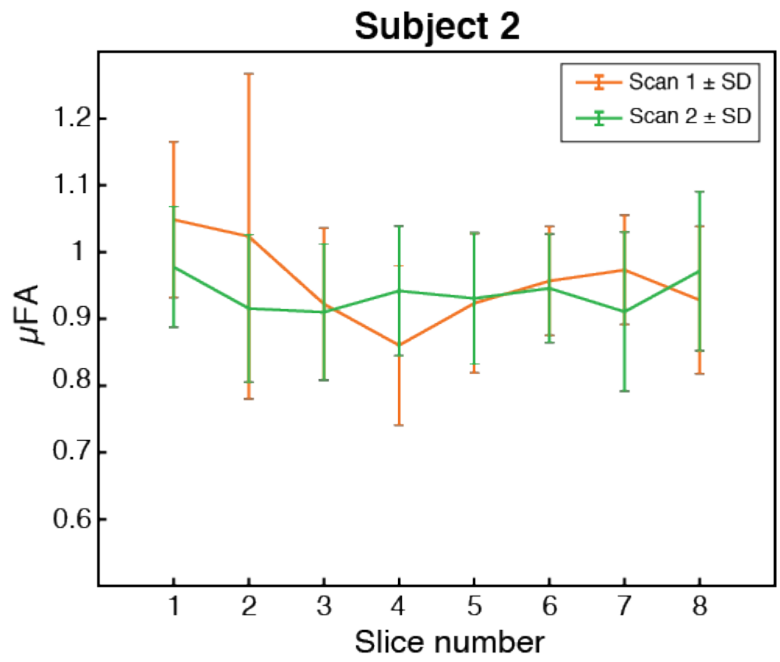

Figure 7-5: Scan-Rescan results from Subject 2. Microscopic fractional anisotropy (μFA) shown for Subject 1. Data include slice measurements from scan 1 and scan 2 a week later. Error bars indicate standard deviation (SD) of measures. Mean ± SD for each scan: Scan 1 μFA = 0.95 ± 0.12; Scan 2 μFA = 0.94 ± 0.10.

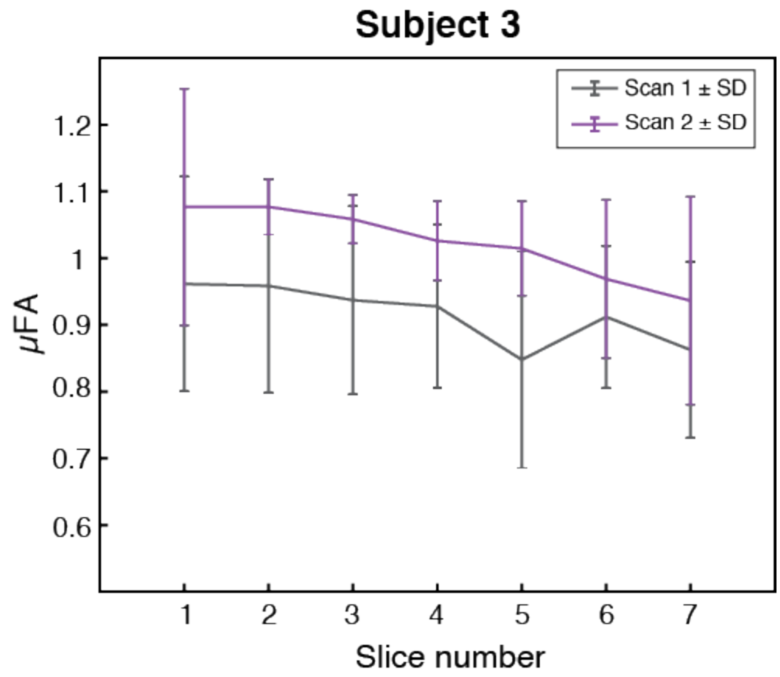

Figure 7-6: Scan-Rescan results from Subject 3. Microscopic fractional anisotropy (μFA) shown for Subject 1. Data include slice measurements from scan 1 and scan 2 a week later. Error bars indicate standard deviation (SD) of measures. Mean ± SD for each scan: Scan 1 μFA = 0.94 ± 0.16; Scan 2 μFA = 1.02 ± 0.09.

An ROI analysis was conducted to determine the sensitivity of this technique to structures with different levels of anisotropy (nerve and muscle). Figure 7-7 shows nerve ROI (A.) and muscle ROI (B.) in the same slice. For nerve signal, there is a clear separation between STE and LTE, indicating increased µFA. In contrast, there is little to no separation between these encoding schemes for the muscle signal, indicating low µFA and lower anisotropy for the compartments present in muscle tissue. These findings are consistent with previously introduced microstructural tissue models[181].

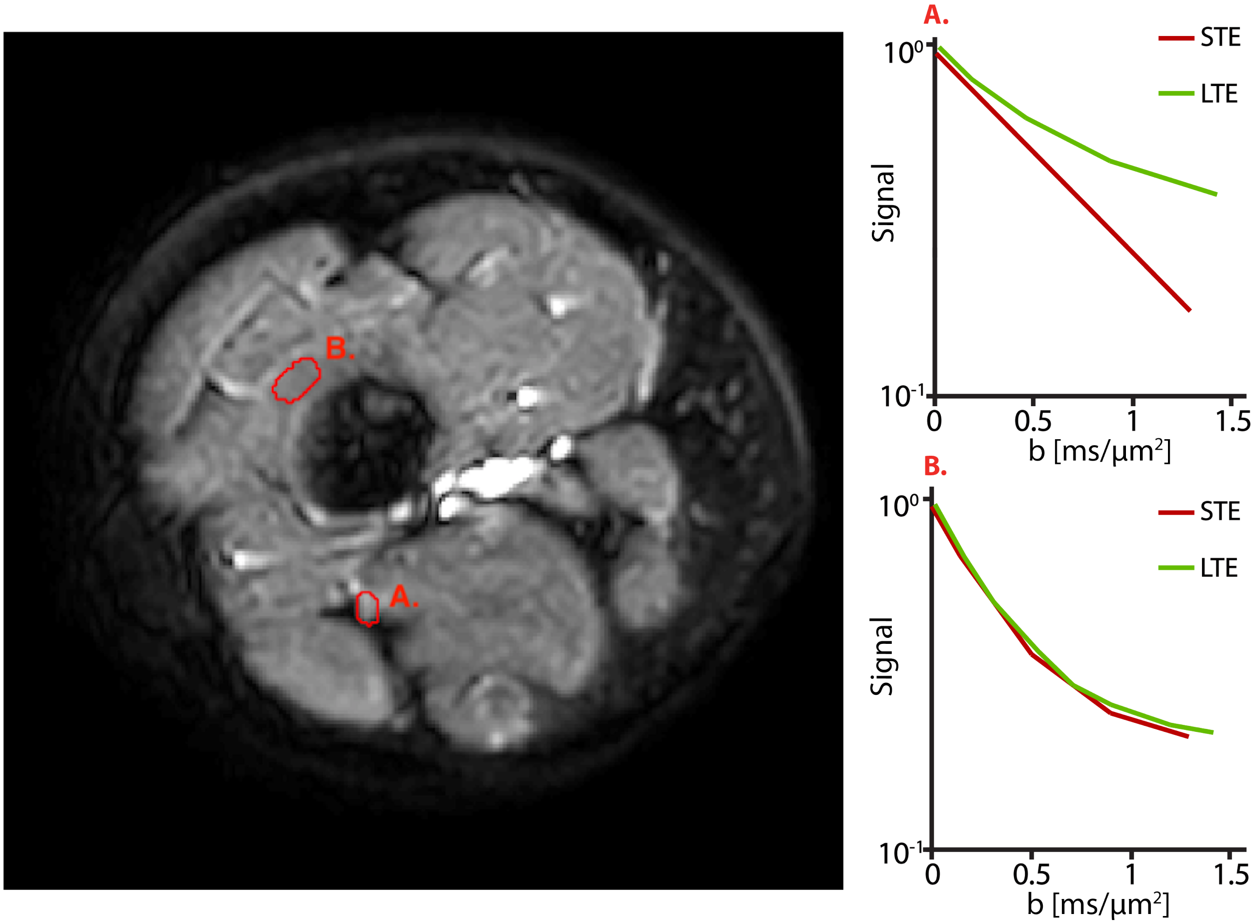

Figure 7-7: Signal versus b-value plots for nerve and muscle. Notice the clear separation between LTE and STE for the nerve ROI (A.), indicating higher degree of microscopic anisotropy. There is no separation of lines for LTE and STE for the muscle ROI (B.), indicating very little microscopic anisotropy.

7.5 Discussion

In this study, we successfully developed a multi-dimensional diffusion protocol for the human sciatic nerve in vivo that overcomes the technical challenges of PNS imaging. The resulting protocol was clinically feasible (with regards to scan time and available hardware), consistent with findings in white matter, reliable across healthy subjects, and repeatable across longitudinal scans. In addition to this, our implementation of this method showed distinct differences between tissues (i.e., muscle and sciatic nerve). This application had its own set of technical challenges, and while some were unique to this study, there were many that are very common among applying brain techniques to the peripheral nerves of the body.

Technical challenges of PNS imaging

Aside from the competing needs for high b-values and low TE values that was considered in the Methods section of this chapter, there were other demands that were considered when tailoring this method to applications in human nerves. For example, the need for high resolution and reduced scan time were of critical importance, as high resolution images are required to study the small structure of nerves, and a short scan time is required for clinical applications. It is for these reasons that we chose to sacrifice resolution along the nerve (i.e., 10mm slice selection) and used high in-plane resolution with non-isotropic voxels, which allowed us to visualize the nerve while also providing sufficient SNR to estimate model parameters.

Another notable technical challenge was the influence of fat in proximal thigh. In most people, the thigh houses the highest percentage of body fat, and in imaging acquisitions, the presence of fat can affect quantification of model parameters. This is because fat and nerve tissue have different diffusion properties. This may be of more problematic when applying to neuropathic patients, as muscle atrophy occurs and fat replacement follows. For the purposes of this study, we employed multiple fat suppression techniques to alleviate any concern of fat influencing our results of FA and µFA respectively. Specifically, this involved the combination of SPAIR and gradient fat reversal (as described in Section 3.2.3 in Chapter 3) on the Philips scanner.

Application to disease and injury

This successful adaptation of the multi-dimensional diffusion sequence may be able to provide quantitative values that will allow us to isolate the various pathologies present during degeneration and regeneration. Specifically, this method may produce sub-voxel anisotropy that are more specific to myelin composition and/or axonal integrity of nerves in the human peripheral nervous system. By providing more information on the micro-environment of diffusion tensors within a given voxel, this additional information may improve interpretations of the various pathologies involved during nerve degeneration, injury, and repair of the peripheral nerves.

In the case of wrist nerve injury, the diffusion of water molecules is often hindered by the effects of inflammation, edema, and collagen production that occurs at the site of injury, resulting in poor motor and sensory functioning of the nerve[191]. By calculating size variance and orientation coherence of axons, we may be able to have a better idea of how the effects of inflammation may be impacts both systems independently. This technique may also be able to quantify the degree to which these effects of injury and recovery have on the microtissue environment during the process of healing. With enough subjects and longitudinal timepoints of

MRI scans, it may be possible to create a model of how the effects of edema, inflammation, and collagen production occur after injury occurs and surgery is conducted. This information would provide novel insight into this aspect of peripheral nerve recovery.

Applications of this technique can benefit HNPP and other inherited neuropathy populations by being able to classify the degree to which nerve degeneration has occurred. Most beneficial to this disease would be determining if the multi-dimensional diffusion encoding method and model can isolate the biological components in length-dependent axonal loss and demyelination. In the case of inherited neuropathies, diffusion measurements can change as a result of degenerating nerves[82]. Since HNPP is a life-long illness that is characterized by a slowly progressive nature of the disease, being able to probe the biological mechanisms of degeneration could provide us with a way to monitor disease progression and treatment response in future clinical trials. If successful, this diffusion method may also be added to the current HNPP protocol with MTR and Dixon sequences to achieve a more comprehensive picture of how this disease affects the peripheral nerves in the leg. Further applications of this technique could be applied to the central nervous system (e.g., brain, spinal cord), and other clinical PNS populations such as diabetic neuropathy, Charcot-Marie-Tooth disease, motor neuropathies, and cases of nerve compression such as carpal tunnel syndrome.

Limitations

Limitations of this study include its inherent small study size, which was used mainly to determine feasibility. However, larger sample size comparing healthy and diseased/injured sciatic nerve would allow us to separate to test the ability of the method to isolate axonal pathology and demyelination, which was not done in this current study. Another possible limitation comes when utilizing two diffusion encoding sequences. It is important that diffusion times for STE and LTE scans are the same. In this study, we matched the average diffusion time of the STE scan (which does not have a single diffusion time) with that of the LTE scan. However, this may also be a limitation of the study, and further work is required to estimate the impact of diffusion times on the results herein. Additionally, while we only compared μFA to FA in this study, future work would focus on including comparisons to other advanced diffusion methods, such as Diffusion Kurtosis Imaging (DKI), Spherical Means Technique (SMT), Neurite Orientation and Dispersion Density Imaging (NODDI)[192–194]. The subject of future work will focus on other parameters of this method than μFA, including size variance (C_{MD}) and orientation coherence (C_C), in patients where these other metrics may be beneficial. Future studies will also focus on the possibility of SNR bias to explain our results of microscopic anisotropy, which in some cases was higher than 1.

7.6 Conclusion

Multidimensional diffusion in the sciatic nerve is feasible with Philips R5.3.0 DDAS system. Future directions of this research will focus on better fat suppression techniques, optimization of b-values and number of diffusion directions, better masking/post-processing techniques, coil selection for larger coverage of the leg, and applying this method towards patients with lower extremity neuropathy.

CHAPTER VIII

CONCLUSIONS

8.1 Limitations of studies

All studies in this project have limitations that should be considered when interpreting the measures we derive from MRI. In the case of HNPP, it is a rare genetic disease and because of this our sample size was small. This is not to say the study was underpowered, but led to the implementation of non-parametric statistical approaches (i.e., Wilcoxon signed-rank test). Had we achieved a larger sample, we could have seen the HNPP group's measures show a Gaussian distribution, which would have allowed for parametric statistical approaches (i.e., paired t-test). This is not to say that there are issues reporting non-parametric statistical results, but in general, reporting measures from a large group size would be better to generalize to the general population. This challenge was not unique to the study on HNPP patients, but also was present in the upper extremity study as well.

A notable limitation of the upper extremity studies are the motivations of the patients to participate in research studies. In inherited diseases like HNPP, and others outside the scope of this project like dementia, research participants tend to have a more altruistic approach to donating their time for scientific research. I have heard first hand from these patients that they wish not to give their ailment to their children or grandchildren, and by helping scientific research, they may be able to contribute in some way to the future treatment their family may have to endure. In the case of upper extremity injuries that are detailed in this dissertation, these situations are caused by pure accident, and treatment is seen as a way to get back to normal life. Thus, the injuries are perceived as a temporary problem and not a lifelong condition such as in inherited diseases. However, the importance of this work is to illustrate that these injuries can have lifelong consequences and the time of treatment is critical to determine that outcome. The same mindset can be applied to the cases of upper extremity compression, where patients see their ailment in the carpal tunnel as a lifelong problem that will need to be monitored, but also see the carpal tunnel release surgery as a quick fix to their symptoms of pain. These motivations heavily impacted our subject recruitment and retention over the longitudinal time courses that these studies had. A measure we took to improve recruitment was an increase in subject payment for each scan, but this had minimal effects on retention.

Another important limitation of the upper extremity study is that we only looked at patients post-operatively. Pre-operative images for the TPNI group were not possible, as these subjects did not know when and how they would suffer a traumatic injury. However, the carpal tunnel patients received diagnostic testing that confirmed the occurrence of CTS prior to surgery and, had this study been more considerate, could have acquired DTI maps of the median nerve in the carpal tunnel before and after surgery. For the sake of explaining the TPNI and CTS patients in the same context, post-operative images sufficed for the interpretation of DTI metrics across varying degrees of injury and recovery over time.

8.2 Challenges of applications to PNS

One of the major challenged of applying MR methods to the PNS is the need for high resolution. Many of the MR techniques we used were initially developed for the brain, which is much larger than the peripheral nerves we are interested in. In this dissertation we imaged the sciatic and tibial nerves of the leg and the median and ulnar nerves of the arm. Sciatic nerve is the largest nerve in the body with a diameter in thigh of approximately 5 mm[101], and the tibial nerve diameter at the ankle is approximately 4 mm[195]. At the forearm near the wrist, the median nerve is approximately 3 mm[196], and the ulnar nerve at approximately 2.5 mm[154]. In comparison, the brain of a typically developed adult is 180 mm from the forehead to the back of the head. As we travel along the nerve of the leg, for example, we would see the proximal sciatic nerve as relatively large, and as we move more distal we would see this nerve bifurcate into the tibial and common peroneal nerves. The same narrowing can be observed for nerves in the arm as well. We also see these nerves becoming smaller as we move more distally towards the finger or the toes. Because of these anatomical features, our MRI methods are inherently limited by the area at which we choose to measure and how the size of the nerve at that location have affect our measurements or alter the parameters we choose as conditions for these measures. The solution we found to overcome this challenge was to implement non-isotropic voxel acquisition with high in-plane resolution in the axial plane, while sacrificing resolution along the nerve. For the multidimensional diffusion application, we also implemented powder averaging over all signals in acquisition to increase relative SNR.

Another challenge is the MR properties of nerve and designing an experiment that will give accurate results. Recall, the T_2-relaxation of nerve is much shorter than white matter in the brain due to the effects of collagen and connective tissue in the nerves. As such, applying previously designed brain MR method to the PNS will require a shorter TE, which may impose hardware limitations depending on the sophistication and power of the sequence. However, the axon diameters in peripheral nerve are much larger than the brain, and lower b-values are feasible to accurately measure the peripheral nerves and would alleviate some of the hardware limitations. This was especially a concern in the multidimensional diffusion implementation as it was a very costly sequence on the scanner hardware.

The influence of fat is another crucial consideration when applying MR methods to studying the PNS. In the studies of this dissertation, implementation of fat suppression techniques was crucial in achieving accurate results. A common feature of the PNS is the presence of fat and muscle surrounding the nerve. As muscle wastes in cases of neuropathy, fat infiltrates and replaces the areas where atrophy has occurred. However, nerve and fat exhibit different diffusion properties, and a residual fat signal left unchecked could cause artifacts that affect our quantification. Specifically, the chemical shift of fat signal could overlay onto the reconstructed image of the nerve and cause erroneous measures that do not accurately reflect nerve health.

Scan time and patient placement are very important in assessing nerve health across neuropathy and injury. Specifically in the case of a pressure palsy like HNPP, use of the Philips anterior coil may feel heavy on the legs of some patients and would cause discomfort over time. This is why scan time should be limited to as short as possible, as this discomfort may cause patients to readjust mid-scan and obscure images that require the patient to lie very still. This becomes an even higher demand when implementing a multi-parametric approach where multiple scans are needed. In the case of upper extremity nerve injury and compression, these demands are also present to provide the most comfortable environment for scanning. The Philips wrist coil, while large enough for typical studies, has the potential to be tight on patients who have sensitive injuries, and in one case we had to move to the anterior coil for scanning the wrist so as to cause the least amount of discomfort to the subject.

Finally, post-processing of peripheral nerve MR data should be closely monitored. For instance, many available software packages for diffusion processing have some assumptions built in that may not be apparent to the naïve scientist. As such, some of these assumptions are geared towards brain research paradigms and it is very possible that a software package was validated based off the anatomy it is meant to be used on. For this consideration, I advise manual calculations of all parameters from acquisition to output measure.

8.3 Future Directions

Each of these studies is a first step in establishing a quantitative protocol to studying nerve health, and future improvements could dramatically affect the importance of these preliminary studies. For the HNPP study, a bigger cohort would strengthen these results by applying our imaging protocol to a larger research site for this patient population, such as Wayne State which has the largest CMT clinic in the nation. A wider cohort group may also help us tease out and explain why MTR was not significantly different between the thigh and ankle of patients but was for controls. Inter-site implementation may also show why Dixon imaging came out as significant, as more subjects with varying disease states may allow for an interpretation of muscle atrophy and fat innervation in these inherited neuropathies. Additionally, a whole leg sequence would be beneficial to capture the length-dependent changes as they occur along the course of the leg, as well as save scan time where the subject must be repositioned and have the same scans run a second time on the ankle.

In the wrist nerve studies, future directions could include applying this imaging protocol to CTS patients prior to surgery to look at how diffusion metrics change over the course of carpal tunnel release surgery. For both the TPNI and CTS subjects, implementing the multidimensional diffusion scan could yield results that relate better to the degree of axonal disorientation and degree of compression along the injury site. In our wrist studies, it is important to note the differences between proximal uninjured nerve and distal injured nerve. This, however, has its limitations as our imaging protocols are designed only to probe nerves of a certain size. Thus, if imaging challenges for capturing smaller nerves, such as the radial nerve and digital nerves in the hand, then we could have a better understanding of how these injuries affect distal areas which may lead to better patient attitudes and outcomes.

Future extension of the work done on multidimensional diffusion could include scanning other peripheral nerves of the body, such as in the arms or the branches of the brachial plexus. Like previously mentioned, this method could also benefit patient populations by supplying researchers with information on nerve orientation and coherence that was unattainable by other methods, and could have a positive impact on patient outcomes. Optimization of the sequence could also be achieved, but for the sake of the study herein, we wanted to see simply if it was feasible to translate to the leg from the brain. Investigation of the assumptions of the model may also improve the relatability of these measures.

REFERENCES

1. Catala, M. & Kubis, N. *Gross anatomy and development of the peripheral nervous system*. *Handbook of Clinical Neurology* **115**, (Elsevier B.V., 2013).
2. Sternini, C. Organization of the peripheral nervous system: Autonomic and sensory ganglia. *J. Investig. Dermatology Symp. Proc.* **2**, 1–7 (1997).
3. Griffin, J. W. & Thompson, W. J. Biology and Pathology of Nonmyelinating Schwann Cells. **1531**, 1518–1531 (2008).
4. Koopmans, G., Hasse, B. & Sinis, N. *The Role of Collagen in Peripheral Nerve Repair*. *International Review of Neurobiology* **87**, (Elsevier Inc., 2009).
5. Topp, K. S. & Boyd, B. S. Structure and biomechanics of peripheral nerves: Nerve responses to physical stresses and implications for physical therapist practice. *Phys. Ther.* **86**, 92–109 (2006).
6. Chernousov, M. A. *et al.* Glypican-1 and α4(V) collagen are required for Schwann cell myelination. *J. Neurosci.* **26**, 508–517 (2006).
7. Moya, F., Bunge, M. B. & Bunge, R. P. Schwann cells proliferate but fail to differentiate in defined medium. *Proc. Natl. Acad. Sci. U. S. A.* **77**, 6902–6906 (1980).
8. Burnett, M. G. & Zager, E. L. Pathophysiology of peripheral nerve injury: a brief review. *Neurosurg. Focus* **16**, 1–7 (2004).
9. Sunderland, S. The anatomy and physiology of nerve injury. *Muscle Nerve* **13**, 771–784 (1990).
10. Kerns, J. M. The microstructure of peripheral nerves. *Tech. Reg. Anesth. Pain Manag.* **12**,

127–133 (2008).

11. Lee, S. K. & Wolfe, S. W. Peripheral nerve injury and repair. *J. Am. Acad. Orthop. Surg.* **8**, 243–252 (2000).

12. Seddon, H. Three types of nerve injury. *Brain* **6**, 237–88 (1943).

13. Chen, Y., Haacke, E. M. & Li, J. Peripheral nerve magnetic resonance imaging. *F1000Research* **8**, 1803 (2019).

14. Sunderland, S. A classification of peripheral nerve injuries producing loss of function. *Brain* **74**, 491–516 (1951).

15. Sunderland, S. *Nerves and nerve injuries*. (E & S Livingstone Ltd., 1968).

16. Bromberg, M. B. An Electrodiagnostic Approach to the Evaluation of Peripheral Neuropathies. *Phys. Med. Rehabil. Clin. N. Am.* **24**, 153–168 (2013).

17. Lee, D. H., Claussen, G. C. & Oh, S. Clinical nerve conduction and needle electromyography studies. *J. Am. Acad. Orthop. Surg.* **12**, 276–287 (2004).

18. Mills, K. R. The basics of electromyography. *Neurol. Pract.* **76**, 32–35 (2005).

19. Levine, T. D. & Saperstein, D. S. Routine use of punch biopsy to diagnose small fiber neuropathy in fibromyalgia patients. *Clin. Rheumatol.* **34**, 413–417 (2015).

20. Bevilacqua, N. J., Rogers, L. C., Malik, R. A. & Armstrong, D. G. Technique of the Sural Nerve Biopsy. *J. Foot Ankle Surg.* **46**, 139–142 (2007).

21. Chung, K. C., Hamill, J. B., Walters, M. R. & Hayward, R. A. The Michigan hand outcomes questionnaire (MHQ): Assessment of responsiveness to clinical change. *Annals of Plastic Surgery* **42**, 619–622 (1999).

22. Shauver, M. J. & Chung, K. C. The Michigan Hand Outcomes Questionnaire after 15 years

of field trial. *Plast. Reconstr. Surg.* **131**, 779–787 (2013).

23. Chung, B. T. & Morris, S. F. Reliability and internal validity of the Michigan hand questionnaire. *Ann. Plast. Surg.* **73**, 385–389 (2014).

24. Härkönen, R., Harju, R. & Alaranta, H. Accuracy of the Jamar Dynamometer. *J. Hand Ther.* **6**, 259–262 (1993).

25. Mathiowetz, V., Weber, K., Volland, G. & Kashman, N. Reliability and validity of grip and pinch strength evaluations. *J. Hand Surg. Am.* **9**, 222–226 (1984).

26. Villafañe, J. H. *et al.* Reliability of the handgrip strength test in elderly subjects with parkinson disease. *Hand* **11**, 54–58 (2016).

27. Härkönen, R., Piirtomaa, M. & Alaranta, H. Grip strength and hand position of the dynamometer in 204 finnish adults. *J. Hand Surg. Am.* **18**, 129–132 (1993).

28. Czell, D. *et al.* Nine Hole Peg Test and Transcranial Magnetic Stimulation: Useful to Evaluate Dexterity of the Hand and Disease Progression in Amyotrophic Lateral Sclerosis. *Neurol. Res. Int.* **2019**, 1–5 (2019).

29. Mathiowetz, V. *et al.* Grip and Pinch Strength: Normative Data for Adults. *Arch Phys Med Rehabil* **66**, 69–72 (1985).

30. Goodkin, D. E., Hertsguard, D. & Seminary, J. Upper extremity function in multiple sclerosis: Improving assessment sensitivity with box-and-block and nine-hole peg tests. *Arch. Phys. Med. Rehabil.* **69**, 850–854 (1988).

31. Feys, P. *et al.* The Nine-Hole Peg Test as a manual dexterity performance measure for multiple sclerosis. *Mult. Scler.* **23**, 711–720 (2017).

32. Murphy, S. M. *et al.* Reliability of the CMT neuropathy score (second version) in Charcot-

Marie-Tooth disease. *J. Peripher. Nerv. Syst.* **16**, 191–198 (2011).

33. Sadjadi, R. *et al.* Psychometrics evaluation of Charcot-Marie-Tooth Neuropathy Score (CMTNSv2) second version, using Rasch analysis. *J. Peripher. Nerv. Syst.* **19**, 192–196 (2014).
34. Bloch, F. Nuclear induction. *Phys. Rev.* **70**, 460–474 (1946).
35. Bloch, F., Hansen, W. W. & Packard, M. The Nuclear Induction Experiment. *Phys. Rev.* **70**, 474–485 (1946).
36. W-M Fan, T. & Lane, A. N. Applications of NMR spectroscopy to systems biochemistry Graphical abstract HHS Public Access. *Prog Nucl Magn Reson Spectrosc* 18–53 (2016). doi:10.1016/j.pnmrs.2016.01.005
37. Simpson, A. J., Simpson, M. J. & Soong, R. Nuclear magnetic resonance spectroscopy and its key role in environmental research. *Environ. Sci. Technol.* **46**, 11488–11496 (2012).
38. Mesilaakso, M. T. Application of NMR spectroscopy to environmental analysis: Detection of trace amounts of chemical warfare agents and related compounds in organic extract, water, and sand. *Environ. Sci. Technol.* **31**, 518–522 (1997).
39. Purcell, E. M., Torrey, H. C. & Pound, R. V. Resonance Absorption by Nuclear Magnetic Moments in a Solid. *Phys. Rev* **69**, (1946).
40. Damadian, R. *et al.* Nuclear Magnetic Resonance As a New Tool in Cancer Research: Human Tumors By Nmr. *Ann. N. Y. Acad. Sci.* **222**, 1048–1076 (1973).
41. Lauterbur, P. C. Image Formation by Induced Local Interactions: Examples Employing Nuclear Magnetic Resonance. *Nature* **242**, 190–191 (1973).
42. Mansfield, P. & Maudsley, A. A. Medical imaging by NMR. *Br. J. Radiol.* **50**, 188–194

(1977).

43. Stanisz, G. J. *et al.* T1, T2 relaxation and magnetization transfer in tissue at 3T. *Magn. Reson. Med.* **54**, 507–512 (2005).

44. O'Brien, J. S. & Sampson, E. L. Lipid composition of the normal human brain: gray matter, white matter, and myelin. *J. Lipid Res.* **6**, 537–544 (1965).

45. Roxanne Labranche, M. *et al.* Liver Iron Quantification with MR Imaging : A Primer for Radiologists 1. *RadioGraphics* **38**, 392–412 (2018).

46. Mansfield, P. & Maudsley, A. A. Planar Spin Imaging by NMR. *JMR* **27**, 101–119 (1977).

47. Paschal, C. B. & Morris, H. D. K-Space in the Clinic. *J. Magn. Reson. Imaging* **19**, 145–159 (2004).

48. Le Bihan, D. Diffusion, Perfusion and Functional MRI. *Funct. MRI* 23–27 (1996). doi:10.1007/978-88-470-2194-5_5

49. Baliyan, V., Das, C. J., Sharma, R. & Gupta, A. K. Diffusion weighted imaging: Technique and applications. *World J. Radiol.* **8**, 785 (2016).

50. Stejskal, E. O. & Tanner, J. E. Spin diffusion measurements: Spin echoes in the presence of a time-dependent field gradient. *J. Chem. Phys.* **42**, 288–292 (1965).

51. Stejskal, E. O. Use of spin echoes in a pulsed magnetic-field gradient to study anisotropie, restricted diffusion and flow. *J. Chem. Phys.* **43**, 3597–3603 (1965).

52. Chilla, G. S., Tan, C. H., Xu, C. & Poh, C. L. Diffusion weighted magnetic resonance imaging and its recent trend-a survey. *Quant. Imaging Med. Surg.* **5**, 407–22 (2015).

53. Taylor, D. G. & Bushell, M. C. The spatial mapping of translational diffusion coefficients by the NMR imaging technique. *Phys. Med. Biol.* **30**, 345–349 (1985).

54. Merboldt, K. D., Hanicke, W. & Frahm, J. Self-diffusion NMR imaging using stimulated echoes. *J. Magn. Reson.* **64**, 479–486 (1985).

55. Mori, S. & Zhang, J. Principles of Diffusion Tensor Imaging and Its Applications to Basic Neuroscience Research. *Neuron* **51**, 527–539 (2006).

56. Basser, P. J., Mattiello, J. & LeBihan, D. MR diffusion tensor spectroscopy and imaging. *Biophys. J.* **66**, 259–267 (1994).

57. Mori, S. & Zijl, P. Van. Diffusion Weighting by the Trace of the Diffusion Tensor within a Single Scan. *MRM* 41–52 (1995).

58. Budde, M. D., Xie, M., Cross, A. H. & Song, S. K. Axial diffusivity is the primary correlate of axonal injury in the experimental autoimmune encephalomyelitis spinal cord: A quantitative pixelwise analysis. *J. Neurosci.* **29**, 2805–2813 (2009).

59. Tu, T. *et al.* Radiological-pathological correlation of diffusion tensor and magnetization transfer imaging in closed head traumatic brain injury model. *Ann Neurol.* **79**, 907–920 (2016).

60. Chiang, C. *et al.* NeuroImage Quantifying white matter tract diffusion parameters in the presence of increased extra-fiber cellularity and vasogenic edema. *Neuroimage* **101**, 310–319 (2014).

61. Song, S.-K. *et al.* Dysmyelination Revealed through MRI as Increased Radial (but Unchanged Axial) Diffusion of Water. *Neuroimage* **17**, 1429–1436 (2002).

62. Van Everdingen, K. J., Van Der Grond, J., Kappelle, L. J., Ramos, L. M. P. & Mali, W. P. T. M. Diffusion-weighted magnetic resonance imaging in acute stroke. *Stroke* **29**, 1783–1790 (1998).

63. Soares, J. M., Marques, P., Alves, V. & Sousa, N. A hitchhiker's guide to diffusion tensor imaging. *Front. Neurosci.* **7**, 1–14 (2013).

64. Westin, C. F. *et al.* Q-space trajectory imaging for multidimensional diffusion MRI of the human brain. *Neuroimage* **135**, 345–362 (2016).

65. Nilsson, M. *et al.* Tensor-valued diffusion MRI in under 3 minutes: an initial survey of microscopic anisotropy and tissue heterogeneity in intracranial tumors. *Magn. Reson. Med.* **83**, 608–620 (2020).

66. Szczepankiewicz, F., Sjölund, J., Ståhlberg, F., Lätt, J. & Nilsson, M. Tensor-valued diffusion encoding for diffusional variance decomposition (DIVIDE): Technical feasibility in clinical MRI systems. *PLoS One* **14**, 1–20 (2019).

67. Henkelman, R. M., Stanisz, G. J. & Graham, S. J. Magnetization transfer in MRI: A review. *NMR Biomed.* **14**, 57–64 (2001).

68. Wolff, S. D. & Balaban, R. S. Magnetization transfer contrast (MTC) and tissue water proton relaxation in vivo. *Magn. Reson. Med.* **10**, 135–144 (1989).

69. Kucharcyk, W. & Macdonald, M, Stanisz, G, H. R. M. Relaxivity at MR Imaging : of Cerebrosides and pH. *Radiology* 521–529 (1994).

70. Sled, J. G. & Pike, G. B. Quantitative Interpretation of Magnetization Transfer in Spoiled Gradient Echo MRI Sequences. *J. Magn. Reson.* **145**, 24–36 (2000).

71. Li, K. *et al.* Multi-parametric MRI characterization of healthy human thigh muscles at 3.0 T - relaxation, magnetization transfer, fat/water, and diffusion tensor imaging. *NMR Biomed.* **27**, 1070–1084 (2014).

72. Smith, S. A. *et al.* Quantitative magnetization transfer characteristics of the human

cervical spinal cord in vivo: Application to adrenomyeloneuropathy. *Magn. Reson. Med.* **61**, 22–27 (2009).

73. Nagy, Z. & Weiskopf, N. Efficient Fat Suppression by Slice-Selection Gradient Reversal in Twice-Refocused Diffusion Encoding. **1260**, 1256–1260 (2008).
74. Brandão, S., Nogueira, L., Matos, E. et al. Fat suppression techniques (STIR vs. SPAIR) on diffusion-weighted imaging of breast lesions at 3.0 T: preliminary experience. *Radiol med* **120**, 705–713 (2015).
75. Dixon, Thomas, W. Simple Proton Spectroscopic Imaging. *Radiology* **153**, 189–194 (1984).
76. Morrow, J. M. *et al.* MRI biomarker assessment of neuromuscular disease progression : a prospective observational cohort study. *Lancet Neurol.* **15**, 65–77 (2016).
77. Lichtenstein, T. *et al.* MRI biomarkers of proximal nerve injury in CIDP. *Ann. Clin. Transl. Neurol.* **5**, 19–28 (2018).
78. Jende, J. M. E. *et al.* Diabetic neuropathy differs between type 1 and type 2 diabetes: Insights from magnetic resonance neurography. *Ann. Neurol.* **83**, 588–598 (2018).
79. Hiba, B. *et al.* Quantitative assessment of skeletal muscle degeneration in patients with myotonic dystrophy type 1 using MRI. *J. Magn. Reson. Imaging* **35**, 678–685 (2012).
80. Gloor, M. *et al.* Quantification of fat infiltration in oculopharyngeal muscular dystrophy: Comparison of three MR imaging methods. *J. Magn. Reson. Imaging* **33**, 203–210 (2011).
81. Beaulieu, C., Does, M.D., Snyder, R.E. and Allen, P. S. Changes in water diffusion due to Wallerian degeneration in peripheral nerve. *Magn. Reson. Med.* **36**, 627–631 (1996).
82. Stanisz, G. J., Midha, R., Munro, C. a & Henkelman, R. M. MR properties of rat sciatic nerve following trauma. *Magn Reson Med* **45**, 415–20 (2001).

83. Takagi, T., Nakamura, M., Yamada, M., Hikishima, K. & Momoshima, S. Visualization of peripheral nerve degeneration and regeneration: Monitoring with diffusion tensor tractography. *Neuroimage* **44**, 884–892 (2009).

84. Lehmann, H. C., Zhang, J., Mori, S. & Sheikh, K. A. Diffusion tensor imaging to assess axonal regeneration in peripheral nerves. *Exp. Neurol.* **223**, 238–244 (2010).

85. Manzanera Esteve, I. V. *et al.* Probabilistic Assessment of Nerve Regeneration with Diffusion MRI in Rat Models of Peripheral Nerve Trauma. *Sci. Rep.* **9**, 1–11 (2019).

86. Howe, F. A., Filler, A. G., Bell, B. A. & Griffiths, J. R. Magnetic resonance neurography. *Magn. Reson. Med.* **28**, 328–338 (1992).

87. Filler, A. G. *et al.* Application of magnetic resonance neurography in the evaluation of patients with peripheral nerve pathology. *J. Neurosurg.* **85**, 299–309 (1996).

88. Hiltunen, J. *et al.* Diffusion tensor imaging and tractography of distal peripheral nerves at 3 T. *Clin. Neurophysiol.* **116**, 2315–2323 (2005).

89. Kabakci, N. *et al.* Diffusion Tensor Imaging and Tractography of Median Nerve: Normative Diffusion Values. *Am. J. Neuroradiol.* **189**, 923–927 (2007).

90. Andreisek, G., White, L. M., Kassner, A., Tomlinson, G. & Sussman, M. S. Diffusion tensor imaging and fiber tractography of the median nerve at 1.5T: Optimization of b value. *Skeletal Radiol.* **38**, 51–59 (2009).

91. Zhou, Y., Kumaravel, M., Patel, V. S., Sheikh, K. A. & Narayana, P. A. Diffusion Tensor Imaging of Forearm Nerves in Humans. *J. Magn. Reson. Imaging* **36**, 920–927 (2012).

92. Zhou, Y. *et al.* High resolution diffusion tensor imaging of human nerves in forearm. *J. Magn. Reson. Imaging* **39**, 1374–1383 (2014).

93. Guggenberger, R. *et al.* Diffusion tensor imaging of the median nerve : intra- , inter-reader agreement , and agreement between two software packages. *Skeletal Radiol.* **41**, 971–980 (2012).

94. Guggenberger, R. *et al.* MR neurography of the median nerve at 3 . 0 T : Optimization of diffusion tensor imaging and fiber tractography. *Eur. J. Radiol.* **81**, e775–e782 (2012).

95. Guggenberger, R. *et al.* Diffusion tensor imaging of the median nerve at 3.0T using different MR scanners: Agreement of FA and ADC measurements. *Eur. J. Radiol.* **82**, e590–e596 (2013).

96. Heckel, A. *et al.* Peripheral Nerve Diffusion Tensor Imaging: Assessment of Axon and Myelin Sheath Integrity. *PLoS One* **10**, e0130833 (2015).

97. Does, M. D. & Snyder, R. E. T2 Relaxation of peripheral nerve measured in vivo. *Magn. Reson. Imaging* **13**, 575–580 (1995).

98. Does, M. D., Beaulieu, C., Allen, P. S. & Snyder, R. E. Multi-component T1 relaxation and magnetisation transfer in peripheral nerve. *Magn. Reson. Imaging* **16**, 1033–1041 (1998).

99. Odrobina, E. E., Lam, T. Y. J., Pun, T., Midha, R. & Stanisz, G. J. MR properties of excised neural tissue following experimentally induced demyelination. *NMR Biomed.* **18**, 277–284 (2005).

100. Manzanera, I. *et al.* Quantitative MRI of Nerve Pathology in Mouse Models of CMT1A and HNPP (P1.453). *Neurology* **90**, P1.453 (2018).

101. Dortch, R. D., Dethrage, L. M., Gore, J. C., Smith, S. A. & Li, J. Proximal nerve magnetization transfer MRI relates to disability in Charcot-Marie-Tooth diseases. *Neurology* **83**, 1545–1553 (2014).

102. Laule, C. *et al.* Magnetic resonance imaging of myelin. *Neurotherapeutics* **4**, 460–484 (2007).

103. Kim, H. S., Yoon, Y. C., Choi, B., Jin, W. & Cha, J. G. Muscle fat quanti fi cation using magnetic resonance imaging : case – control study of Charcot – Marie – Tooth disease patients and volunteers. 574–585 (2019). doi:10.1002/jcsm.12415

104. Schneider, C. *et al.* MRI detects peripheral nerve and adjacent muscle pathology in non-systemic vasculitic neuropathy (NSVN). *J. Neurol.* **266**, 975–981 (2019).

105. Smith, A. K. *et al.* Incorporating dixon multi-echo fat water separation for novel quantitative magnetization transfer of the human optic nerve in vivo. *Magn. Reson. Med.* **77**, 707–716 (2017).

106. Noguerol, T. M., Alcalá, A. L., Cabrera, M. G., Cabrero, J. B. & Vilanova, J. C. Advanced MR Imaging Techniques for Differentiation of Neuropathic Arthropathy and Osteomyelitis in the Diabetic Foot 1. *RadioGraphics* **37**, 1161–1180 (2017).

107. Li, J., Parker, B., Martyn, C., Natarajan, C. & Guo, J. The PMP22 gene and its related diseases. *Mol. Neurobiol.* **47**, 673–698 (2013).

108. Sander, S., Ouvrier, R. A., McLeod, J. G., Nicholson, G. A. & Pollard, J. D. Clinical syndromes associated with tomacula or myelin swellings in sural nerve biopsies. *J. Neurol. Neurosurg. Psychiatry* **68**, 483–488 (2000).

109. Shy, M. E. *et al.* Reliability and validity of the CMT neuropathy score as a measure of disability. *Neurology* **64**, 1209–1214 (2005).

110. Krajewski, K. M. Neurological dysfunction and axonal degeneration in Charcot-Marie-Tooth disease type 1A. *Brain* **123**, 1516–1527 (2000).

111. Bird, T. D. Hereditary Neuropathy with Liability to Pressure Palsies Clinical Characteristics Clinical Description. 1–12 (2019).

112. Vinci, P. Perplexity about the use of the Charcot-Marie-Tooth neuropathy score in rehabilitation. *Eur. J. Phys. Rehabil. Med.* **44**, 473–474 (2008).

113. Schmierer, K., Scaravilli, F., Altmann, D. R., Barker, G. J. & Miller, D. H. Magnetization transfer ratio and myelin in postmortem multiple sclerosis brain. *Ann. Neurol.* **56**, 407–415 (2004).

114. Henkelman, R. M. *et al.* Quantitative interpretation of magnetization transfer. *Magn Reson Med* **29**, 759–766 (1993).

115. Li, K. *et al.* A rapid approach for quantitative magnetization transfer imaging in thigh muscles using the pulsed saturation method. *Magn. Reson. Imaging* **33**, 709–717 (2015).

116. Skinner, T. E. & Glover, G. H. An extended two-point Dixon algorithm for calculating separate water, fat, and b0 images. *Magn. Reson. Med.* **37**, 628–630 (1997).

117. Li, J., Krajewski, K., Shy, M. E. & Lewis, R. A. Hereditary neuropathy with liability to pressure palsy: the electrophysiology fits the name. *Neurology* **58**, 1769–73 (2002).

118. Hu, B., Arpag, S., Zuchner, S. & Li, J. A novel missense mutation of CMT2P alters transcription machinery. *Ann. Neurol.* **80**, 834–845 (2016).

119. MATLAB® Statistics and Machine Learning Toolbox Release 2017a, The MathWorks, Inc., Natick, Massachusetts, United States of America.

120. MATLAB® Curve Fitting Toolbox Release 2017a, The MathWorks, Inc., Natick, Massachusetts, United States of America.

121. Smith, D. S., Berglund, J., Kullberg, J. Optimization of Fat-Water Separation Algorithm

Selection and Options Using Image-based Metrics with Validation by. *21st Annu. Sci. Meet. ISMRM, Abstr. #2413* (2013).

122. Hu, B. *et al.* Tuning PAK Activity to Rescue Abnormal Myelin Permeability in HNPP. *PLoS Genet.* **12**, 1–24 (2016).

123. Li, J. *et al.* Stoichiometric alteration of PMP22 protein determines the phenotype of hereditary neuropathy with liability to pressure palsies. *Arch. Neurol.* **64**, 974–978 (2007).

124. Pareyson, D., Scaioli, V. & Laurá, M. Clinical and electrophysiological aspects of Charcot-Marie-Tooth disease. *Neuromolecular Med.* **8**, 197–206 (2006).

125. Padua, L. *et al.* Natural history of charcot-marie-tooth 2: 2-year follow-up of muscle strength, walking ability and quality of life. *Neurol. Sci.* **31**, 175–178 (2010).

126. Lewis, R. A. *et al.* High-dosage ascorbic acid treatment in charcot-marie-tooth disease type 1A results of a randomized, double-masked, controlled trial. *JAMA Neurol.* **70**, 981–987 (2013).

127. Ortega, X. *et al.* Variability of muscle fat fraction quantification in MRI using the Dixon technique. *IMÁGENES PEDIÁTRICAS* **22**, 149–155 (2016).

128. Hamrick, M. W., McGee-Lawrence, M. E. & Frechette, D. M. Fatty Infiltration of Skeletal Muscle: Mechanisms and Comparisons with Bone Marrow Adiposity. *Front. Endocrinol. (Lausanne).* **7**, 1–7 (2016).

129. Davison, M. J., Maly, M. R., Adachi, J. D., Noseworthy, M. D. & Beattie, K. A. Relationships between fatty infiltration in the thigh and calf in women with knee osteoarthritis. *Aging Clin. Exp. Res.* **29**, 291–299 (2017).

130. Morrow, J. M. *et al.* Reproducibility, and age, body-weight and gender dependency of candidate skeletal muscle MRI outcome measures in healthy volunteers. *Eur. Radiol.* **24**, 1610–1620 (2014).

131. Hong, Y. H. *et al.* Clinical and electrophysiologic features of HNPP patients with 17p11.2 deletion. *Acta Neurol. Scand.* **108**, 352–358 (2003).

132. Chung, K. W. *et al.* Different clinical and magnetic resonance imaging features between Charcot-Marie-Tooth disease type 1A and 2A. *Neuromuscul. Disord.* **18**, 610–618 (2008).

133. Marcus, R. L., Addison, O., Kidde, J. P., Dibble, L. E. & Lastayo, P. C. Skeletal muscle fat infiltration: Impact of age, inactivity, and exercise. *J. Nutr. Heal. Aging* **14**, 362–366 (2010).

134. Spees, W. M. *et al.* MRI-based assessment of function and dysfunction in myelinated axons. *Proc. Natl. Acad. Sci.* **115**, E10225–E10234 (2018).

135. Ropele, S. *et al.* A comparison of magnetization transfer ratio, magnetization transfer rate, and the native relaxation time of water protons related to relapsing-remitting multiple sclerosis. *Am. J. Neuroradiol.* **21**, 1885–1891 (2000).

136. Kollmer, J., Kästel, T., Jende, J. M. E., Bendszus, M. & Heiland, S. Magnetization Transfer Ratio in Peripheral Nerve Tissue: Does It Depend on Age or Location? *Invest. Radiol.* **53**, 397–402 (2018).

137. Lichtenstein, T. *et al.* MRI biomarkers of proximal nerve injury in CIDP. *Ann. Clin. Transl. Neurol.* **5**, 1–24 (2016).

138. Heath, F., Hurley, S. A., Johansen-Berg, H. & Sampaio-Baptista, C. Advances in noninvasive myelin imaging. *Dev. Neurobiol.* **78**, 136–151 (2018).

139. Jende, J. M. E. *et al.* Peripheral nerve involvement in multiple sclerosis: Demonstration by magnetic resonance neurography. *Ann. Neurol.* **82**, 676–685 (2017).

140. Campbell, W. W. Evaluation and management of peripheral nerve injury. *Clinical Neurophysiology* (1978). doi:10.1016/j.clinph.2008.03.018

141. Noble, J., Munro, C. A., Prasad, V. S. S. V. & Midha, R. Analysis of upper and lower extremity peripheral nerve injuries in a population of patients with multiple injuries. *J. Trauma - Inj. Infect. Crit. Care* **45**, 116–122 (1998).

142. Chhabra, A., Ahlawat, S., Belzberg, A. & Andreseik, G. Peripheral nerve injury grading simplified on MR neurography: As referenced to Seddon and Sunderland classifications. *Indian J. Radiol. Imaging* **24**, 217 (2014).

143. Cross, J. D., Ficke, J. R., Hsu, J. R., Masini, B. D. & Wenke, J. C. Battlefield orthopaedic injuries cause the majority of long-term disabilities. *J. Am. Acad. Orthop. Surg.* **19**, 1–7 (2011).

144. Stansbury, L. G., Branstetter, J. G. & Lalliss, S. J. Amputation in military trauma surgery. *J. Trauma - Inj. Infect. Crit. Care* **63**, 940–944 (2007).

145. Ciaramitaro, P. *et al.* Traumatic peripheral nerve injuries: Epidemiological findings, neuropathic pain and quality of life in 158 patients. *J. Peripher. Nerv. Syst.* **15**, 120–127 (2010).

146. Kouyoumdjian, J. A. Peripheral nerve injuries: A retrospective survey of 456 cases. *Muscle and Nerve* **34**, 785–788 (2006).

147. Brown, J. M., Tung, T. H. H. & Mackinnon, S. E. Median to Radial Nerve Transfer to Restore Wrist and Finger Extension. *Oper. Neurosurg.* **66**, ons75–ons83 (2010).

148. Mafi, P., Hindocha, S., Dhital, M. & Saleh, M. Advances of Peripheral Nerve Repair Techniques to Improve Hand Function: A Systematic Review of Literature. *Open Orthop. J.* **6**, 60–68 (2012).

149. Ruijs, A. C. J., Jaquet, J. B., Kalmijn, S., Giele, H. & Hovius, S. E. R. Median and ulnar nerve injuries: A meta-analysis of predictors of motor and sensory recovery after modern microsurgical nerve repair. *Plastic and Reconstructive Surgery* **116**, 484–494 (2005).

150. Grinsell, D. & Keating, C. P. Peripheral Nerve Reconstruction after Injury: A Review of Clinical and Experimental Therapies. *Biomed Res. Int.* **2014**, (2014).

151. Chaudhry, V. & Cornblath, D. R. Wallerian degeneration in human nerves: Serial electrophysiological studies. *Muscle Nerve* **15**, 687–693 (1992).

152. Oh, S. J. Electromyographic studies in peripheral nerve injuries. *South. Med. J.* **69**, 177–182 (1976).

153. Robinson, L. R. Traumatic injury to peripheral nerves. *Muscle and Nerve* **23**, 863–873 (2000).

154. Cartwright, M. S., Chloros, G. D., Walker, F. O., Wiesler, E. R. & Campbell, W. W. Diagnostic ultrasound for nerve transection. *Muscle and Nerve* **35**, 796–799 (2007).

155. Suk, J. I., Walker, F. O. & Cartwright, M. S. Ultrasound of peripheral nerves. *Curr Neurol Neurosci Rep.* **13**, 328 (2013).

156. Behr, B. *et al.* Magnetic resonance imaging monitoring of peripheral nerve regeneration following neurotmesis at 4.7 tesla. *Plast. Reconstr. Surg.* **123**, 1778–1788 (2009).

157. Agosta, F. *et al.* In vivo assessment of cervical cord damage in MS patients: A longitudinal diffusion tensor MRI study. *Brain* **130**, 2211–2219 (2007).

158. Bennett, R. E., Mac Donald, C. L. & Brody, D. L. Diffusion tensor imaging detects axonal injury in a mouse model of repetitive closed-skull traumatic brain injury. *Neurosci. Lett.* **513**, 160–165 (2012).

159. Filippi, M., Cercignani, M., Inglese, M. & Al., E. Diffusion tensor magnetic resonance imaging. *Neurology* **56**, 304–311 (2001).

160. Jeon, T., Fung, M. M., Koch, K. M., Tan, E. T. & Sneag, D. B. Peripheral nerve diffusion tensor imaging: Overview, pitfalls, and future directions. *J. Magn. Reson. Imaging* **47**, 1171–1189 (2018).

161. Meek, M. F., Stenekes, M. W., Hoogduin, H. M. & Nicolai, J. A. In vivo three-dimensional reconstruction of human median nerves by diffusion tensor imaging. *Exp. Neurol.* **198**, 479–482 (2006).

162. Kabakci, N. T., Kovanlikaya, A. & Kovanlikaya, I. Tractography of the Median Nerve. *Semin. Musculoskelet. Radiol.* **198**, 479–482 (2009).

163. Naraghi, A. M., Awdeh, F. H., Chhabra, A., Wadhwa, V. & Andreisek, G. Diffusion Tensor Imaging of Peripheral Nerves. (2015).

164. Mori, S. & Zijl, P. C. M. Van. Fiber tracking: principles and strategies - a technical review. *NMR Biomed.* **15**, 468–480 (2002).

165. Boyer, R. B. *et al.* 4.7-T diffusion tensor imaging of acute traumatic peripheral nerve injury. *Neurosurg. Focus* **39**, E9 (2015).

166. Farinas, A. F. *et al.* Diffusion tensor tractography to visualize axonal outgrowth and regeneration in a 4-cm reverse autograft sciatic nerve rabbit injury model. *Neurol. Res.* **41**, 257–264 (2019).

167. Ghergherehchi, C. L. *et al.* Polyethylene glycol (PEG) and other bioactive solutions with neurorrhaphy for rapid and dramatic repair of peripheral nerve lesions by PEG-fusion. *J. Neurosci. Methods* **314**, 1–12 (2019).

168. Ginimuge, P. R. & Jyothi, S. D. Methylene Blue : Revisited. **26**, 517–520 (2010).

169. Bamba, R. *et al.* A novel therapy to promote axonal fusion in human digital nerves. *J. Trauma Acute Care Surg.* **81**, S177–S183 (2016).

170. Paskal, A. M., Paskal, W., Pietruski, P. & Wlodarski, P. K. Polyethylene glycol: The future of posttraumatic nerve repair? systemic review. *Int. J. Mol. Sci.* **20**, 1–10 (2019).

171. MATLAB. (2017). version 2017a. Natick, Massachusetts: The MathWorks Inc.

172. Bazina, P.-L. *et al.* Volumetric Neuroimage Analysis Extensions for the MIPAV Software Package. *J. Neurosci. Methods* **165**, 111–121 (2007).

173. Song, S. K. *et al.* Diffusion tensor imaging detects and differentiates axon and myelin degeneration in mouse optic nerve after retinal ischemia. *Neuroimage* **20**, 1714–1722 (2003).

174. Morisaki, S. *et al.* In vivo assessment of peripheral nerve regeneration by diffusion tensor imaging. *J. Magn. Reson. Imaging* **33**, 535–542 (2011).

175. Svennigsen, Å. F. & Dahlin, L. B. Repair of the peripheral nerve-remyelination that works. *Brain Sci.* **3**, 1182–1197 (2013).

176. Winklewski, P. J. *et al.* Understanding the physiopathology behind axial and radial diffusivity changes-what do we Know? *Front. Neurol.* **9**, (2018).

177. Alexander, A. L., Lee, J. E., Lazar, M. & Field, A. S. Diffusion Tensor Imaging of the Brain Andrew. *Neurotherapeutics* **4**, 316–329 (2007).

178. Rotman, M. B., Enkvetchakul, B. V., Megerian, J. T. & Gozani, S. N. Time course and predictors of median nerve conduction after carpal tunnel release. *J. Hand Surg. Am.* **29**, 367–372 (2004).

179. Williams, S. E. *et al.* Quantitative effects of inclusion of fat on muscle diffusion tensor MRI measurements. *J. Magn. Reson. Imaging* **38**, 1292–1297 (2013).

180. Topgaard, D. Multidimensional diffusion MRI. *J. Magn. Reson.* **275**, 98–113 (2017).

181. Szczepankiewicz, F., Westen, D. Van, Englund, E. & Westin, C. The link between diffusion MRI and tumor heterogeneity: Mapping cell eccentricity and density by diffusional variance decomposition (DIVIDE). 522–532 (2017). doi:10.1016/j.neuroimage.2016.07.038.The

182. Westin, C. *et al.* NeuroImage Q-space trajectory imaging for multidimensional diffusion MRI of the human brain. *Neuroimage* **135**, 345–362 (2016).

183. Szczepankiewicz, F. *et al.* Quantification of microscopic diffusion anisotropy disentangles effects of orientation dispersion frommicrostructure: Applications in healthy volunteers and in brain tumors. *Neuroimage* **104**, 241–252 (2015).

184. Shemesh, N. *et al.* Conventions and Nomenclature for Double Diffusion Encoding NMR and MRI. **87**, 82–87 (2016).

185. Cory, D. G. & Garroway, A. N. Measurement of Translational Displacement Probabilities by NMR: An Indicator of Compartmentation. *Magn. Reson. Med.* **14**, 435–444 (1990).

186. Lasič, S., Jespersen, S. N., Lundell, H., SÃ¸nderby, C. K. & Dyrby, T. B. Microanisotropy imaging: quantification of microscopic diffusion anisotropy and orientation of order parameter by diffusion MRI with magic-angle spinning of the q-vector. *Front. Phys.* **2**, 1–

14 (2014).

187. Stassart, R. M., Möbius, W., Nave, K. A. & Edgar, J. M. The Axon-Myelin unit in development and degenerative disease. *Front. Neurosci.* **12**, (2018).

188. Sjölund, J. *et al.* Constrained optimization of gradient waveforms for generalized diffusion encoding. **261**, 157–168 (2015).

189. Nilsson, M. Github repository. (2018). doi:https://github.com/markus-nilsson/md-dmri

190. Wada, K., Hashimoto, T., Miyagi, R., Sakai, T. & Sairyo, K. Diffusion tensor imaging and tractography of the sciatic nerve: assessment of fractional anisotropy and apparent diffusion coefficient values relative to the piriformis muscle, a preliminary study. *Skeletal Radiol.* **46**, 309–314 (2017).

191. Stanisz, G. J., Webb, S., Munro, C. A., Pun, T. & Midha, R. MR Properties of Excised Neural Tissue Following Experimentally Induced Inflammation. *Magn. Reson. Med.* **51**, 473–479 (2004).

192. Zhang, H., Schneider, T., Wheeler-kingshott, C. A. & Alexander, D. C. NeuroImage NODDI : Practical in vivo neurite orientation dispersion and density imaging of the human brain. *Neuroimage* **61**, 1000–1016 (2012).

193. Kaden, E., Kruggel, F. & Alexander, D. C. Quantitative mapping of the per-axon diffusion coefficients in brain white matter. *Magn. Reson. Med.* **75**, 1752–1763 (2016).

194. Steven, A. J., Zhuo, J. & Melhem, E. R. Diffusion kurtosis imaging: An emerging technique for evaluating the microstructural environment of the brain. *Am. J. Roentgenol.* **202**, 26–33 (2014).

195. Driban, J. B., Swanik, C. B. & Barbe, M. F. Anatomical evaluation of the tibial nerve within

the popliteal fossa. *Clin. Anat.* **20**, 694–698 (2007).

196. Bathala, L., Kumar, P., Kumar, K., Shaik, A. B. & Visser, L. H. Normal values of median nerve cross-sectional area obtained by ultrasound along its course in the arm with electrophysiological correlations, in 100 Asian subjects. *Muscle and Nerve* **49**, 284–286 (2014).